



A Staggered Semi-implicit Discontinuous Galerkin Scheme with a Posteriori Subcell Finite Volume Limiter for the Euler Equations of Gasdynamics

Matteo Ioriatti¹ · Michael Dumbser¹ · Raphaël Loubère²

Received: 18 April 2019 / Revised: 15 March 2020 / Accepted: 26 March 2020 / Published online: 19 April 2020
© Springer Science+Business Media, LLC, part of Springer Nature 2020

Abstract

In this paper we propose a novel semi-implicit Discontinuous Galerkin (DG) finite element scheme on staggered meshes with a posteriori subcell finite volume limiting for the one and two dimensional Euler equations of compressible gasdynamics. We therefore extend the strategy adopted by Dumbser and Casulli (Appl Math Comput 272:479–497, 2016), where the Euler equations have been solved using a semi-implicit finite volume scheme based on the flux-vector splitting method recently proposed by Toro and Vázquez-Cendón (Comput Fluids 70:1–12, 2012). In our scheme, the nonlinear convective terms are discretized explicitly, while the pressure terms are discretized implicitly. As a consequence, the time step is restricted only by a mild CFL condition based on the fluid velocity, which makes this method particularly suitable for simulations in the low Mach number regime. However, the conservative formulation of the scheme, together with the novel subcell finite volume limiter allows also the numerical simulation of high Mach number flows with shock waves. Inserting the discrete momentum equation into the discrete total energy conservation law yields a mildly nonlinear system with the scalar pressure as the only unknown. Due to the use of staggered meshes, the resulting pressure system has the most compact stencil possible and can be efficiently solved with modern iterative methods. In order to deal with shock waves or steep gradients, the new semi-implicit DG scheme proposed in this paper includes an a posteriori subcell finite volume limiting technique. This strategy was first proposed by Dumbser et al. (J Comput Phys 278:47–75, 2014) for explicit DG schemes on collocated grids and is based on the a posteriori MOOD algorithm of Clain, Loubère and Diot. Recently, this methodology was also extended to semi-implicit DG schemes on staggered meshes for the shallow water equations in Ioriatti and Dumbser (Appl Numer Math 135:443–480, 2019). Within the MOOD approach, an *unlimited* DG scheme first produces a so-called *candidate solution* for the next time level t^{n+1} . Later on, the control volumes with a non-admissible candidate solution are identified by using physical and numerical detection criteria, such as the positivity of the solution, the absence of floating point errors and the satisfaction of a relaxed discrete maximum principle (DMP). Then, in the detected troubled cells a more robust first order semi-implicit finite volume (FV) method is applied on a sub-grid composed of $2P + 1$ subcells, where P denotes the polynomial degree used in the DG scheme. For that

✉ Matteo Ioriatti
matteo.ioriatti@unitn.it

Extended author information available on the last page of the article

purpose, the nonlinear convective terms are recomputed in the troubled cells using an explicit finite volume scheme on the subcell level. Also the linear system for the pressure needs to be assembled and solved again, but where now a low order semi-implicit finite volume scheme is used on the sub-cell level in all troubled DG elements, instead of the original high order DG method. Finally, the higher order DG polynomials are reconstructed from the piecewise constant subcell finite volume averages and the scheme proceeds to the next time step. In this paper we present, discuss and test this novel family of methods and simulate a set of classical numerical benchmark problems of compressible gasdynamics. Great attention is dedicated to 1D and 2D Riemann problems and we also show that for these test cases the scheme responds appropriately in the presence of shock waves and does not produce non-physical spurious numerical oscillations.

Keywords High order semi-implicit discontinuous Galerkin scheme · A posteriori sub-cell finite volume limiter · Staggered grid · MOOD paradigm · Sub-cell finite volume limiting · Euler equations of compressible gasdynamics · Low Mach number flows

1 Introduction

Computational fluid dynamics is a branch of applied mathematics that demands the development of advanced, accurate and efficient algorithms for the numerical solution of partial differential equations (PDEs) in multiple space dimensions. These mathematical tools have become widespread in many scientific applications in the contexts of computational physics, aerospace engineering and bio-medical sciences. Nowadays, there exist several dedicated solvers capable of simulating a large range of physical flow configurations. However, an ultimate numerical method for all the possible flow conditions still does not exist. In this paper we develop a novel algorithm that is at the same time suitable for low Mach number (or nearly incompressible) flows, where classical explicit methods are typically not efficient due to the CFL timestep restriction based on the speed of sound, as well as for high Mach number flows with shock waves and contact discontinuities. It is therefore our declared goal to develop a new all Mach number flow solver that is able to cope with a large range of different possible flow regimes of the compressible Euler and Navier–Stokes equations.

The Discontinuous Galerkin (DG) method is a finite element method where the numerical solution is approximated by high order piecewise polynomials. It was first developed by Reed and Hill for the discretization of the governing equations of neutron transport phenomena [70]. Later on, this method rapidly gained popularity after the works of Cockburn and Shu. In particular, in [24,26–28,28] the DG method was extended to general systems of nonlinear hyperbolic PDE. While the aforementioned DG schemes were based on TVD Runge–Kutta time integrators, space-time DG methods were first developed by Van der Vegt et al. in [86,87]. DG schemes were applied for the first time to the Navier–Stokes equations by Bassi and Rebay [3], Baumann and Oden [4,5], Hartmann and Houston [51,52], Gassner et al. [48] and Klaij et al. [59]. Moreover, a new family of fully-discrete explicit one-step DG schemes was proposed in [40] and [69]. A central DG method that employs overlapping meshes was introduced by Liu et al. in [63,64]. Most of the DG methods mentioned so far, apart from the space-time DG approach, which is by construction fully implicit, are characterized by an explicit time integration; this feature makes them inefficient for situations characterized by very low Mach numbers. An implicit discretization allows to avoid this problem. In this framework, we mention the implicit DG schemes on *collocated grids* developed by Bassi et

al. [1,2] and the semi-implicit DG scheme of Dolejsi and Feistauer [31]. Other semi-implicit DG methods on collocated grids have been presented for the shallow water equations in [84,85]. For a new family of semi-implicit hybrid finite volume/finite element schemes, see [10,11].

A particularly efficient family of semi-implicit finite volume and finite difference algorithms on staggered meshes for computational fluid dynamics has been developed in a series of papers by Casulli et al. in [12–14,16,18–20]. Later, this family of algorithms was extended to incompressible and compressible fluid flow in elastic pipes, see e.g. [17,37,46,56,81], and in [33,36] these schemes were extended to the compressible Navier–Stokes equations and to viscous and resistive magnetohydrodynamics (MHD), respectively. The first high-order semi-implicit DG scheme on staggered meshes for the shallow water equations has been proposed in [35] and was later successfully extended to the compressible and incompressible Navier–Stokes equations on unstructured meshes [75–79], to adaptive Cartesian grids (AMR) [44,45], as well as to compressible fluid flow in elastic pipes [54] and linear elasticity [80]. The main advantage of the use of staggered meshes consists in the fact that the resulting linear system for the pressure is typically symmetric, positive definite and well conditioned, so that the discrete pressure can be efficiently computed using iterative methods. Furthermore, the use of a staggered mesh leads to a pressure system with the most compact possible stencil, involving only the cell and its direct neighbors, together with the smallest number of unknowns, namely only the scalar pressure. A drawback of high order DG schemes is the generation of spurious oscillations near discontinuities or strong gradients due to Gibbs’ phenomenon. This fact is justified by Godunov’s theorem [49], according to which *linear* monotone schemes can be at most first order accurate. In order to overcome this problem, a simple strategy consists in adding some artificial viscosity to the scheme [66]. However, determining the precise location and amount of the artificial viscosity to be added is not a trivial task, and is the subject of many publications in the CFD literature. Recently, a more sophisticated technique, called *a posteriori subcell finite volume limiting*, was presented in [39,42,55,90]. This new limiter is based on the ideas of the a posteriori MOOD approach that was introduced in [23,29,30,65] for finite volume schemes.

In the present work we propose a novel high order *semi-implicit* DG finite element method on staggered meshes with *a posteriori* subcell finite volume limiting for the Euler equations of compressible gasdynamics. The method represents the natural high order extension to staggered Cartesian grids of the schemes proposed in [36,79]. In addition, the limiting approach is carried out following the ideas introduced in [55] for the shallow water equations.

The rest of paper is structured as follows. In Sects. 2 and 3 we derive the new *a posteriori* subcell finite volume limiter for semi-implicit staggered DG methods for the Euler equations of gasdynamics in one and two space dimensions. In Sects. 4 and 5 the numerical method is validated for several classical benchmarks that involve smooth and discontinuous solutions. Finally, in Sect. 6 we give some conclusions and provide an outlook to future research.

2 Staggered Semi-implicit DG Schemes with a Posteriori Sub-cell Finite Volume Limiting for the Euler Equations in 1D

In this section we introduce our staggered semi-implicit DG schemes with *a posteriori* subcell finite volume limiting for the 1D Euler equations. For the sake of a comprehensive presentation, we first derive the unlimited semi-implicit 1D DG scheme in Sect. 2.2; then in Sect. 2.3 we introduce a semi-implicit FV method within a proper subcell formulation. Later

on, we recall the MOOD algorithm and we conclude in Sect. 2.5 with the general scheme that combines these two methods. In the following, several universal tensors will be used and we report them in the “Appendix A”.

2.1 Governing Equations of the 1D Model

The Euler equations of compressible gasdynamics in one space dimension are a well-known system of hyperbolic PDEs and read as follows

$$\begin{aligned}\frac{\partial \rho}{\partial t} + \frac{\partial(\rho u)}{\partial x} &= 0, \\ \frac{\partial(\rho u)}{\partial t} + \frac{\partial}{\partial x}(\rho u^2 + p) &= 0, \\ \frac{\partial(\rho E)}{\partial t} + \frac{\partial}{\partial x}(u(\rho E + p)) &= 0.\end{aligned}\quad (1)$$

The Eq. (1) state the principles of mass, momentum and total energy conservation. The spatial and the temporal coordinates are x and t and the computational domain is denoted by $\Omega_x = [x_L, x_R]$ in the following. Furthermore, $\rho(x, t)$ is the fluid density, $u(x, t)$ is the velocity, $p(x, t)$ is the pressure and $E(x, t)$ is the specific total energy. Additionally, we have $E = e + k$, where e is the specific internal energy and $k = \frac{1}{2}u^2$ is the specific kinetic energy. We introduce another quantity called specific enthalpy $h = e + p/\rho$ and consequently we rewrite the flux of the energy equation as the sum of two different contributions $u(\rho E + p) = u\rho k + h\rho u$, see [36, 67, 83]. In order to close the system, we use the equation of state (EOS) for an ideal gas, which reads

$$e = e(p, \rho) = \frac{p}{(\gamma - 1)\rho}. \quad (2)$$

Here, $\gamma = c_p/c_v$ is the ratio of specific heats, which typically lies in the range $1 < \gamma < 3$. In this paper we will consider this quantity as a constant and equal to $\gamma = 1.4$, which is the adiabatic index of a diatomic gas and thus a reasonable value for air at moderate pressures and temperatures.

The system in Eq. (1) can be written in more compact matrix-vector notation as

$$\frac{\partial \mathbf{Q}}{\partial t} + \frac{\partial \mathbf{F}(\mathbf{Q})}{\partial x} = 0, \quad (3)$$

where $\mathbf{Q} = [\rho, \rho u, \rho E]^T$ is the vector of conserved variables and $\mathbf{F} = [\rho u, \rho u^2 + p, u(\rho E + p)]^T$ is the physical flux vector. In addition, it is possible to introduce the vector of the primitive variables $\mathbf{V} = [\rho, u, p]^T$. In quasi-linear form the above system reads

$$\frac{\partial \mathbf{Q}}{\partial t} + \mathbf{A}(\mathbf{Q}) \frac{\partial \mathbf{Q}}{\partial x} = 0, \quad (4)$$

where $\mathbf{A}(\mathbf{Q}) = \partial \mathbf{F}(\mathbf{Q}) / \partial \mathbf{Q}$ is the Jacobian matrix of the system. For the Euler equations, $\mathbf{A}(\mathbf{Q})$ has three real eigenvalues: $\lambda_1 = u - a$, $\lambda_2 = u$ and $\lambda_3 = u + a$, where a is the sound speed. For an ideal gas the sound speed is equal to $a = \sqrt{\gamma p/\rho}$. Moreover, the matrix \mathbf{A} has a complete set of linearly independent eigenvectors, hence the system is hyperbolic. For a thorough discussion of the Euler equations of gasdynamics and numerical methods for their discretization, the reader is referred to the textbook of Toro [82]. Following the flux vector splitting proposed by Toro and Vázquez-Cendón in [83] and the ideas outlined in [33, 36, 67],

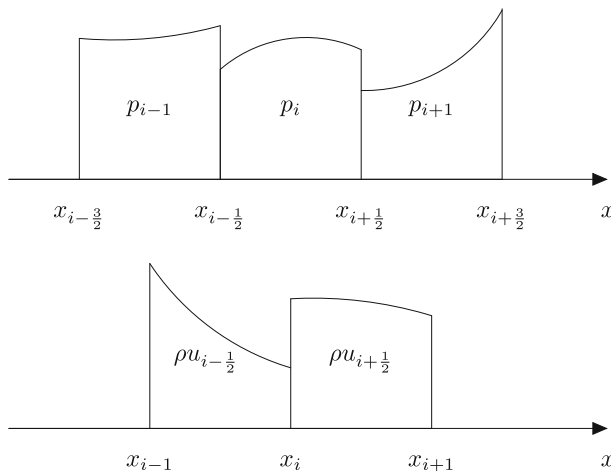


Fig. 1 Staggered grids for the one-dimensional DG scheme. Main grid used for the free surface (top) and dual mesh for the velocity (bottom)

the PDE system (3) can now be rewritten as

$$\frac{\partial \mathbf{Q}}{\partial t} + \frac{\partial \mathbf{F}^c(\mathbf{Q})}{\partial x} + \frac{\partial \mathbf{F}^p(\mathbf{Q})}{\partial x} = 0, \quad (5)$$

with the nonlinear convective flux $\mathbf{F}^c(\mathbf{Q}) = [\rho u, \rho u^2, \rho u k]^T$ that does not contain any pressure terms, and the pressure flux $\mathbf{F}^p(\mathbf{Q}) = [0, p, h\rho u]^T$. Following [36] and [33], in this paper we will discretize \mathbf{F}^c explicitly and \mathbf{F}^p implicitly. In [83] it was shown that the Jacobian of the convective flux $\mathbf{A}^c(\mathbf{Q}) = \partial \mathbf{F}^c(\mathbf{Q}) / \partial \mathbf{Q}$ has the eigenvalues $\lambda_1^c = 0$ and $\lambda_{2,3}^c = u$, i.e. the CFL condition on the explicit part of the scheme will depend only on the bulk flow velocity u and not on the sound speed a . For this reason, the method presented in this paper can also be used for the simulation of low Mach number flows.

2.2 Unlimited Staggered Semi-implicit DG Scheme for the 1D Euler Equations

We consider a computational domain $\Omega_x = [x_L, x_R]$ composed of two overlapping grids (see Fig. 1). The first one is called main grid, which contains N_x cells characterized by a constant length $\Delta x = \frac{L}{N_x} = \frac{x_R - x_L}{N_x}$, while the second grid is called dual mesh and it has $N_x + 1$ elements. On this last grid there are $N_x - 1$ equally spaced elements, while the length of the cells on the left and on the right boundary is only $\Delta x/2$. A generic element of the main grid is denoted by $T_i = [x_{i-\frac{1}{2}}, x_{i+\frac{1}{2}}]$, whereas a control volume on the staggered grid is indicated as $T_{i+\frac{1}{2}} = [x_i, x_{i+1}]$ and its edges are the barycenters of two consecutive cells of the main grid. In order to represent our numerical solution via piecewise polynomials of degree P , we use a set of basis functions $\varphi(\xi)$ defined on the reference element $[0, 1]$. In particular, we choose a *nodal basis* given by the Lagrange interpolation polynomials passing through the Gauss-Legendre quadrature points of the reference element $[0, 1]$. This basis is by construction orthogonal. For any physical control volume we generate the basis functions $\phi_l(x)$ on the main grid and the basis functions $\psi_l(x)$ on the dual grid from $\varphi_l(\xi)$ as

$$\begin{aligned} \phi_l(x) &= \varphi_l(\xi) \quad \text{with } x = x_{i-\frac{1}{2}} + \xi \Delta x, \quad \text{and} \quad \psi_l(x) = \varphi_l(\xi) \\ &\quad \text{with } x = x_i + \xi \Delta x, \quad 0 \leq \xi \leq 1. \end{aligned} \quad (6)$$

Then, a quantity located on the main grid, for example the pressure, is approximated within T_i as follows

$$p_i(x, t) = \sum_{l=1}^{P+1} \phi_l(x) \hat{p}_{i,l}(t) := \boldsymbol{\phi}(x) \cdot \hat{\mathbf{p}}_i(t), \quad (7)$$

while for variables that are defined on the staggered dual mesh, such as the fluid velocity, we have within $T_{i+\frac{1}{2}}$

$$u_{i+\frac{1}{2}}(x, t) = \sum_{l=1}^{P+1} \psi_l(x) \hat{u}_{i+\frac{1}{2},l}(t) := \boldsymbol{\psi}(x) \cdot \hat{\mathbf{u}}_{i+\frac{1}{2}}(t) \quad (8)$$

where $\hat{\mathbf{p}}$ and $\hat{\mathbf{u}}$ are the degrees of freedom for the pressure and for the velocity, respectively. Following the ideas of semi-implicit methods, see e.g. [36, 67, 83], the Euler equations can be split into a convective sub-system, which contains the non linear terms updated on the main grid, and into a quasi-linear pressure subsystem where the linear part of the momentum equation is integrated on the dual grid.

2.2.1 Explicit Discretization of the Nonlinear Convective Terms

In the numerical scheme proposed in this paper, the convective subsystem

$$\frac{\partial \mathbf{Q}}{\partial t} + \frac{\partial \mathbf{F}^c(\mathbf{Q})}{\partial x} = 0 \quad (9)$$

is integrated using an *explicit* Runge-Kutta discontinuous Galerkin (RKDG) scheme on the main grid, based on a third order TVD Runge-Kutta method [50]. For this purpose, we define the discrete solution for the vector \mathbf{Q} within an element T_i as

$$\mathbf{Q}_i(t) = \phi_l(x) \hat{\mathbf{Q}}_{i,l}(t), \quad (10)$$

where we assume the Einstein summation convention over repeated indices. Multiplication of Eq. (9) with a test function ϕ_k , integration over the primary control volume T_i with subsequent integration by parts and introduction of a numerical flux lead to the following semi-discrete method

$$\int_{T_i} \phi_k(x) \frac{\partial \mathbf{Q}_i}{\partial t} dx + \phi_k \left(x_{i+\frac{1}{2}} \right) \mathbf{F}_{i+\frac{1}{2}}^c - \phi_k \left(x_{i-\frac{1}{2}} \right) \mathbf{F}_{i-\frac{1}{2}}^c - \int_{T_i} \frac{\partial \phi_k}{\partial x} \mathbf{F}^c(\mathbf{Q}_i) dx = 0. \quad (11)$$

The numerical fluxes $\mathbf{F}_{i \pm \frac{1}{2}}^c$ at the cell interfaces $x_{i \pm \frac{1}{2}}$ are given by a local Lax–Friedrichs (Rusanov) Riemann solver

$$\mathbf{F}_{i+\frac{1}{2}}^c = \frac{1}{2} \left(\mathbf{F}^c \left(\mathbf{Q}_{i+\frac{1}{2}}^+ \right) + \mathbf{F}^c \left(\mathbf{Q}_{i+\frac{1}{2}}^- \right) \right) - \frac{1}{2} s_{\max} \left(\mathbf{Q}_{i+\frac{1}{2}}^+ - \mathbf{Q}_{i+\frac{1}{2}}^- \right), \quad (12)$$

where $\mathbf{Q}_{i \pm \frac{1}{2}}^\pm$ are the boundary extrapolated values at the element interfaces from the right and left, respectively. Since in this explicit part of the scheme we only consider the convective subsystem, the maximal signal speed s_{\max} is given by the eigenvalues λ^c of the convective flux \mathbf{F}^c , i.e.

$$s_{\max} = \max \left(\max \left| \lambda^c \left(\mathbf{Q}_{i+\frac{1}{2}}^+ \right) \right|, \max \left| \lambda^c \left(\mathbf{Q}_{i+\frac{1}{2}}^- \right) \right| \right) = \max \left(\left| u_{i+\frac{1}{2}}^+ \right|, \left| u_{i+\frac{1}{2}}^- \right| \right). \quad (13)$$

After integration with a third order TVD Runge-Kutta scheme [50] the degrees of freedom of the conservative variables of the convective subsystem at the new time are denoted by $\widehat{\mathbf{Q}}^*$ and read as follows:¹

$$\begin{aligned}\widehat{\mathbf{k}}_1 &= \widehat{\mathbf{Q}}^n + \Delta t \mathbf{L}_h(\widehat{\mathbf{Q}}^n), \\ \widehat{\mathbf{k}}_2 &= \frac{3}{4} \widehat{\mathbf{Q}}^n + \frac{1}{4} \widehat{\mathbf{k}}_1 + \frac{1}{4} \Delta t \mathbf{L}_h(\widehat{\mathbf{k}}_1), \\ \widehat{\mathbf{Q}}^* &= \frac{1}{3} \widehat{\mathbf{Q}}^n + \frac{2}{3} \widehat{\mathbf{k}}_2 + \frac{2}{3} \Delta t \mathbf{L}_h(\widehat{\mathbf{k}}_2).\end{aligned}\quad (14)$$

In Eq. (14) the spatial discretization operator $\mathbf{L}_h(\widehat{\mathbf{Q}})$ is defined for each element T_i as

$$\mathbf{L}_h(\widehat{\mathbf{Q}})|_{T_i} = -\frac{1}{\Delta x} \mathbf{M}^{-1} \left(\boldsymbol{\varphi}(1) \mathbf{F}_{i+\frac{1}{2}}^c - \boldsymbol{\varphi}(0) \mathbf{F}_{i-\frac{1}{2}}^c - \int_0^1 \boldsymbol{\varphi}'(\xi) \boldsymbol{\varphi}(\xi) d\xi \cdot \widehat{\mathbf{F}}_i^c \right), \quad (15)$$

with the element mass matrix on the reference element given by

$$\mathbf{M} = \int_0^1 \boldsymbol{\varphi} \boldsymbol{\varphi} d\xi = \int_0^1 \varphi_k \varphi_l d\xi, \quad (16)$$

and the vector of degrees of freedom of the convective flux simply defined as $\widehat{\mathbf{F}}_i^c = \mathbf{F}^c(\widehat{\mathbf{Q}}_i)$, since we use an orthogonal nodal basis.

2.2.2 Derivation of the Semi-implicit Staggered DG Scheme in 1D

We first discretize the total energy equation obtained after the flux splitting procedure (5). We multiply the total energy equation by the vector of test functions $\boldsymbol{\phi}$ and we integrate over a control volume of the main grid T_i :

$$\int_{x_{i-\frac{1}{2}}}^{x_{i+\frac{1}{2}}} \boldsymbol{\phi} \left(\frac{\partial}{\partial t} (\rho e + \rho k) + \frac{\partial}{\partial x} (\rho k u + h \rho u) \right) dx = 0. \quad (17)$$

In the time derivative, the term of the total energy term at t^{n+1} is divided considering the contribution of the specific internal energy and the one of the kinetic energy; in addition we make use of the term $\widehat{\rho E}_i^*$ that has been obtained after the explicit discretization of the nonlinear convective terms discussed before. Then, we integrate the spatial derivative by parts in space and, in order to achieve second order of accuracy in time, we use the so-called θ -method. This leads to

$$\begin{aligned}& \left(\int_{x_{i-\frac{1}{2}}}^{x_{i+\frac{1}{2}}} \boldsymbol{\phi} \boldsymbol{\phi} dx \right) \cdot \left(\frac{\widehat{\rho e}_i^{n+1} + \widehat{\rho k}_i^{n+1} - \widehat{\rho E}_i^*}{\Delta t} \right) \\ &+ \boldsymbol{\phi} \left(x_{i+\frac{1}{2}}^- \right) \boldsymbol{\psi} \left(x_{i+\frac{1}{2}} \right) \boldsymbol{\psi} \left(x_{i+\frac{1}{2}} \right) \cdot \widehat{\mathbf{h}}_{i+\frac{1}{2}}^{n+\theta_{i+\frac{1}{2}}} \widehat{\rho \mathbf{u}}_{i+\frac{1}{2}}^{n+\theta_{i+\frac{1}{2}}} - \boldsymbol{\phi} \left(x_{i-\frac{1}{2}}^+ \right) \boldsymbol{\psi} \left(x_{i-\frac{1}{2}} \right) \boldsymbol{\psi} \left(x_{i-\frac{1}{2}} \right) \cdot \widehat{\mathbf{h}}_{i-\frac{1}{2}}^{n+\theta_{i-\frac{1}{2}}} \widehat{\rho \mathbf{u}}_{i-\frac{1}{2}}^{n+\theta_{i-\frac{1}{2}}} \\ &- \left(\int_{x_{i-\frac{1}{2}}}^{x_i} \frac{\partial \boldsymbol{\phi}}{\partial x} \boldsymbol{\psi} \boldsymbol{\psi} dx \right) \cdot \widehat{\mathbf{h}}_{i-\frac{1}{2}}^{n+\theta_{i-\frac{1}{2}}} \widehat{\rho \mathbf{u}}_{i-\frac{1}{2}}^{n+\theta_{i-\frac{1}{2}}} - \left(\int_{x_i}^{x_{i+\frac{1}{2}}} \frac{\partial \boldsymbol{\phi}}{\partial x} \boldsymbol{\psi} \boldsymbol{\psi} dx \right) \cdot \widehat{\mathbf{h}}_{i+\frac{1}{2}}^{n+\theta_{i+\frac{1}{2}}} \widehat{\rho \mathbf{u}}_{i+\frac{1}{2}}^{n+\theta_{i+\frac{1}{2}}} = 0,\end{aligned}\quad (18)$$

¹ When the index i is omitted in the vector of degrees of freedom we intend the entire set of all degrees of freedom of all elements.

where $\widehat{\rho u}_{i+\frac{1}{2}}^{n+\theta_{i+\frac{1}{2}}} = (1 - \theta_{i+\frac{1}{2}})\widehat{\rho u}_{i+\frac{1}{2}}^n + \theta_{i+\frac{1}{2}}\widehat{\rho u}_{i+\frac{1}{2}}^{n+1}$ and $0.5 \leq \theta \leq 1$ is an implicitness parameter. When $\theta = 1$ the scheme is the implicit Euler scheme which is first order accurate in time; when $\theta = 0.5$ we have the second-order Crank-Nicolson time discretization [15]. According to the Godunov theorem [49], in this last case the method is not monotone and can generate unphysical oscillations in the vicinity of strong discontinuities. As we will see later, in the framework of sub-cell FV limiters for semi-implicit DG schemes (see [55]) we therefore want to vary the parameter θ in the domain and this is done assigning different values of θ on the dual mesh. Equation (18) can be rewritten in the compact matrix-vector form

$$\mathbf{M} \cdot (\widehat{\rho e}_i^{n+1} + \widehat{\rho k}_i^{n+1} - \widehat{\rho E}_i^*) + \frac{\Delta t}{\Delta x} \left(\mathbf{R}_e^{\text{DG}} \cdot \widehat{h}_{i+\frac{1}{2}}^{n+\theta_{i+\frac{1}{2}}} \widehat{\rho u}_{i+\frac{1}{2}}^{n+\theta_{i+\frac{1}{2}}} - \mathbf{L}_e^{\text{DG}} \cdot \widehat{h}_{i-\frac{1}{2}}^{n+\theta_{i-\frac{1}{2}}} \widehat{\rho u}_{i-\frac{1}{2}}^{n+\theta_{i-\frac{1}{2}}} \right) = 0. \quad (19)$$

where $\mathbf{R}_e^{\text{DG}} \cdot \widehat{h}_{i+\frac{1}{2}}^{n+\theta_{i+\frac{1}{2}}} \widehat{\rho u}_{i+\frac{1}{2}}^{n+\theta_{i+\frac{1}{2}}}$ is the product of a rank 3 tensor \mathbf{R}_e^{DG} with the degrees of freedom $\widehat{h}_{i+\frac{1}{2}}^{n+\theta_{i+\frac{1}{2}}} \widehat{\rho u}_{i+\frac{1}{2}}^{n+\theta_{i+\frac{1}{2}}}$. Moving the quantities of Eq. (19) at time t^n to the right hand side yields

$$\begin{aligned} & \mathbf{M} \cdot \frac{\widehat{p}_i^{n+1}}{\gamma - 1} + \mathbf{M} \cdot \widehat{\rho k}_i^{n+1} + \frac{\Delta t}{\Delta x} \left(\theta_{i+\frac{1}{2}} \mathbf{R}_e^{\text{DG}} \cdot \widehat{h}_{i+\frac{1}{2}}^{n+1} \widehat{\rho u}_{i+\frac{1}{2}}^{n+1} - \theta_{i-\frac{1}{2}} \mathbf{L}_e^{\text{DG}} \cdot \widehat{h}_{i-\frac{1}{2}}^{n+1} \widehat{\rho u}_{i-\frac{1}{2}}^{n+1} \right) \\ &= \mathbf{M} \cdot \widehat{\rho E}_i^* - \frac{\Delta t}{\Delta x} \left((1 - \theta_{i+\frac{1}{2}}) \mathbf{R}_e^{\text{DG}} \cdot \widehat{h}_{i+\frac{1}{2}}^n \widehat{\rho u}_{i+\frac{1}{2}}^n - (1 - \theta_{i-\frac{1}{2}}) \mathbf{L}_e^{\text{DG}} \cdot \widehat{h}_{i-\frac{1}{2}}^n \widehat{\rho u}_{i-\frac{1}{2}}^n \right) \end{aligned} \quad (20)$$

where we expressed the internal energy e as function of p using the ideal gas equation of state. In addition, the meaning of the symbol under-tilde will be clarified later. The momentum equation is multiplied by the test function ψ and it is integrated over a control volume $T_{i+\frac{1}{2}}$ that belongs to the dual grid

$$\int_{x_i}^{x_{i+1}} \psi \left(\frac{\partial \rho u}{\partial t} + \frac{\partial \rho u^2}{\partial x} \right) dx = - \int_{x_i}^{x_{i+1}} \psi \frac{\partial p}{\partial x} dx. \quad (21)$$

We carry out the integration of (21) following the same procedure used in [35, 54, 55, 79]. The nonlinear convective terms have already been discretized explicitly, leading to $\widehat{\rho u}_{i+\frac{1}{2}}^*$, while the pressure gradient is approximated by splitting it into a smooth contribution and a jump term across the interfaces of the primary grid, which are located in the interior of the dual mesh. This yields

$$\begin{aligned} & \left(\int_{x_i}^{x_{i+1}} \psi \psi dx \right) \cdot \left(\frac{\widehat{\rho u}_{i+\frac{1}{2}}^{n+1} - \widehat{\rho u}_{i+\frac{1}{2}}^*}{\Delta t} \right) = - \psi \left(x_{i+\frac{1}{2}} \right) \left(\phi \left(x_{i+\frac{1}{2}}^+ \right) \cdot \widehat{p}_{i+1}^{n+\theta_{i+\frac{1}{2}}} - \phi \left(x_{i+\frac{1}{2}}^- \right) \cdot \widehat{p}_i^{n+\theta_{i-\frac{1}{2}}} \right) \\ & \quad - \left(\int_{x_i}^{x_{i+\frac{1}{2}}^-} \psi \frac{\partial \phi}{\partial x} dx \right) \cdot \widehat{p}_i^{n+\theta_{i-\frac{1}{2}}} - \left(\int_{x_{i+\frac{1}{2}}^+}^{x_{i+1}} \psi \frac{\partial \phi}{\partial x} dx \right) \cdot \widehat{p}_{i+1}^{n+\theta_{i+\frac{1}{2}}} \end{aligned} \quad (22)$$

and the more compact matrix-tensor formulation of the same equation reads as follows:

$$\mathbf{M} \cdot \left(\widehat{\rho u}_{i+\frac{1}{2}}^{n+1} - \widehat{\rho u}_{i+\frac{1}{2}}^* \right) + \frac{\Delta t}{\Delta x} \left(\mathbf{R}_p^{\text{DG}} \cdot \widehat{p}_{i+1}^{n+\theta_{i+\frac{1}{2}}} - \mathbf{L}_p^{\text{DG}} \cdot \widehat{p}_i^{n+\theta_{i+\frac{1}{2}}} \right) = 0. \quad (23)$$

Later on, we introduce the term $\widehat{G}_{i+\frac{1}{2}}^n$ that collects the convective terms of the momentum equation and the discrete pressure gradient at the time level t^n

$$\widehat{G}_{i+\frac{1}{2}}^n = \widehat{\rho u}_{i+\frac{1}{2}}^* - \frac{\Delta t}{\Delta x} (1 - \theta_{i+\frac{1}{2}}) \mathbf{M}^{-1} \cdot \left(\mathbf{R}_p^{\text{DG}} \cdot \widehat{p}_{i+1}^n - \mathbf{L}_p^{\text{DG}} \cdot \widehat{p}_i^n \right), \quad (24)$$

so that the final semi-implicit momentum equation reads

$$\widehat{\rho u}_{i+\frac{1}{2}}^{n+1} = \widehat{G}_{i+\frac{1}{2}}^n - \frac{\Delta t}{\Delta x} \theta_{i+\frac{1}{2}} \mathbf{M}^{-1} \cdot \left(\mathbf{R}_p^{\text{DG}} \cdot \widehat{p}_{i+1}^{n+1} - \mathbf{L}_p^{\text{DG}} \cdot \widehat{p}_i^{n+1} \right). \quad (25)$$

Later, we will insert the discrete momentum equation (25) into the discrete total energy equation (20). However, the enthalpy h is a function of the pressure, and in order to avoid a strongly non-linear system in p we adopt an iterative *Picard* technique. Hence, the symbol under-tilde means that a variable is evaluated at the previous Picard iteration. In the following we will use the superscript r as the iteration index of the Picard process. For the sake of clarity we rewrite Eq. (20) as

$$\begin{aligned} & \mathbf{M} \cdot \frac{\widehat{p}_i^{n+1,r+1}}{\gamma - 1} + \frac{\Delta t}{\Delta x} \left(\theta_{i+\frac{1}{2}} \mathbf{R}_e^{\text{DG}} \cdot \widehat{h}_{i+\frac{1}{2}}^{n+1,r} \widehat{\rho u}_{i+\frac{1}{2}}^{n+1,r+1} - \theta_{i-\frac{1}{2}} \mathbf{L}_e^{\text{DG}} \cdot \widehat{h}_{i-\frac{1}{2}}^{n+1,r} \widehat{\rho u}_{i-\frac{1}{2}}^{n+1,r+1} \right) \\ &= \mathbf{M} \cdot (\widehat{\rho E}_i^* - \widehat{\rho k}_i^{n+1,r}) \\ & - \frac{\Delta t}{\Delta x} \left((1 - \theta_{i+\frac{1}{2}}) \mathbf{R}_e^{\text{DG}} \cdot \widehat{h}_{i+\frac{1}{2}}^n \widehat{\rho u}_{i+\frac{1}{2}}^n - (1 - \theta_{i-\frac{1}{2}}) \mathbf{L}_e^{\text{DG}} \cdot \widehat{h}_{i-\frac{1}{2}}^n \widehat{\rho u}_{i-\frac{1}{2}}^n \right). \end{aligned} \quad (26)$$

The discrete momentum equation (25) becomes

$$\widehat{\rho u}_{i+\frac{1}{2}}^{n+1,r+1} = \widehat{G}_{i+\frac{1}{2}}^n - \frac{\Delta t}{\Delta x} \theta_{i+\frac{1}{2}} \mathbf{M}^{-1} \cdot \left(\mathbf{R}_p^{\text{DG}} \cdot \widehat{p}_{i+1}^{n+1,r+1} - \mathbf{L}_p^{\text{DG}} \cdot \widehat{p}_i^{n+1,r+1} \right). \quad (27)$$

Therefore, after inserting (27) into (26) one gets a discrete wave equation for the unknown pressure $p^{n+1,r+1}$ at the next Picard iteration, which can be solved by using a Thomas algorithm for linear block three-diagonal systems, and which reads

$$\mathcal{L}_i^{\text{DG}} \cdot \widehat{p}_{i-1}^{n+1,r+1} + \mathcal{C}_i^{\text{DG}} \cdot \widehat{p}_i^{n+1,r+1} + \mathcal{R}_i^{\text{DG}} \cdot \widehat{p}_{i+1}^{n+1,r+1} = \widehat{b}_i^r. \quad (28)$$

Here, \widehat{b}_i^r is the known right hand side term

$$\begin{aligned} \widehat{b}_i^r = & \mathbf{M} \cdot (\widehat{\rho E}_i^* - \widehat{\rho k}_i^{n+1,r} \widehat{h}_i^{n+1,r}) - \frac{\Delta t}{\Delta x} \left(\theta_{i+\frac{1}{2}} \mathbf{R}_e^{\text{DG}} \cdot \widehat{h}_{i+\frac{1}{2}}^{n+1,r} \widehat{\rho u}_{i+\frac{1}{2}}^* - \theta_{i-\frac{1}{2}} \mathbf{L}_e^{\text{DG}} \cdot \widehat{h}_{i-\frac{1}{2}}^{n+1,r} \widehat{\rho u}_{i-\frac{1}{2}}^* \right) \\ & - \frac{\Delta t}{\Delta x} \left((1 - \theta_{i+\frac{1}{2}}) \mathbf{R}_e^{\text{DG}} \cdot \widehat{h}_{i+\frac{1}{2}}^n \widehat{\rho u}_{i+\frac{1}{2}}^n - (1 - \theta_{i-\frac{1}{2}}) \mathbf{L}_e^{\text{DG}} \cdot \widehat{h}_{i-\frac{1}{2}}^n \widehat{\rho u}_{i-\frac{1}{2}}^n \right). \end{aligned} \quad (29)$$

The block matrices $\mathcal{L}_i^{\text{DG}}$, $\mathcal{C}_i^{\text{DG}}$ and $\mathcal{R}_i^{\text{DG}}$ read

$$\mathcal{L}_i^{\text{DG}} = -\frac{\Delta t^2}{\Delta x^2} \theta_{i-\frac{1}{2}}^2 \mathbf{L}_e^{\text{DG}} \widehat{h}_{i-\frac{1}{2}}^{n+1,r} \mathbf{M}^{-1} \mathbf{L}_p^{\text{DG}}, \quad (30)$$

$$\begin{aligned} \mathcal{C}_i^{\text{DG}} = & \frac{1}{\gamma - 1} \mathbf{M} + \frac{\Delta t^2}{\Delta x^2} \theta_{i+\frac{1}{2}}^2 \mathbf{R}_e^{\text{DG}} \widehat{h}_{i+\frac{1}{2}}^{n+1,r} \mathbf{M}^{-1} \mathbf{L}_p^{\text{DG}} + \frac{\Delta t^2}{\Delta x^2} \theta_{i-\frac{1}{2}}^2 \mathbf{L}_e^{\text{DG}} \widehat{h}_{i-\frac{1}{2}}^{n+1,r} \mathbf{M}^{-1} \mathbf{R}_p^{\text{DG}}, \\ & \end{aligned} \quad (31)$$

$$\mathcal{R}_i^{\text{DG}} = -\frac{\Delta t^2}{\Delta x^2} \theta_{i+\frac{1}{2}}^2 \mathbf{R}_{\mathbf{e}}^{\text{DG}} \hat{\mathbf{h}}_{i+\frac{1}{2}}^{n+1,r} \mathbf{M}^{-1} \mathbf{R}_{\mathbf{p}}^{\text{DG}}. \quad (32)$$

For every Picard iteration, once the pressure is known, the momentum update is done using Eq. (27). Subsequently, also the enthalpy $\hat{\mathbf{h}}_{i+\frac{1}{2}}^{n+1,r+1}$ has to be computed and, in order to get a quantity from the main grid to the dual one and back, we use the following averaging operator based on L_2 projection:

$$\hat{\mathbf{p}}_{i+\frac{1}{2}} = \mathbf{M}^{-1} \cdot (\mathbf{M}_{\mathbf{L}}^{\text{DG}} \cdot \hat{\mathbf{p}}_i + \mathbf{M}_{\mathbf{R}}^{\text{DG}} \cdot \hat{\mathbf{p}}_{i+1}). \quad (33)$$

In addition, since in Eq. (29) the kinetic energy is needed on the main grid, we first compute the degrees of freedom of the velocity as $\hat{\mathbf{u}}_{i+\frac{1}{2}}^{n+1,r+1} = \hat{\rho} \hat{\mathbf{u}}_{i+\frac{1}{2}}^{n+1,r+1} / \hat{\rho}_{i+\frac{1}{2}}^{n+1}$ and then we apply the L_2 averaging operator from the dual to the main grid

$$\hat{\mathbf{u}}_i = \mathbf{M}^{-1} \cdot \left(\mathbf{M}_{\mathbf{L}}^{\text{DG}} \cdot \hat{\mathbf{u}}_{i-\frac{1}{2}} + \mathbf{M}_{\mathbf{R}}^{\text{DG}} \cdot \hat{\mathbf{u}}_{i+\frac{1}{2}} \right). \quad (34)$$

The tensors $\mathbf{M}_{\mathbf{L}}^{\text{DG}}$ and $\mathbf{M}_{\mathbf{R}}^{\text{DG}}$ are given in “Appendix A.3”. The discrete momentum on the main grid can be computed as $\hat{\rho} \hat{\mathbf{u}}_i^{n+1,r+1} = \hat{\rho}_i^{n+1,r+1} \hat{\mathbf{u}}_i^{n+1,r+1}$ or using a L_2 average like Eq. (34). Numerical experiments indicate that only very few Picard iterations, typically 2 or 3, are enough to obtain a good solution. Finally, at the end of the Picard loop the update of the total energy is carried out and from Eq. (19) we get

$$\widehat{\rho E}_i^{n+1} = \widehat{\rho E}_i^* - \frac{\Delta t}{\Delta x} \mathbf{M}^{-1} \cdot \left(\mathbf{R}_{\mathbf{e}}^{\text{DG}} \cdot \hat{\mathbf{h}}_{i+\frac{1}{2}}^{n+\theta_{i+\frac{1}{2}}} \widehat{\rho} \widehat{\mathbf{u}}_{i+\frac{1}{2}}^{n+\theta_{i+\frac{1}{2}}} - \mathbf{L}_{\mathbf{e}}^{\text{DG}} \cdot \hat{\mathbf{h}}_{i-\frac{1}{2}}^{n+\theta_{i-\frac{1}{2}}} \widehat{\rho} \widehat{\mathbf{u}}_{i-\frac{1}{2}}^{n+\theta_{i-\frac{1}{2}}} \right). \quad (35)$$

For this semi-implicit DG scheme, the maximum time step is given by the usual CFL condition of the RKDG scheme which reads

$$\Delta t < \text{CFL} \frac{\Delta x}{\max(|u|)} \quad \text{with} \quad \text{CFL} < (2P + 1)^{-1}. \quad (36)$$

Note that this is the stability condition due to the explicit discretization of the nonlinear convective terms and which is based only on the fluid velocity. Due to the implicit treatment of the pressure terms, the speed of sound does not influence the choice of Δt . Consequently, this method becomes suitable for the numerical simulation of low Mach number flows. However, due to its conservative formulation, the method is also able to deal with shock waves, as shown later. For other types of semi-implicit DG schemes on staggered meshes, the reader is referred to [35, 44, 45, 54, 76, 78, 79]. In addition, the scheme derived here represents the natural extension to arbitrary order of accuracy in space of the semi-implicit 1D finite volume method introduced in [36].

2.3 A Sub-cell Formulation for the Semi-implicit Finite Volume Method for the 1D Euler Equations

In this subsection we introduce a sub-cell formulation of the semi-implicit finite volume method for the 1D Euler equations. In particular this approach was adopted in [55] for the shallow water equations but other similar methods have been proposed also in [12, 60, 74]. The computational domain is $\Omega_x = [x_L, x_R]$ and, similarly to the method in Sect. 2.2, we consider two staggered meshes. For an element T_i of the main grid, given a positive integer P , there are $2P + 1$ piecewise constant sub-cell averages that represent the FV data on $2P + 1$ sub-cells $T_{i,s}$ characterized by length $\Delta x_s = \Delta x / (2P + 1)$. Consequently we have that

$T_i = \cup_s T_{i,s}$ with $s = 1, \dots, (2P + 1)$. Hence, for $P = 2$, $\bar{\mathbf{p}}_i = [\bar{p}_{i,1}, \bar{p}_{i,2}, \bar{p}_{i,3}, \bar{p}_{i,4}, \bar{p}_{i,5}]$ denotes the set of sub-cell data in the cell T_i . For a schematic representation of these grids see Fig. 2. The quantities assigned to the main grid and to the dual grid are the same discussed in the previous Sect. 2.2. For the convective sub-system, the explicit finite volume update on a collocated grid at the subcell level is given by

$$\bar{\mathbf{Q}}_{i,s}^* = \bar{\mathbf{Q}}_{i,s}^n - \frac{\Delta t}{\Delta x_s} \left(\mathbf{F}_{i,s+\frac{1}{2}}^c - \mathbf{F}_{i,s-\frac{1}{2}}^c \right), \quad (37)$$

where we used again the Rusanov method in order to evaluate the numerical fluxes $\mathbf{F}_{i,s \pm \frac{1}{2}}^c$. We start with the semi-implicit approximation of the momentum equation. Using the adaptive θ -method, the discretization reads as follows

$$\left(\bar{\rho} \bar{\mathbf{u}}_{i+\frac{1}{2}}^{n+1} - \bar{\rho} \bar{\mathbf{u}}_{i+\frac{1}{2}}^* \right) + \frac{\Delta t}{\Delta x} \left(\mathbf{R}^{\text{FV}} \cdot \bar{\mathbf{p}}_{i+1}^{n+\theta_{i+\frac{1}{2}}} - \mathbf{L}^{\text{FV}} \cdot \bar{\mathbf{p}}_i^{n+\theta_{i+\frac{1}{2}}} \right) = 0 \quad (38)$$

where $\bar{\rho} \bar{\mathbf{u}}_{i+\frac{1}{2}}^*$ is the contribution of the explicit discretization of the nonlinear convective term; in addition, the tensors \mathbf{R}^{FV} and \mathbf{L}^{FV} (see “Appendix A.2”) approximate the derivative in x -direction. For the sake of clarity, we give the approximation of the pressure gradient $\Delta x \partial p / \partial x$ with $P = 2$ and $\theta_{i \pm \frac{1}{2}} = 1$:

$$\begin{aligned} & \mathbf{R}^{\text{FV}} \cdot \bar{\mathbf{p}}_{i+\frac{1}{2}}^{n+1} - \mathbf{L}^{\text{FV}} \cdot \bar{\mathbf{p}}_{i-\frac{1}{2}}^{n+1} \\ &= 5 \left(\bar{p}_{i-\frac{1}{2},4}^{n+1} - \bar{p}_{i-\frac{1}{2},3}^{n+1} \bar{p}_{i-\frac{1}{2},5}^{n+1} - \bar{p}_{i-\frac{1}{2},4}^{n+1}, \bar{p}_{i+\frac{1}{2},1}^{n+1} - \bar{p}_{i-\frac{1}{2},5}^{n+1}, \bar{p}_{i+\frac{1}{2},2}^{n+1} - \bar{p}_{i+\frac{1}{2},1}^{n+1}, \bar{p}_{i+\frac{1}{2},3}^{n+1} - \bar{p}_{i+\frac{1}{2},2}^{n+1} \right). \end{aligned} \quad (39)$$

The semi-implicit sub-cell finite volume discretization of the total energy equation takes the form

$$\begin{aligned} & \frac{1}{\gamma - 1} \bar{p}_i^{n+1,r+1} + \frac{\Delta t}{\Delta x} \left(\theta_{i+\frac{1}{2}} \mathbf{R}^{\text{FV}} \cdot \bar{\mathbf{h}}_{i+\frac{1}{2}}^{n+1,r} \bar{\rho} \bar{\mathbf{u}}_{i+\frac{1}{2}}^{n+1,r+1} - \theta_{i-\frac{1}{2}} \mathbf{L}^{\text{FV}} \cdot \bar{\mathbf{h}}_{i-\frac{1}{2}}^{n+1,r} \bar{\rho} \bar{\mathbf{u}}_{i-\frac{1}{2}}^{n+1,r+1} \right) \\ &= \left(\bar{\rho} \bar{\mathbf{E}}_i^* - \bar{\rho}_i^{n+1} \bar{k}_i^{n+1,r} \right) - \frac{\Delta t}{\Delta x} \left((1 - \theta_{i+\frac{1}{2}}) \mathbf{R}^{\text{FV}} \cdot \bar{\mathbf{h}}_{i+\frac{1}{2}}^n \bar{\rho} \bar{\mathbf{u}}_{i+\frac{1}{2}}^n - (1 - \theta_{i-\frac{1}{2}}) \mathbf{L}^{\text{FV}} \cdot \bar{\mathbf{h}}_{i-\frac{1}{2}}^n \bar{\rho} \bar{\mathbf{u}}_{i-\frac{1}{2}}^n \right). \end{aligned} \quad (40)$$

Inserting Eq. (38) into Eq. (40) yields a linear three-diagonal system, which at each Picard level reads

$$\mathcal{L}_i^{\text{FV}} \cdot \bar{\mathbf{p}}_{i-1}^{n+1,r+1} + \mathcal{C}_i^{\text{FV}} \cdot \bar{\mathbf{p}}_i^{n+1,r+1} + \mathcal{R}_i^{\text{FV}} \cdot \bar{\mathbf{p}}_{i+1}^{n+1,r+1} = \bar{\mathbf{b}}_i^r, \quad (41)$$

and which can be solved either by a Thomas algorithm or by an iterative conjugate gradient method. In each Picard iteration the enthalpy, which is defined on the staggered mesh, has to be updated and one can use the following FV average in order to interpolate the pressure from the main grid to the dual mesh

$$\bar{\mathbf{p}}_{i+\frac{1}{2}} = \left(\mathbf{M}_L^{\text{FV}} \cdot \bar{\mathbf{p}}_i + \mathbf{M}_R^{\text{FV}} \cdot \bar{\mathbf{p}}_{i+1} \right). \quad (42)$$

Similarly, the kinetic energy is discretized on the main grid. So, in order to get the degrees of freedom of the velocity $\bar{\mathbf{u}}_i$, the projection from the dual grid to main one reads

$$\bar{\mathbf{u}}_i = \left(\mathbf{M}_L^{\text{FV}} \cdot \bar{\mathbf{u}}_{i-\frac{1}{2}} + \mathbf{M}_R^{\text{FV}} \cdot \bar{\mathbf{u}}_{i+\frac{1}{2}} \right). \quad (43)$$

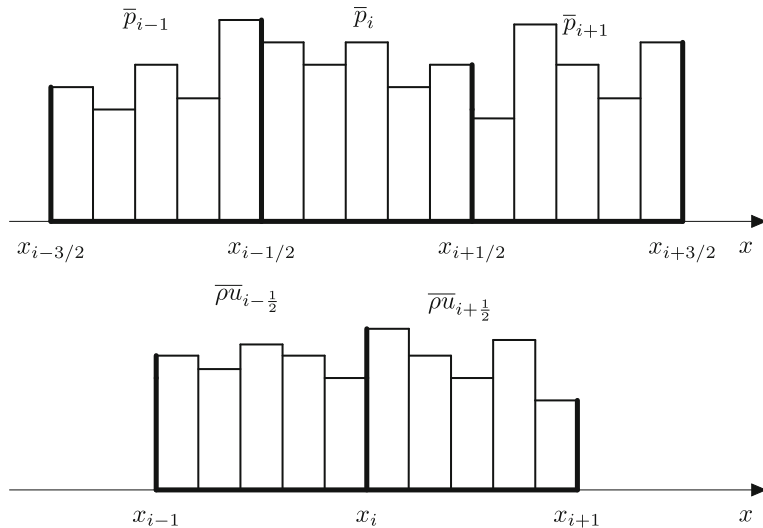


Fig. 2 Staggered grids for the sub-cell finite volume scheme in one dimension in the case $P = 2$ ($N_s = 5$). Main grid used for the free surface (top) and staggered dual mesh for the velocity (bottom)

For the matrices introduced in Eqs. (42) and (43), see “Appendix A.2”. Finally, the total energy update reads

$$\overline{\rho E}_i^{n+1} = \overline{\rho E}_i^* - \frac{\Delta t}{\Delta x} \cdot \left(\mathbf{R}^{\text{FV}} \cdot \bar{h}_{i+\frac{1}{2}}^{n+\theta_{i+\frac{1}{2}}} \overline{\rho u}_{i+\frac{1}{2}}^{n+\theta_{i+\frac{1}{2}}} - \mathbf{L}^{\text{FV}} \cdot \bar{h}_{i-\frac{1}{2}}^{n+\theta_{i-\frac{1}{2}}} \overline{\rho u}_{i-\frac{1}{2}}^{n+\theta_{i-\frac{1}{2}}} \right). \quad (44)$$

Note that, for the ideal gas EOS, in our numerical method the resulting pressure system is always *linear*. It remains linear also for general EOS where the internal energy density ρe is still a *linear* function of pressure. The pressure system would become nonlinear only for those real gas EOS, where the internal energy density ρe is a nonlinear function of the pressure p . The Picard procedure is needed in our approach in order to update the kinetic energy at the new time level, as well as the enthalpy that is needed in the energy flux, see [36] for a more detailed discussion.

The CFL condition of the scheme is given by the stability condition for the computation of the explicit nonlinear convective terms:

$$\Delta t < \text{CFL} \frac{\Delta x_s}{\max(|u|)} \quad \text{with} \quad \text{CFL} < 1. \quad (45)$$

We remind that here we introduced an alternative data representation for the FV method which is necessary in order to combine the DG and FV schemes on staggered meshes for the *a posteriori* limiting strategy introduced in the next section. For the method discussed in this subsection, the solution algorithm is the same adopted for the 1D pure DG scheme in Sect. 2.2. For a better understanding of this particular semi-implicit FV method see [36, 55].

2.4 MOOD Algorithm and Detection Criteria: 1D Case

In this paper, we employ the limiting strategy proposed in [55] for staggered SIDG schemes in the context of the shallow water equations. Similarly to the *a posteriori* sub-cell limiter

for explicit DG schemes exposed in [7, 39, 42], the starting point is the MOOD paradigm [23, 29, 30, 65]: at each time step the algorithm is composed of two stages. In the first one, the unlimited DG scheme presented in Sect. 2.2 generates a so-called *candidate solution* $\mathbf{Q}^{\circ,n+1} = (\rho^{\circ,n+1}, \rho u^{\circ,n+1}, \rho E^{\circ,n+1})^T$ at time t^{n+1} . Then, the troubled zones are detected using physical and numerical admissibility criteria. In the cells flagged as troubled zones, the more robust staggered semi-implicit finite volume subcell scheme introduced in the previous Sect. 2.3 is used, while we continue using the unlimited high order DG method in those control volumes which are not troubled. Afterwards, in the second part of the procedure, a valid solution at time t^n is recovered and then the update is carried out by a *mixed* scheme, which uses the more robust subcell finite volume method in troubled cells and the unlimited DG method in the other ones. To do this, the linear system for the pressure is reassembled and solved again. Moreover, if no troubled cells have been identified after the first stage of the algorithm, the scheme directly proceeds to the next time level.

2.4.1 Data Representation, Projection and Reconstruction

For a generic variable q of the approximated solution given by the DG scheme in the cell T_i at time t^n , the degrees of freedom used for the piecewise polynomial data representation are denoted by $\hat{\mathbf{q}}_i^n$. Similarly $\bar{\mathbf{q}}_i^n$ denote the piecewise constant cell averages in the subcells $T_{i,s}$. These subcell averages $\bar{\mathbf{q}}_i^n$ are computed from $\hat{\mathbf{q}}_i^n$ using the following L_2 projection

$$\bar{\mathbf{q}}_{i,s}^n = \frac{1}{|T_{i,s}|} \int_{T_{i,s}} \phi_l(x) dx \hat{q}_{i,l}^n, \quad \forall T_{i,s} \in T_i, \quad (46)$$

and consequently we introduce the projection operator \mathcal{P} so that $\bar{\mathbf{q}}_i^n = \mathcal{P} \cdot \hat{\mathbf{q}}_i^n$.

Then, one can gather back the piecewise constant sub-cell averages $\bar{\mathbf{q}}_{i,s}^n$ into the degrees of freedom $\hat{q}_{i,l}^n$ of a high order DG polynomial by solving again (46). However, these procedure leads to an *over-determined* system because there are $2P + 1$ equations for $P + 1$ unknowns. In order to overcome this problem a *constrained least-squares* approach (see [38, 58]) is adopted. In particular, the linear constraint is integral conservation on the big cell T_i (see [42]), i.e.

$$\sum_j |T_{i,s}| \bar{\mathbf{q}}_{i,s}^n = \int_{T_i} \phi_l(x) dx \hat{q}_{i,l}^n. \quad (47)$$

This operation is expressed in a tensorial formulation as $\hat{\mathbf{q}}_i^n = \mathcal{W} \cdot \bar{\mathbf{q}}_i^n$, with $\mathcal{W} \cdot \mathcal{P} = \mathcal{I}$, where \mathcal{I} denotes the identity matrix. Moreover, in some situations we will need to recover a polynomial from $P + 1$ piecewise constant sub-cell data. Here we consider two situations: one is at the left part, $T_i^L = \bigcup_{s=1}^{P+1} T_{i,s}$ (see Fig. 3b), and the other at the right side, $T_i^R = \bigcup_{s=P+1}^{2P+1} T_{i,s}$ (see Fig. 3c). So we introduce the matrices \mathcal{W}_L and \mathcal{W}_R that are computed using reconstruction procedure (46) only on the left and right part of cell T_i . Note that here the least squares procedure is not necessary because now the number of equations is equal to the number of unknowns. For a schematic summary of the projection and reconstruction procedures described above, see Fig. 3a.

2.4.2 Detection Criteria

In this subsection we discuss the physical and numerical admissibility criteria. All the quantities are analyzed on the *main grid* and those variables which are located on the staggered

dual grid are extrapolated onto the main grid. This operation is done by using the algorithm given in Eq. (33).

At first, we want that the candidate solution, given numerically by the unlimited staggered DG scheme, satisfies some *physical admissibility criteria* (PAD). For the Euler equations we check that both density and pressure are positive, hence we require

$$\hat{\rho}_{i,l}^{\circ,n+1} > 0 \quad \text{and} \quad \hat{p}_{i,l}^{\circ,n+1} > 0. \quad (48)$$

In addition, similarly to [7, 39, 42], the detector is supplemented by *numerical admissibility criteria* (NAD) based on a relaxed version of the discrete maximum principle (DMP). For a generic variable q this criterion reads as follows

$$\min_{\forall T_j \in \mathcal{V}_i} (\hat{q}_{j,l}^n) - \delta \leq \hat{q}_{i,l}^{\circ,n+1} \leq \max_{\forall T_j \in \mathcal{V}_i} (\hat{q}_{j,l}^n) + \delta, \quad (49)$$

where $\mathcal{V}_i = \{T_{i-1}, T_i, T_{i+1}\}$ is the set of neighbour cells of T_i , which is the set of Voronoi neighbours in the multidimensional case. In equation (49) we introduce two tolerances: δ is a relaxation parameter that allows some very small oscillations or numerical noise; it reads

$$\delta = \max \left[\delta_0, \epsilon \left(\max_{\forall T_j \in \mathcal{V}_i} (\hat{q}_{j,l}^n) - \min_{\forall T_j \in \mathcal{V}_i} (\hat{q}_{j,l}^n) \right) \right] \quad (50)$$

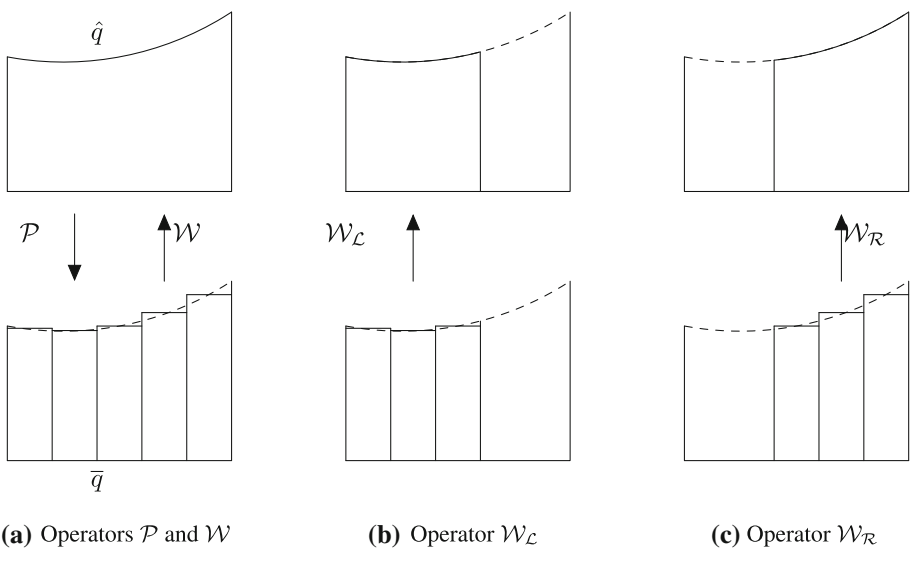
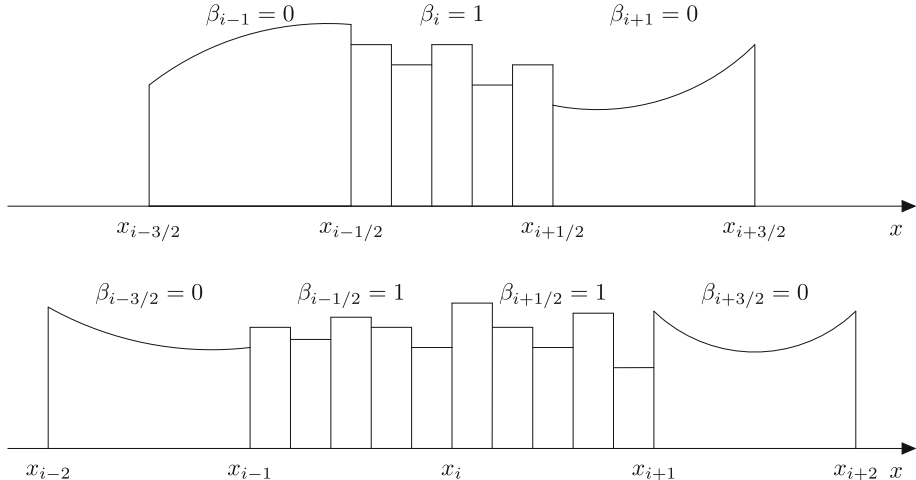
where δ_0 is chosen in the interval $[10^{-4}, 10^{-3}]$ and typically $\epsilon = 5 \cdot 10^{-4}$. In this algorithm we check the DMP componentwise for all conserved variables. Moreover, an additional detection of troubled cells is carried out by projecting all numerical quantities from the main grid to the dual mesh and then projecting them back onto the main grid. This procedure creates non-physical oscillations near discontinuities and thus leads to a more robust detection of troubled cells, especially for the initial condition.

Successively, a cell is flagged as troubled if it does not respect the a posteriori admissibility criteria applied to the candidate solution $\mathbf{Q}^{\circ,n+1}$. We therefore introduce a troubled cell indicator parameter β_i . If $\beta_i = 1$ then a cell is marked as troubled and the solution at time t^{n+1} will be recomputed using the more robust subcell finite volume scheme presented in Sect. 2.3. On the contrary, if $\beta_i = 0$ in T_i it means that the cell is not troubled. In addition, if the cell T_i is flagged as troubled we also mark both dual control volumes $T_{i-\frac{1}{2}}$ and $T_{i+\frac{1}{2}}$ as troubled control volumes, see Fig. 4. As consequence, we impose $\beta_{i-\frac{1}{2}} = 1$ and $\beta_{i+\frac{1}{2}} = 1$.

Finally, for the sake of clarity we remind that in the first MOOD iteration the implicitness parameter θ is a constant value θ_{DG} in the whole domain. It is a user-defined parameter which is typically chosen very close to 1/2 in order to minimize the effects of the numerical viscosity caused by the time integration. At the second MOOD level, the value of the parameter θ in the troubled cells of dual grid is imposed equal to 1. Consequently, the new numerical solution is given by using a monotone and robust finite volume method in the troubled cells.

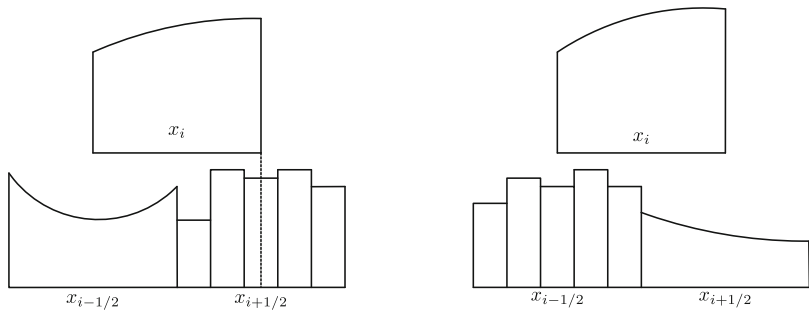
2.5 Sub-cell Limiting of the Semi-implicit DG Scheme for the 1D Euler Equations

Finally, we complete the derivation of the 1D algorithm for the subcell finite volume limiting of the staggered semi-implicit DG scheme for the compressible Euler equations. The computation of the nonlinear convective terms is carried out according to the MOOD strategy used for explicit high order schemes, see [7, 23, 29, 30, 39, 42, 65]. Hence, at the beginning of the first MOOD step all the cells are flagged with $\beta_i = 0$ and the nonlinear convective terms are computing via the high order unlimited RKDG algorithm explained in Sect. 2.2.1. Later on, after the detection of the troubled control volumes, we use the explicit finite volume update

**Fig. 3** Projection and reconstruction operators**Fig. 4** Staggered grids for the semi-implicit staggered DG scheme with sub-cell limiter active in cell T_i . Main grid used for the free surface (top) and staggered dual mesh for the velocity (bottom). If a cell T_i on the main grid is flagged as troubled, then also the two overlapping staggered velocity control volumes $T_{i \pm \frac{1}{2}}$ are flagged as troubled. The data representation in troubled cells is changed from high order polynomials to piecewise constant subcell averages

given in 2.3 in order to recompute the solution in the cells marked with $\beta_i = 1$, while for the cells which are not troubled we keep the results of the first MOOD step.

Now, we consider the semi-implicit approximation of the one-dimensional total energy and momentum equations for the complete algorithm. For the general case we distinguish four situations. The first one is when the control volume T_i and the corresponding dual cells $T_{i \pm}$ are not marked as troubled. In this case $\beta_{i-\frac{1}{2}} = \beta_i = \beta_{i+\frac{1}{2}} = 0$ and the equations are



(a) DG method used in T_i and $T_{i-\frac{1}{2}}$; finite volumes in $T_{i+\frac{1}{2}}$ **(b)** DG method used in T_i and $T_{i+\frac{1}{2}}$; finite volumes in $T_{i-\frac{1}{2}}$.

Fig. 5 Control volumes for the total energy equation for the staggered semi-implicit DG scheme in the limited case using $P = 2$, i.e. $N_s = 2P + 1 = 5$. Finite volume method used in $T_{i+\frac{1}{2}}$ (left) and in $T_{i-\frac{1}{2}}$ (right)

discretized using the pure DG method introduced in Sect. 2.2. The opposite case is when the troubled cell indicator $\beta_{i-\frac{1}{2}} = \beta_i = \beta_{i+\frac{1}{2}} = 1$ is equal to one in all the control volumes $T_{i-\frac{1}{2}}, T_i, T_{i+\frac{1}{2}}$; for this situation, we use the finite volume method discussed in 2.3.

In the following we provide two examples when cell T_i is not troubled but one of its neighbors is marked as troubled. In this case, the discrete energy conservation law reads

$$\mathbf{M} \cdot \left(\frac{\widehat{\rho E}_i^{n+1} - \widehat{\rho E}_i^*}{\Delta t} \right) + \frac{\mathbf{R}_e^{\text{DG}} \cdot \widehat{h}_{i+\frac{1}{2}}^{n+\theta_{i+\frac{1}{2}}} \widehat{\rho u}_{i+\frac{1}{2}}^{n+\theta_{i+\frac{1}{2}}} - \mathbf{L}_e^{\text{Lim}} \cdot \overline{h}_{i-\frac{1}{2}}^{n+\theta_{i-\frac{1}{2}}} \overline{\rho u}_{i-\frac{1}{2}}^{n+\theta_{i-\frac{1}{2}}}}{\Delta x} = 0,$$

with $\mathbf{L}_e^{\text{Lim}} = \mathbf{L}'_e^{\text{DG}} \cdot \mathcal{W}_R$

(51)

for $\beta_i = 0, \beta_{i-1} = 0$ and $\beta_{i+1} = 1$ and

$$\mathbf{M} \cdot \left(\frac{\widehat{\rho E}_i^{n+1} - \widehat{\rho E}_i^*}{\Delta t} \right) + \frac{\mathbf{R}_e^{\text{Lim}} \cdot \overline{h}_{i+\frac{1}{2}}^{n+\theta_{i+\frac{1}{2}}} \overline{\rho u}_{i+\frac{1}{2}}^{n+\theta_{i+\frac{1}{2}}} - \mathbf{L}_e^{\text{DG}} \cdot \widehat{h}_{i-\frac{1}{2}}^{n+\theta_{i-\frac{1}{2}}} \widehat{\rho u}_{i-\frac{1}{2}}^{n+\theta_{i-\frac{1}{2}}}}{\Delta x} = 0,$$

with $\mathbf{R}_e^{\text{Lim}} = \mathbf{R}'_e^{\text{DG}} \cdot \mathcal{W}_L$.

(52)

for $\beta_i = 0, \beta_{i-1} = 1$ and $\beta_{i+1} = 0$. These two approximations are very similar to Eq. (19) the discretization of the energy equation in the pure DG case. In fact, considering the scheme in Fig. 5a, the operator \mathcal{W}_L reconstructs the polynomial data using the first $P + 1$ subcell averages of the cell $T_{i+\frac{1}{2}}$. Similarly \mathcal{W}_R reconstructs the polynomial data from the last $P + 1$ piecewise constant data of the control volume $T_{i-\frac{1}{2}}$, see Fig. 5b. In addition, in equations (51) and (52) we introduced the matrices $\mathbf{R}'_e^{\text{DG}}$ and $\mathbf{L}'_e^{\text{DG}}$ that are rank 2 tensors and which are explicitly given in “Appendix A.3”.

Now we discuss the two limited cases of the discrete momentum equation. Here, we consider the cases when $T_{i+\frac{1}{2}}$ is a troubled cell and only one of the control volumes T_i and T_{i+1} is a limited control volume. Hence the numerical approximation of the momentum equation reads as follows

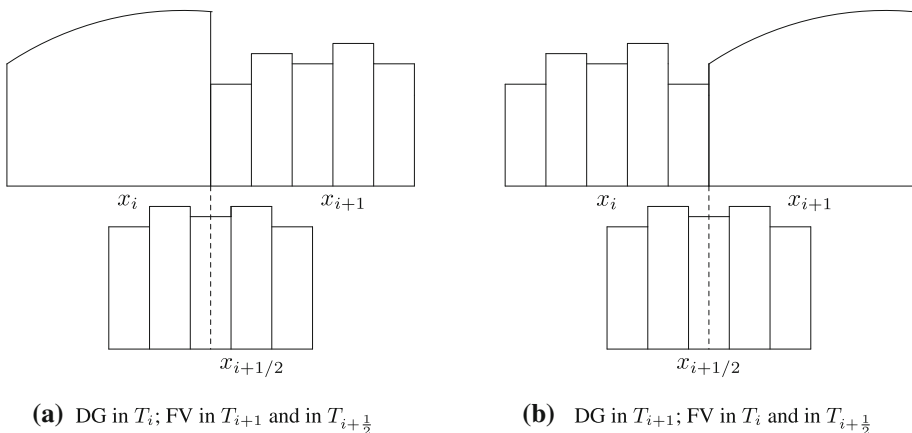


Fig. 6 Control volumes for the momentum equation for the staggered semi-implicit DG scheme in the limited case using $P = 2$ ($N_s = 5$)

$$\overline{\rho u}_{i+\frac{1}{2}}^{n+1} = \overline{\rho u}_{i+\frac{1}{2}}^* - \frac{\Delta t}{\Delta x} \left(\mathbf{R}_u^{\text{Lim}} \cdot \hat{p}_{i+1}^{n+\theta_{i+\frac{1}{2}}} - \mathbf{L}^{\text{FV}} \cdot \overline{p}_i^{n+\theta_{i+\frac{1}{2}}} \right) \quad \text{with } \mathbf{R}_u^{\text{Lim}} = \mathbf{R}^{\text{FV}} \cdot \mathcal{P} \quad (53)$$

when $\beta_i = 0$ and $\beta_{i+1} = 1$ (see Fig. 6a) and

$$\overline{\rho u}_{i+\frac{1}{2}}^{n+1} = \overline{\rho u}_{i+\frac{1}{2}}^* - \frac{\Delta t}{\Delta x} \left(\mathbf{R}^{\text{FV}} \cdot \overline{p}_{i+1}^{n+\theta_{i+\frac{1}{2}}} - \mathbf{L}_u^{\text{Lim}} \cdot \hat{p}_i^{n+\theta_{i+\frac{1}{2}}} \right) \quad \text{with } \mathbf{L}_u^{\text{Lim}} = \mathbf{L}^{\text{FV}} \cdot \mathcal{P} \quad (54)$$

when $\beta_i = 1$ and $\beta_{i+1} = 0$ (see Fig. 6b). Note that Eqs. 53 and 54 can be seen as particular case of the discrete momentum equation (38) for the sub-cell finite volume method. In addition, in Eq. (53), the product $\mathbf{R}_u^{\text{Lim}} \cdot \hat{p}_{i+1}^{n+\theta_{i+\frac{1}{2}}} = \mathbf{R}^{\text{FV}} \cdot \overline{p}_{i+1}^{n+\theta_{i+\frac{1}{2}}}$ is equal to the multiplication of the tensor \mathbf{R}^{FV} with the vector of piecewise constant subcell averages $\overline{p}_{i+1}^{n+\theta_{i+\frac{1}{2}}} = \mathcal{P} \cdot \hat{p}_{i+1}^{n+\theta_{i+\frac{1}{2}}}$ given by the projection of the DG degrees of freedom onto the set of the subcell finite volume degrees of freedom. This observation is valid also for the tensor product $\mathbf{L}_u^{\text{Lim}} \cdot \hat{p}_i^{n+\theta_{i+\frac{1}{2}}} = \mathbf{L}^{\text{FV}} \cdot \overline{p}_i^{n+\theta_{i+\frac{1}{2}}}$ in Eq. (54).

The substitution of the momentum equation into the energy equation yields the following block three-diagonal linear system (55):

$$\mathcal{L}_i^{\text{Lim}} \cdot \tilde{p}_{i-1}^{n+1,r+1} + \mathcal{C}_i^{\text{Lim}} \cdot \tilde{p}_i^{n+1,r+1} + \mathcal{R}_i^{\text{Lim}} \cdot \tilde{p}_{i+1}^{n+1,r+1} = \tilde{b}_i^r. \quad (55)$$

We denote with the symbol \tilde{p}_i^{n+1} the generic degrees of freedom of the pressure which represent either a DG polynomial or a set of subcell averages depending on the value of the troubled cell indicator β .

In the following, we will give the expressions for the blocks $\mathcal{L}_i^{\text{Lim}}$, $\mathcal{C}_i^{\text{Lim}}$, $\mathcal{R}_i^{\text{Lim}}$ and for the right hand side term \tilde{b}_i^r . For clarity, $\mathcal{C}_i^{\text{Lim}}$ is divided in two contributions

$$\mathcal{C}_i^{\text{Lim}} = \mathcal{C}_i^{0,\text{Lim}} + \mathcal{C}_i^{x,\text{Lim}}, \quad (56)$$

where $\mathbf{C}_i^{0,\text{Lim}}$ is equal to the mass matrix in the DG case or equal to the identity for the subcell FV scheme:

$$\mathbf{C}_i^{0,\text{Lim}} = \begin{cases} \mathbf{M} & \text{if } \beta_i = 0, \\ \mathbf{I} & \text{if } \beta_i = 1. \end{cases} \quad (57)$$

The remaining blocks $\mathcal{L}_i^{\text{Lim}}$, $\mathbf{C}_i^x, \text{Lim}$, $\mathcal{L}_i^{\text{Lim}}$ can be expressed considering four different cases depending on the value of β :

$$\mathcal{L}_i^{\text{Lim}} = -\frac{\Delta t^2}{\Delta x^2} \theta_{i-\frac{1}{2}}^2 \begin{cases} \mathbf{L}_e^{\text{DG}} \cdot \hat{\mathbf{h}}_{i-\frac{1}{2}}^{n+1} \cdot \mathbf{M}^{-1} \cdot \mathbf{L}_u^{\text{DG}} & \text{if } \beta_{i-1} = \beta_i = 0, \\ \mathbf{L}^{\text{FV}} \cdot \text{diag}\left(\bar{\mathbf{h}}_{i-\frac{1}{2}}^{n+1}\right) \cdot \mathbf{L}^{\text{FV}} & \text{if } \beta_{i-1} = \beta_i = 1, \\ \mathbf{L}_e^{\text{Lim}} \cdot \text{diag}\left(\bar{\mathbf{h}}_{i-\frac{1}{2}}^{n+1}\right) \cdot \mathbf{L}^{\text{FV}} & \text{if } \beta_{i-1} = 1, \beta_i = 0, \\ \mathbf{L}^{\text{FV}} \cdot \text{diag}\left(\bar{\mathbf{h}}_{i-\frac{1}{2}}^{n+1}\right) \cdot \mathbf{L}_u^{\text{Lim}} & \text{if } \beta_{i-1} = 0, \beta_i = 1, \end{cases} \quad (58)$$

$$\mathbf{C}_i^x, \text{Lim} = \frac{\Delta t^2}{\Delta x^2} \begin{cases} \theta_{i-\frac{1}{2}}^2 \mathbf{R}_e^{\text{DG}} \cdot \hat{\mathbf{h}}_{i-\frac{1}{2}}^{n+1} \cdot \mathbf{M}^{-1} \cdot \mathbf{L}_u^{\text{DG}} + \theta_{i+\frac{1}{2}}^2 \mathbf{L}_e^{\text{DG}} \cdot \hat{\mathbf{h}}_{i+\frac{1}{2}}^{n+1} \cdot \mathbf{M}^{-1} \cdot \mathbf{R}_u^{\text{DG}} & \text{if } \beta_i = \beta_{i-\frac{1}{2}} = \beta_{i+\frac{1}{2}} = 0, \\ \theta_{i-\frac{1}{2}}^2 \mathbf{L}^{\text{FV}} \cdot \text{diag}\left(\bar{\mathbf{h}}_{i-\frac{1}{2}}^{n+1}\right) \cdot \mathbf{R}^{\text{FV}} + \theta_{i+\frac{1}{2}}^2 \mathbf{R}^{\text{FV}} \cdot \text{diag}\left(\bar{\mathbf{h}}_{i+\frac{1}{2}}^{n+1}\right) \cdot \mathbf{L}^{\text{FV}} & \text{if } \beta_i = \beta_{i-\frac{1}{2}} = \beta_{i+\frac{1}{2}} = 1, \\ \theta_{i-\frac{1}{2}}^2 \mathbf{R}_e^{\text{DG}} \cdot \hat{\mathbf{h}}_{i-\frac{1}{2}}^{n+1} \cdot \mathbf{M}^{-1} \cdot \mathbf{L}_u^{\text{DG}} + \theta_{i+\frac{1}{2}}^2 \mathbf{R}_e^{\text{Lim}} \cdot \text{diag}\left(\bar{\mathbf{h}}_{i+\frac{1}{2}}^{n+1}\right) \cdot \mathbf{L}_u^{\text{Lim}} & \text{if } \beta_i = \beta_{i-\frac{1}{2}} = 0, \beta_{i+\frac{1}{2}} = 1, \\ \theta_{i-\frac{1}{2}}^2 \mathbf{L}_e^{\text{Lim}} \cdot \text{diag}\left(\bar{\mathbf{h}}_{i-\frac{1}{2}}^{n+1}\right) \cdot \mathbf{R}_u^{\text{Lim}} + \theta_{i+\frac{1}{2}}^2 \mathbf{L}_e^{\text{DG}} \cdot \hat{\mathbf{h}}_{i+\frac{1}{2}}^{n+1} \cdot \mathbf{M}^{-1} \cdot \mathbf{R}_u^{\text{DG}} & \text{if } \beta_i = \beta_{i+\frac{1}{2}} = 0, \beta_{i-\frac{1}{2}} = 1, \end{cases} \quad (59)$$

$$\mathcal{R}_i^{\text{Lim}} = -\frac{\Delta t^2}{\Delta x^2} \theta_{i+\frac{1}{2}}^2 \begin{cases} \mathbf{R}_e^{\text{DG}} \cdot \hat{\mathbf{h}}_{i+\frac{1}{2}}^{n+1} \cdot \mathbf{M}^{-1} \cdot \mathbf{R}_u^{\text{DG}} & \text{if } \beta_{i+1} = \beta_i = 0, \\ \mathbf{R}^{\text{FV}} \cdot \text{diag}\left(\bar{\mathbf{h}}_{i+\frac{1}{2}}^{n+1}\right) \cdot \mathbf{R}^{\text{FV}} & \text{if } \beta_{i+1} = \beta_i = 1, \\ \mathbf{R}_e^{\text{Lim}} \cdot \text{diag}\left(\bar{\mathbf{h}}_{i+\frac{1}{2}}^{n+1}\right) \cdot \mathbf{R}^{\text{FV}} & \text{if } \beta_{i+1} = 1, \beta_i = 0, \\ \mathbf{R}^{\text{FV}} \cdot \text{diag}\left(\bar{\mathbf{h}}_{i+\frac{1}{2}}^{n+1}\right) \cdot \mathbf{R}_u^{\text{Lim}} & \text{if } \beta_{i+1} = 0, \beta_i = 1. \end{cases} \quad (60)$$

Finally, the right hand side term reads

$$\tilde{\mathbf{b}}_i^r = \tilde{\mathbf{b}}_i^{0,r} + \tilde{\mathbf{b}}_i^{x,r} \quad (61)$$

with

$$\tilde{\mathbf{b}}_i^{0,r} = \begin{cases} \mathbf{M} \cdot (\widehat{\rho E}_i^* - \widehat{\rho}_i^{n+1} \widehat{k}_i^{n+1,r}) & \text{if } \beta_i = 0, \\ \widehat{\rho E}_i^* - \widehat{\rho}_i^{n+1} \widehat{k}_i^{n+1,r} & \text{if } \beta_i = 1, \end{cases} \quad (62)$$

and with

$$\tilde{b}_i^{x,r} = -\frac{\Delta t}{\Delta x} \begin{cases} \left(\theta_{i+\frac{1}{2}} \mathbf{R}_{\mathbf{e}}^{\text{DG}} \cdot \hat{\mathbf{h}}_{i+\frac{1}{2}}^{n+1} \hat{\mathbf{G}}_{i+\frac{1}{2}}^n - \theta_{i-\frac{1}{2}} \mathbf{L}_{\mathbf{e}}^{\text{DG}} \cdot \hat{\mathbf{h}}_{i-\frac{1}{2}}^{n+1} \hat{\mathbf{G}}_{i-\frac{1}{2}}^n \right) \\ + \left(\left(1 - \theta_{i+\frac{1}{2}} \right) \mathbf{R}_{\mathbf{e}}^{\text{DG}} \cdot \hat{\mathbf{h}}_{i+\frac{1}{2}}^n \widehat{\boldsymbol{\rho u}}_{i+\frac{1}{2}}^n - \left(1 - \theta_{i-\frac{1}{2}} \right) \mathbf{L}_{\mathbf{e}}^{\text{DG}} \cdot \hat{\mathbf{h}}_{i-\frac{1}{2}}^n \widehat{\boldsymbol{\rho u}}_{i-\frac{1}{2}}^n \right) & \text{if } \beta_i = \beta_{i-\frac{1}{2}} = \beta_{i+\frac{1}{2}} = 0, \\ \left(\theta_{i+\frac{1}{2}} \mathbf{R}_{\mathbf{FV}}^{\text{FV}} \cdot \bar{\mathbf{h}}_{i+\frac{1}{2}}^n \bar{\mathbf{G}}_{i+\frac{1}{2}}^n - \theta_{i-\frac{1}{2}} \mathbf{L}_{\mathbf{FV}}^{\text{FV}} \cdot \bar{\mathbf{h}}_{i-\frac{1}{2}}^n \bar{\mathbf{G}}_{i-\frac{1}{2}}^n \right) \\ + \left(\left(1 - \theta_{i+\frac{1}{2}} \right) \mathbf{R}_{\mathbf{FV}}^{\text{FV}} \cdot \bar{\mathbf{h}}_{i+\frac{1}{2}}^n \bar{\boldsymbol{\rho u}}_{i+\frac{1}{2}}^n - \left(1 - \theta_{i-\frac{1}{2}} \right) \mathbf{L}_{\mathbf{FV}}^{\text{FV}} \cdot \bar{\mathbf{h}}_{i-\frac{1}{2}}^n \bar{\boldsymbol{\rho u}}_{i-\frac{1}{2}}^n \right) & \text{if } \beta_i = \beta_{i-\frac{1}{2}} = \beta_{i+\frac{1}{2}} = 1, \\ \left(\theta_{i+\frac{1}{2}} \mathbf{R}_{\mathbf{e}}^{\text{Lim}} \cdot \bar{\mathbf{h}}_{i+\frac{1}{2}}^{n+1} \bar{\mathbf{G}}_{i+\frac{1}{2}}^n - \theta_{i-\frac{1}{2}} \mathbf{L}_{\mathbf{e}}^{\text{DG}} \cdot \hat{\mathbf{h}}_{i-\frac{1}{2}}^{n+1} \hat{\mathbf{G}}_{i-\frac{1}{2}}^n \right) \\ + \left(\left(1 - \theta_{i+\frac{1}{2}} \right) \mathbf{R}_{\mathbf{e}}^{\text{Lim}} \cdot \bar{\mathbf{h}}_{i+\frac{1}{2}}^{n+1} \bar{\boldsymbol{\rho u}}_{i+\frac{1}{2}}^n - \left(1 - \theta_{i-\frac{1}{2}} \right) \mathbf{L}_{\mathbf{e}}^{\text{DG}} \cdot \hat{\mathbf{h}}_{i-\frac{1}{2}}^n \hat{\boldsymbol{\rho u}}_{i-\frac{1}{2}}^n \right) & \text{if } \beta_i = \beta_{i-\frac{1}{2}} = 0, \beta_{i+\frac{1}{2}} = 1, \\ \left(\theta_{i+\frac{1}{2}} \mathbf{R}_{\mathbf{e}}^{\text{DG}} \cdot \hat{\mathbf{h}}_{i+\frac{1}{2}}^{n+1} \hat{\mathbf{G}}_{i+\frac{1}{2}}^n - \theta_{i-\frac{1}{2}} \mathbf{L}_{\mathbf{e}}^{\text{Lim}} \cdot \bar{\mathbf{h}}_{i-\frac{1}{2}}^{n+1} \bar{\mathbf{G}}_{i-\frac{1}{2}}^n \right) \\ + \left(\left(1 - \theta_{i+\frac{1}{2}} \right) \mathbf{R}_{\mathbf{e}}^{\text{DG}} \cdot \hat{\mathbf{h}}_{i+\frac{1}{2}}^n \hat{\boldsymbol{\rho u}}_{i+\frac{1}{2}}^n - \left(1 - \theta_{i-\frac{1}{2}} \right) \mathbf{L}_{\mathbf{e}}^{\text{Lim}} \cdot \bar{\mathbf{h}}_{i-\frac{1}{2}}^n \bar{\boldsymbol{\rho u}}_{i-\frac{1}{2}}^n \right) & \text{if } \beta_i = \beta_{i+\frac{1}{2}} = 0, \beta_{i-\frac{1}{2}} = 1. \end{cases} \quad (63)$$

We conclude with the algorithms for the interpolation from the main grid to the dual mesh

$$\tilde{\rho}_{i+\frac{1}{2}} = \begin{cases} \mathbf{M}_{\mathbf{L}}^{-1} \cdot (\mathbf{M}_{\mathbf{L}}^{\text{DG}} \cdot \hat{\rho}_i + \mathbf{M}_{\mathbf{R}}^{\text{DG}} \cdot \hat{\rho}_{i+1}) & \text{if } \beta_{i+\frac{1}{2}} = \beta_i = \beta_{i+1} = 0, \\ (\mathbf{M}_{\mathbf{L}}^{\text{FV}} \cdot \bar{\rho}_i + \mathbf{M}_{\mathbf{R}}^{\text{FV}} \cdot \bar{\rho}_{i+1}) & \text{if } \beta_{i+\frac{1}{2}} = \beta_i = \beta_{i+1} = 1, \\ (\mathbf{M}_{\mathbf{L}}^{\text{FV}} \cdot \mathcal{P} \cdot \hat{\rho}_i + \mathbf{M}_{\mathbf{R}}^{\text{FV}} \cdot \bar{\rho}_{i+1}) & \text{if } \beta_{i+\frac{1}{2}} = \beta_{i+1} = 1, \beta_i = 0, \\ (\mathbf{M}_{\mathbf{L}}^{\text{FV}} \cdot \bar{\rho}_i + \mathbf{M}_{\mathbf{R}}^{\text{FV}} \cdot \mathcal{P} \cdot \hat{\rho}_{i+1}) & \text{if } \beta_{i+\frac{1}{2}} = \beta_i = 1, \beta_{i+1} = 0 \end{cases} \quad (64)$$

and with the one for the opposite projection from the staggered grid to the main one

$$\tilde{U}_i = \begin{cases} \mathbf{M}_{\mathbf{L}}^{-1} \cdot (\mathbf{M}_{\mathbf{L}}^{\text{DG}} \cdot \hat{U}_{i-\frac{1}{2}} + \mathbf{M}_{\mathbf{R}}^{\text{DG}} \cdot \hat{U}_{i+\frac{1}{2}}) & \text{if } \beta_i = \beta_{i-\frac{1}{2}} = \beta_{i+\frac{1}{2}} = 0, \\ (\mathbf{M}_{\mathbf{L}}^{\text{FV}} \cdot \bar{U}_{i-\frac{1}{2}} + \mathbf{M}_{\mathbf{R}}^{\text{FV}} \cdot \bar{U}_{i+\frac{1}{2}}) & \text{if } \beta_i = \beta_{i-\frac{1}{2}} = \beta_{i+\frac{1}{2}} = 1, \\ \mathbf{M}_{\mathbf{L}}^{-1} \cdot (\mathbf{M}_{\mathbf{L}}^{\text{DG}} \cdot \hat{U}_{i-\frac{1}{2}} + \mathbf{M}_{\mathbf{R}}^{\text{DG}} \cdot \mathcal{W}_{\mathcal{L}} \cdot \bar{U}_{i+\frac{1}{2}}) & \text{if } \beta_i = \beta_{i-\frac{1}{2}} = 0, \beta_{i+\frac{1}{2}} = 1, \\ \mathbf{M}_{\mathbf{L}}^{-1} \cdot (\mathbf{M}_{\mathbf{L}}^{\text{DG}} \cdot \mathcal{W}_{\mathcal{R}} \cdot \bar{U}_{i-\frac{1}{2}} + \mathbf{M}_{\mathbf{R}}^{\text{DG}} \cdot \hat{U}_{i+\frac{1}{2}}) & \text{if } \beta_i = \beta_{i+\frac{1}{2}} = 0, \beta_{i-\frac{1}{2}} = 1, \end{cases} \quad (65)$$

Finally note that, due to the choice of $N_s = 2P + 1$ subcell averages, the CFL condition for the explicit part of the high order DG scheme and the CFL condition for the explicit part of the subgrid finite volume method yield the same maximum admissible time step size Δt for both semi-implicit schemes.

3 Staggered Semi-implicit DG Schemes with Sub-cell Finite Volume Limiting for the Euler Equations in 2D

In this section we now present the staggered semi-implicit DG scheme with *a posteriori* subcell finite volume limiter for the two-dimensional compressible Euler equations. We start by introducing the unlimited semi-implicit DG scheme in Sect. 3.2.2; then in Sect. 3.3 we briefly focus the attention on the subcell formulation for the semi-implicit FV method in 2D. Later on, we discuss the *a posteriori* subcell limiter for the 2D case, which is again based

on the MOOD paradigm (see Sect. 3.4) and which combines the two methods previously mentioned (see Sect. 3.5).

3.1 Governing Equations of the 2D Model

The two dimensional Euler equations are a nonlinear system of four PDEs and read as follows:

$$\begin{aligned} \frac{\partial \rho}{\partial t} + \frac{\partial \rho u}{\partial x} + \frac{\partial \rho v}{\partial y} &= 0, \\ \frac{\partial \rho u}{\partial t} + \frac{\partial \rho uu}{\partial x} + \frac{\partial \rho uv}{\partial y} + \frac{\partial p}{\partial x} &= 0, \\ \frac{\partial \rho v}{\partial t} + \frac{\partial \rho uv}{\partial x} + \frac{\partial \rho vv}{\partial y} + \frac{\partial p}{\partial y} &= 0, \\ \frac{\partial \rho E}{\partial t} + \frac{\partial}{\partial x} u(\rho E + p) + \frac{\partial}{\partial y} v(\rho E + p) &= 0, \end{aligned} \quad (66)$$

where \mathbf{Q} is the vector of the conserved variables $\mathbf{Q} = [\rho, \rho u, \rho v, \rho E]^T$ and \mathbf{V} is the vector of the primitive variables $\mathbf{V} = [\rho, u, v, p]^T$. The total energy is split into two contributions $\rho E = \rho e + \rho k$, where $k = \frac{1}{2}(u^2 + v^2)$ is the specific kinetic energy. In order to close the system we use again the ideal gas equation of state; hence, similar to the 1D case the internal energy is expressed as $e = \frac{p}{(\gamma - 1)\rho}$. The system of PDEs (66) can be written in conservative and quasi-linear form as

$$\frac{\partial \mathbf{Q}}{\partial t} + \frac{\partial \mathbf{F}_x(\mathbf{Q})}{\partial x} + \frac{\partial \mathbf{F}_y(\mathbf{Q})}{\partial y} = 0 \quad (67)$$

and

$$\frac{\partial \mathbf{Q}}{\partial t} + \mathbf{A}_x(\mathbf{Q}) \frac{\partial \mathbf{Q}}{\partial x} + \mathbf{A}_y(\mathbf{Q}) \frac{\partial \mathbf{Q}}{\partial y} = 0, \quad (68)$$

respectively, where $\mathbf{A}_x(\mathbf{Q})$ and $\mathbf{A}_y(\mathbf{Q})$ are the two Jacobian matrices expressed as $\mathbf{A}_x(\mathbf{Q}) = \partial \mathbf{F}_x(\mathbf{Q}) / \partial \mathbf{Q}$ and $\mathbf{A}_y(\mathbf{Q}) = \partial \mathbf{F}_y(\mathbf{Q}) / \partial \mathbf{Q}$ where $\mathbf{F}_x = [\rho u, \rho u^2 + p, \rho uv, u(E + p)]^T$ and $\mathbf{F}_y = [\rho v, \rho uv, \rho v^2 + p, v(E + p)]^T$ are the physical fluxes in x and y direction, respectively. Also in this case it is possible to verify that Eq. (66) is a hyperbolic system of PDEs, see [82]. In the two dimensional case the flux splitting of Toro and Vázquez yields the following PDE for the total energy equation.

$$\frac{\partial}{\partial t} (\rho e + \rho k) + \frac{\partial}{\partial x} (\rho k u + h \rho u) + \frac{\partial}{\partial y} (\rho k v + h \rho v) = 0. \quad (69)$$

3.2 Unlimited Staggered Semi-implicit DG Scheme for the 2D Euler Equations

First we introduce the main grid for the computational domain $\Omega_{xy} = [x_L, x_R] \times [y_B, y_T]$ which is divided into $N_x \times N_y$ control volumes denoted as $T_{i,j} = [x_{i-\frac{1}{2}}, x_{i+\frac{1}{2}}] \times [y_{j-\frac{1}{2}}, y_{j+\frac{1}{2}}]$, see Fig. 7a. In addition, the lengths of the elements $T_{i,j}$ are $\Delta x = \frac{x_R - x_L}{N_x}$ and $\Delta y = \frac{y_T - y_B}{N_y}$ for the x and y directions, respectively. Later on we consider two staggered grids and their cells are denoted by $T_{i+\frac{1}{2},j} = [x_i, x_{i+1}] \times [y_{j-\frac{1}{2}}, y_{j+\frac{1}{2}}]$ and $T_{i,j+\frac{1}{2}} = [x_{i-\frac{1}{2}}, x_{i+\frac{1}{2}}] \times [y_j, y_{j+1}]$, see Fig. 7b. Now we consider the same polynomial basis functions ϕ and ψ of degree P used in the 1D semi-implicit DG scheme. Hence, a quantity defined on the main grid, for example the pressure, is represented within element

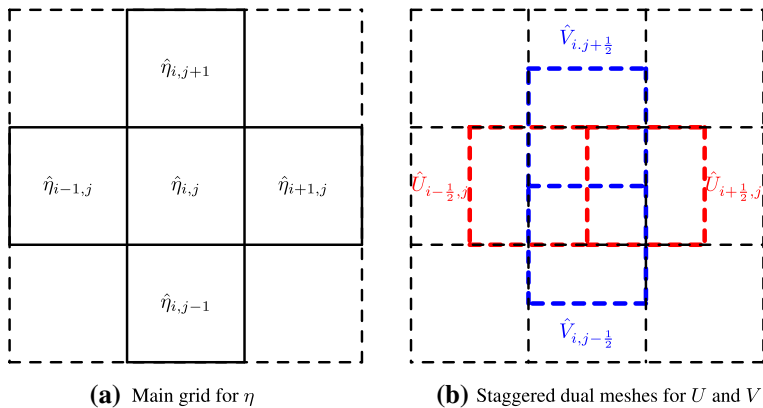


Fig. 7 Computational grids for the 2D semi-implicit staggered DG scheme

the $T_{i,j}$ as follows

$$p_{i,j}(x, y, t) = \sum_l^{P+1} \sum_m^{P+1} \phi_l(x)\phi_m(y) \hat{p}_{i,j,l,m}(t) = \boldsymbol{\phi}(x)\boldsymbol{\phi}(y) \cdot \hat{\mathbf{p}}_{i,j}(t), \quad (70)$$

then, according to the philosophy of staggered methods the velocities are located on the dual meshes and they are defined as

$$u_{i+\frac{1}{2},j}(x,y,t) = \sum_l^P \sum_m^{P+1} \phi_l(x)\psi_m(y)\hat{u}_{i+\frac{1}{2},j,l,m}(t) = \boldsymbol{\phi}(x)\boldsymbol{\psi}(y) \cdot \hat{\mathbf{u}}_{i+\frac{1}{2},j}(t) \quad (71)$$

$$v_{i,j+\frac{1}{2}}(x, y, t) = \sum_l^{P+1} \sum_m^{P+1} \psi_l(x) \phi_m(y) \hat{v}_{i,j+\frac{1}{2},l,m}(t) = \boldsymbol{\psi}(x) \boldsymbol{\phi}(y) \cdot \hat{\mathbf{v}}_{i,j+\frac{1}{2}}(t). \quad (72)$$

3.2.1 Convective Terms

Similar to the 1D staggered semi-implicit DG method, also in the 2D case the nonlinear convective terms are updated on the main grid and integrated using the RKDG method where the spatial operator $\mathbf{L}_h(\tilde{\mathbf{Q}})$ reads

$$\mathbf{L}_h(\widehat{\mathbf{Q}})|_{T_i} = \mathbf{L}_h^x(\widehat{\mathbf{Q}})|_{T_i} + \mathbf{L}_h^y(\widehat{\mathbf{Q}})|_{T_i} \quad (73)$$

with

$$\mathbf{L}_h^x(\widehat{\mathbf{Q}})|_{T_i} = -\frac{\Delta t}{\Delta x \Delta y} (\mathbf{M}^{\mathbf{x}\mathbf{y}})^{-1} \left(\int_{\partial T_{i,j}} \boldsymbol{\phi} \mathbf{F}_{\mathbf{x}}^{\mathbf{c}} \cdot \mathbf{n} dS - \int_{T_{i,j}} \nabla \boldsymbol{\phi} \cdot \mathbf{F}_{\mathbf{x}}^{\mathbf{c}} dx dy \right), \quad (74)$$

$$\mathbf{L}_h^y(\widehat{\mathbf{Q}})|_{T_i} = -\frac{\Delta t}{\Delta x \Delta y} (\mathbf{M}^{\mathbf{xy}})^{-1} \left(\int_{\partial T_{i,j}} \boldsymbol{\phi} \mathbf{F}_y^c \cdot \mathbf{n} dS - \int_{T_{i,j}} \nabla \boldsymbol{\phi} \cdot \mathbf{F}_y^c dx dy \right), \quad (75)$$

where $\mathbf{F}_x^c = [\rho u, \rho uu, \rho uv, \rho ku]^T$ and $\mathbf{F}_y^c = [\rho v, \rho uv, \rho vv, \rho kv]^T$ are the physical convective fluxes and for the computation of the mass matrix \mathbf{M}^{xy} we will give more explanations

in the next subsection. In addition, the numerical fluxes are computed using the Rusanov method

$$\mathbf{F} \cdot \mathbf{n} = \frac{1}{2} (\mathbf{F}^c(q^+) + \mathbf{F}^c(q^-)) \cdot \mathbf{n} - \frac{1}{2} S_{max} (\mathbf{q}^+ - \mathbf{q}^-), \quad \text{with } S_{max} = \max(|\mathbf{v}^+ \cdot \mathbf{n}|, |\mathbf{v}^- \cdot \mathbf{n}|). \quad (76)$$

3.2.2 Derivation of the 2D Semi-implicit Staggered DG Scheme

The integration of the energy equation is carried out by multiplying Eq. (69) with the test functions $\phi\psi$ and integrating over a control volume $T_{i,j}$ of the main grid

$$\int_{x_{i-\frac{1}{2},j}}^{x_{i+\frac{1}{2},j}} \int_{y_{i,j-\frac{1}{2}}}^{y_{i,j+\frac{1}{2}}} \phi\psi \left(\frac{\partial}{\partial t}(\rho e + \rho k) + \frac{\partial}{\partial x}(\rho ku + h\rho u) + \frac{\partial}{\partial y}(\rho kv + h\rho v) \right) dx dy = 0. \quad (77)$$

Similarly, the momentum equations in x and y direction are discretized on the dual meshes as follows

$$\int_{x_{i,j}}^{x_{i+1,j}} \int_{y_{i,j-\frac{1}{2}}}^{y_{i,j+\frac{1}{2}}} \psi\phi \left(\frac{\partial \rho u}{\partial t} + \frac{\partial \rho u^2}{\partial x} + \frac{\partial \rho uv}{\partial y} \right) dx dy = - \int_{x_{i,j}}^{x_{i+1,j}} \int_{y_{i,j-\frac{1}{2}}}^{y_{i,j+\frac{1}{2}}} \psi\phi \frac{\partial p}{\partial x} dx dy. \quad (78)$$

$$\int_{x_{i-\frac{1}{2},j}}^{x_{i+\frac{1}{2},j}} \int_{y_{i,j}}^{y_{i,j+1}} \phi\psi \left(\frac{\partial \rho v}{\partial t} + \frac{\partial \rho uv}{\partial x} + \frac{\partial \rho v^2}{\partial y} \right) dx dy = - \int_{x_{i-\frac{1}{2},j}}^{x_{i+\frac{1}{2},j}} \int_{y_{i,j}}^{y_{i,j+1}} \phi\psi \frac{\partial p}{\partial y} dx dy. \quad (79)$$

We proceed with Eq. (77) by splitting the integration of the time derivative in three contributions

$$\left(\int_{x_{i-\frac{1}{2}}}^{x_{i+\frac{1}{2}}} \phi\phi dx \right) \cdot \left(\int_{y_{j-\frac{1}{2}}}^{y_{j+\frac{1}{2}}} \phi\phi dy \right) \cdot \left(\frac{\widehat{\rho E}_{i,j}^{n+1} + \widehat{\rho k}_{i,j}^{n+1} - \widehat{\rho E}_{i,j}^*}{\Delta t} \right) \quad (80)$$

where $\widehat{\rho E}_{i,j}^{n+1} = \widehat{\rho e}_{i,j}^{n+1} + \widehat{\rho k}_{i,j}^{n+1}$ is the total energy density at the new time and the termntsiz $\widehat{\rho E}_{i,j}^*$ is the result of the explicit discretization of the convection of the kinetic energy. Now we consider the integration of the derivative in x direction $\frac{\partial h\rho u}{\partial x}$. In this case it is possible to isolate the integral of the basis functions that depends on y while for the remaining part the procedure is carried out similarly to Eq. (18); hence integration by parts and the adaptive θ -method in order to get second order of accuracy in time yield

$$\left(+ \phi\left(x_{i+\frac{1}{2}}^-\right) \psi\left(x_{i+\frac{1}{2}}\right) \psi\left(x_{i+\frac{1}{2}}\right) \cdot \hat{h}_{i+\frac{1}{2},j}^{n+\theta_{i+\frac{1}{2},j}} \widehat{\rho u}_{i+\frac{1}{2},j}^{n+\theta_{i+\frac{1}{2},j}} - \phi\left(x_{i-\frac{1}{2}}^+\right) \psi\left(x_{i-\frac{1}{2}}\right) \psi\left(x_{i-\frac{1}{2}}\right) \cdot \hat{h}_{i-\frac{1}{2},j}^{n+\theta_{i-\frac{1}{2},j}} \widehat{\rho u}_{i-\frac{1}{2},j}^{n+\theta_{i-\frac{1}{2},j}} \right. \\ \left. - \left(\int_{x_i^-}^{x_i^+} \frac{\partial \phi}{\partial x} \psi \psi dx \right) \cdot \hat{h}_{i-\frac{1}{2},j}^{n+\theta_{i-\frac{1}{2},j}} \widehat{\rho u}_{i-\frac{1}{2},j}^{n+\theta_{i-\frac{1}{2},j}} - \left(\int_{x_i^-}^{x_i^+} \frac{\partial \phi}{\partial x} \psi \psi dx \right) \cdot \hat{h}_{i+\frac{1}{2},j}^{n+\theta_{i+\frac{1}{2},j}} \widehat{\rho u}_{i+\frac{1}{2},j}^{n+\theta_{i+\frac{1}{2},j}} \right) \left(\int_{y_{j-\frac{1}{2}}}^{y_{j+\frac{1}{2}}} \phi \phi dy \right). \quad (81)$$

The integration of the derivative $\frac{\partial h \rho v}{\partial y}$ can be done in the same way. Later on, we continue the integration of Eq. (78). The time derivative is discretized introducing the nonlinear convective term $\widehat{\rho u}_{i+\frac{1}{2},j}^*$ and separating the integrals in x and y direction. Then, the contribution of the pressure gradient is approximated by splitting it into a smooth contribution and a jump term across the interface of the primary grid, which is located in the interior of the dual mesh. Furthermore, we use a spatially adaptive θ -method. The same procedure can be properly repeated for Eq. (79).

$$\left(\int_{x_i}^{x_{i+1}} \psi \psi dx \right) \left(\int_{y_{i-\frac{1}{2}}}^{y_{i+\frac{1}{2}}} \phi \phi dy \right) \cdot \left(\frac{\widehat{\rho u}_{i+\frac{1}{2},j}^{n+1} - \widehat{\rho u}_{i+\frac{1}{2},j}^*}{\Delta t} \right) = - \left(\int_{y_{i-\frac{1}{2}}}^{y_{i+\frac{1}{2}}} \phi \phi dy \right) \\ \cdot \left(\psi\left(x_{i+\frac{1}{2}}\right) \left(\phi\left(x_{i+\frac{1}{2}}^+\right) \cdot \hat{p}_{i+1,j}^{n+\theta_{i+\frac{1}{2},j}} - \phi\left(x_{i+\frac{1}{2}}^-\right) \cdot \hat{p}_{i,j}^{n+\theta_{i-\frac{1}{2},j}} \right) \right. \\ \left. - \left(\int_{x_i}^{x_{i+\frac{1}{2}}} \psi \frac{\partial \phi}{\partial x} dx \right) \cdot \hat{p}_{i,j}^{n+\theta_{i-\frac{1}{2},j}} - \left(\int_{x_{i+\frac{1}{2}}}^{x_{i+1}} \psi \frac{\partial \phi}{\partial x} dx \right) \cdot \hat{p}_{i+1,j}^{n+\theta_{i+\frac{1}{2},j}} \right) \quad (82)$$

Finally, the integration of Eqs. (77), (78) and (79) is completed and written in the compact matrix-vector notation as follows

$$\mathbf{M}^{\mathbf{xy}} \cdot (\widehat{\rho e}_{i,j}^{n+1} + \widehat{\rho k}_{i,j}^{n+1} - \widehat{\rho E}_{i,j}^*) \\ + \frac{\Delta t}{\Delta x} \mathbf{M}^{\mathbf{y}} \cdot \left(\mathbf{R}_e^{\mathbf{x}, \text{DG}} \cdot \hat{h}_{i+\frac{1}{2},j}^{n+\theta_{i+\frac{1}{2},j}} \widehat{\rho u}_{i+\frac{1}{2},j}^{n+\theta_{i+\frac{1}{2},j}} - \mathbf{L}_e^{\mathbf{x}, \text{DG}} \cdot \hat{h}_{i-\frac{1}{2},j}^{n+\theta_{i-\frac{1}{2},j}} \widehat{\rho u}_{i-\frac{1}{2},j}^{n+\theta_{i-\frac{1}{2},j}} \right) \\ + \frac{\Delta t}{\Delta y} \mathbf{M}^{\mathbf{x}} \cdot \left(\mathbf{R}_e^{\mathbf{y}, \text{DG}} \cdot \hat{h}_{i,j+\frac{1}{2}}^{n+\theta_{i,j+\frac{1}{2}}} \widehat{\rho v}_{i,j+\frac{1}{2}}^{n+\theta_{i,j+\frac{1}{2}}} - \mathbf{L}_e^{\mathbf{y}, \text{DG}} \cdot \hat{h}_{i,j-\frac{1}{2}}^{n+\theta_{i,j-\frac{1}{2}}} \widehat{\rho v}_{i,j-\frac{1}{2}}^{n+\theta_{i,j-\frac{1}{2}}} \right) = 0 \quad (83)$$

$$\mathbf{M}^{\mathbf{xy}} \cdot \left(\widehat{\rho u}_{i+\frac{1}{2},j}^{n+1} - \widehat{\rho u}_{i+\frac{1}{2},j}^* \right) + \frac{\Delta t}{\Delta x} \mathbf{M}^{\mathbf{y}} \cdot \left(\mathbf{R}_p^{\mathbf{x}, \text{DG}} \cdot \hat{p}_{i+1,j}^{n+\theta_{i+\frac{1}{2},j}} - \mathbf{L}_p^{\mathbf{x}, \text{DG}} \cdot \hat{p}_{i,j}^{n+\theta_{i+\frac{1}{2},j}} \right) = 0 \quad (84)$$

$$\mathbf{M}^{\mathbf{xy}} \cdot \left(\widehat{\rho v}_{i,j+\frac{1}{2}}^{n+1} - \widehat{\rho v}_{i,j+\frac{1}{2}}^* \right) + \frac{\Delta t}{\Delta y} \mathbf{M}^{\mathbf{x}} \cdot \left(\mathbf{R}_p^{\mathbf{y}, \text{DG}} \cdot \hat{p}_{i,j+1}^{n+\theta_{i,j+\frac{1}{2}}} - \mathbf{L}_p^{\mathbf{y}, \text{DG}} \cdot \hat{p}_{i,j}^{n+\theta_{i,j+\frac{1}{2}}} \right) = 0 \quad (85)$$

The matrices used in Eqs. (83), (84), (85), (74), (75) are obtained using the following tensor products and assuming the Einstein convection of summation over repeated indexes

$$\mathbf{Z}^{\mathbf{x}} = Z_{mn} I_{m'n'} X_{nn'}, \quad \mathbf{Z}^{\mathbf{y}} = I_{mn} Z_{m'n'} X_{nn'}, \quad \mathbf{Z}^{\mathbf{xy}} = \mathbf{Z}^{\mathbf{x}} \cdot \mathbf{Z}^{\mathbf{y}}, \quad (86)$$

where $\widehat{\mathbf{X}}$ is a generic vector of degrees of freedom, \mathbf{Z} is a square matrix and \mathbf{I} is the identity matrix. Consequently, these tensor products are carried out involving the same tensors introduced in the 1D case for the unlimited semi-implicit staggered DG scheme. See also [44] for a similar notation employed in the context of high order semi-implicit staggered DG methods for the incompressible Navier–Stokes equations.

Then, from Eqs. (84) and (85) one can get an expression of the degrees of freedom of $\widehat{\rho\mathbf{u}}_{i,j \pm \frac{1}{2}}^{n+1}$ and $\widehat{\rho\mathbf{v}}_{i,j \pm \frac{1}{2}}^{n+1}$ and cast them into Eq. (83). Later on, similar to the 1D case, an iterative *Picard* procedure is introduced in order to avoid the solution of a strongly nonlinear system of equations. Consequently, the final *linear* system for the unknown pressure reads

$$\mathcal{L}_{i,j}^{x,\text{DG}} \cdot \hat{p}_{i-1,j}^{n+1,r+1} + \mathcal{L}_{i,j}^{y,\text{DG}} \cdot \hat{p}_{i,j-1}^{n+1,r+1} + \mathcal{C}_{i,j}^{\text{DG}} \cdot \hat{p}_{i,j}^{n+1,r+1} + \mathcal{R}_{i,j}^{x,\text{DG}} \cdot \hat{p}_{i+1,j}^{n+1,r+1} + \mathcal{R}_{i,j}^{y,\text{DG}} \cdot \hat{p}_{i,j+1}^{n+1,r+1} = \hat{b}_{i,j}^r, \quad (87)$$

and is solved using modern iterative Krylov subspace methods based on a matrix-free implementation. Numerical experiments have shown that system in Eq. (87) can be solved using the conjugate gradient method, but we stress that we do not have a rigorous proof yet that the system is symmetric and positive definite. A deeper analysis will be carried out in further works.

We stress again that, for the ideal gas EOS, in our approach the resulting pressure system is always *linear*. The pressure system would become nonlinear only for those real gas EOS, where the internal energy density ρe is a nonlinear function of the pressure p , see [36].

Once the pressure is known, in the Picard loop the degrees of freedom of the momentum in x and y direction are readily updated as follows

$$\widehat{\rho\mathbf{u}}_{i+\frac{1}{2},j}^{n+1} = \widehat{\mathbf{G}\mathbf{u}}_{i+\frac{1}{2},j}^{n+1} - \theta_{i+\frac{1}{2},j} \frac{\Delta t}{\Delta x} (\mathbf{M}^{x-1}) \cdot \left(\mathbf{R}_p^{x,\text{DG}} \cdot \hat{p}_{i+1,j}^{n+1,r+1} - \mathbf{L}_p^{x,\text{DG}} \cdot \hat{p}_{i,j}^{n+1,r+1} \right) \quad (88)$$

$$\widehat{\rho\mathbf{v}}_{i,j+\frac{1}{2}}^{n+1} = \widehat{\mathbf{G}\mathbf{v}}_{i,j+\frac{1}{2}}^{n+1} - \theta_{i,j+\frac{1}{2}} \frac{\Delta t}{\Delta y} (\mathbf{M}^{y-1}) \cdot \left(\mathbf{R}_p^{y,\text{DG}} \cdot \hat{p}_{i,j+1}^{n+1,r+1} - \mathbf{L}_p^{y,\text{DG}} \cdot \hat{p}_{i,j}^{n+1,r+1} \right) \quad (89)$$

and the two components of the velocity vector are computed component-wise as

$$\widehat{\mathbf{u}}_{i+\frac{1}{2},j}^{n+1} = \frac{\widehat{\rho\mathbf{u}}_{i+\frac{1}{2},j}^{n+1}}{\widehat{\rho}_{i+\frac{1}{2},j}^{n+1}}, \quad \widehat{\mathbf{v}}_{i,j+\frac{1}{2}}^{n+1} = \frac{\widehat{\rho\mathbf{v}}_{i,j+\frac{1}{2}}^{n+1}}{\widehat{\rho}_{i,j+\frac{1}{2}}^{n+1}}. \quad (90)$$

In the previous equation the density is extrapolated on the staggered meshes using the following L_2 -based projection

$$\hat{\rho}_{i+\frac{1}{2},j} = (\mathbf{M}^x)^{-1} \cdot (\mathbf{M}_L^{x,\text{DG}} \cdot \hat{\rho}_{i,j} + \mathbf{M}_R^{x,\text{DG}} \cdot \hat{\rho}_{i+1,j}) \quad (91)$$

$$\hat{\rho}_{i,j+\frac{1}{2}} = (\mathbf{M}^y)^{-1} \cdot (\mathbf{M}_L^{y,\text{DG}} \cdot \hat{\rho}_{i,j} + \mathbf{M}_R^{y,\text{DG}} \cdot \hat{\rho}_{i,j+1}). \quad (92)$$

Similarly, we interpolate the velocities on the main grid from the dual control volumes

$$\hat{u}_{i,j} = (\mathbf{M}^x)^{-1} \cdot (\mathbf{M}_L^{x,\text{DG}} \cdot \hat{u}_{i-\frac{1}{2},j} + \mathbf{M}_R^{x,\text{DG}} \cdot \hat{u}_{i+\frac{1}{2},j}) \quad (93)$$

$$\hat{v}_{i,j} = (\mathbf{M}^y)^{-1} \cdot (\mathbf{M}_L^{y,\text{DG}} \cdot \hat{v}_{i,j-\frac{1}{2}} + \mathbf{M}_R^{y,\text{DG}} \cdot \hat{v}_{i,j+\frac{1}{2}}) \quad (94)$$

and then it is possible to compute the kinetic energy as

$$\hat{k}_{i,j} = \frac{1}{2}(\hat{u}_{i,j}^2 + \hat{v}_{i,j}^2). \quad (95)$$

Finally, once the Picard loop is terminated, it is possible to update the degrees of freedom of the total energy density by the following expression

$$\begin{aligned} \widehat{\rho E}_{i,j}^{n+1} &= \widehat{\rho E}_{i,j}^* \\ &- \frac{\Delta t}{\Delta x} \mathbf{M}^{\mathbf{x}-1} \cdot \left(\mathbf{R}_e^{\mathbf{x}, \text{DG}} \cdot \hat{h}_{i+\frac{1}{2},j}^{n+\theta_{i+\frac{1}{2},j}} \widehat{\rho u}_{i+\frac{1}{2},j}^{n+\theta_{i+\frac{1}{2},j}} - \mathbf{L}_e^{\mathbf{x}, \text{DG}} \cdot \hat{h}_{i-\frac{1}{2},j}^{n+\theta_{i-\frac{1}{2},j}} \widehat{\rho u}_{i-\frac{1}{2},j}^{n+\theta_{i-\frac{1}{2},j}} \right) \\ &- \frac{\Delta t}{\Delta y} \mathbf{M}^{\mathbf{y}-1} \cdot \left(\mathbf{R}_e^{\mathbf{y}, \text{DG}} \cdot \hat{h}_{i,j+\frac{1}{2}}^{n+\theta_{i,j+\frac{1}{2}}} \widehat{\rho v}_{i,j+\frac{1}{2}}^{n+\theta_{i,j+\frac{1}{2}}} - \mathbf{L}_e^{\mathbf{y}, \text{DG}} \cdot \hat{h}_{i,j-\frac{1}{2}}^{n+\theta_{i,j-\frac{1}{2}}} \widehat{\rho v}_{i,j-\frac{1}{2}}^{n+\theta_{i,j-\frac{1}{2}}} \right), \end{aligned} \quad (96)$$

which is easily obtained modifying properly Eq. (83). We conclude discussing the stability condition of the method. The maximum time step is given by the classical CFL condition of the DG method based on the maximum velocities $|u_{\max}|$ and $|v_{\max}|$

$$\Delta t = \text{CFL} \left(\frac{|u_{\max}|}{\Delta x} + \frac{|v_{\max}|}{\Delta y} \right)^{-1}, \quad \text{with} \quad \text{CFL} < \frac{1}{2P+1}. \quad (97)$$

This is possible due to the implicit treatment of the pressure system and, as we will see later, this makes the staggered semi-implicit 2D DG scheme a good candidate for solving the 2D Euler equations in the low Mach number regime.

3.3 A Sub-cell Formulation for the Semi-implicit Finite Volume Method for the 2D Euler Equations

Now the two dimensional case of the semi-implicit sub-cell finite volume scheme is presented. This method represents the two dimensional extension of the method proposed in Sect. 2.3. Similarly to the previous sub-section the control volumes of the the grids are $T_{i,j}$, $T_{i+\frac{1}{2},j}$ and $T_{i,j+\frac{1}{2}}$ see Figs. 8 and 9. The sub-grid is composed of $(2P+1)^2$ finite volume sub-elements of size $\Delta x_s = \Delta x/(2P+1)$ and $\Delta y_s = \Delta y/(2P+1)$, where P is a positive integer, see Fig. 8b.

Here the quantities assigned to the main grid and to the the dual meshes are chosen in the same way discussed in the previous Sect. 3.2.2. Then, the explicit convective terms are updated at the subcell level using a first order finite volume scheme on collocated grids with a simple Rusanov-type method for the numerical fluxes

$$\overline{\mathcal{Q}}_{i,j,p,q}^* = \overline{\mathcal{Q}}_{i,j,p,q}^n - \frac{\Delta t}{\Delta x_s} \left(\mathbf{F}_{i,j,p+\frac{1}{2},q}^c - \mathbf{F}_{i,j,p-\frac{1}{2},q}^c \right) - \frac{\Delta t}{\Delta y_s} \left(\mathbf{G}_{i,j,p,q+\frac{1}{2}}^c - \mathbf{G}_{i,j,p,q-\frac{1}{2}}^c \right). \quad (98)$$

Later on, the semi-implicit discretization of the energy equation is carried out on the main grid and it reads

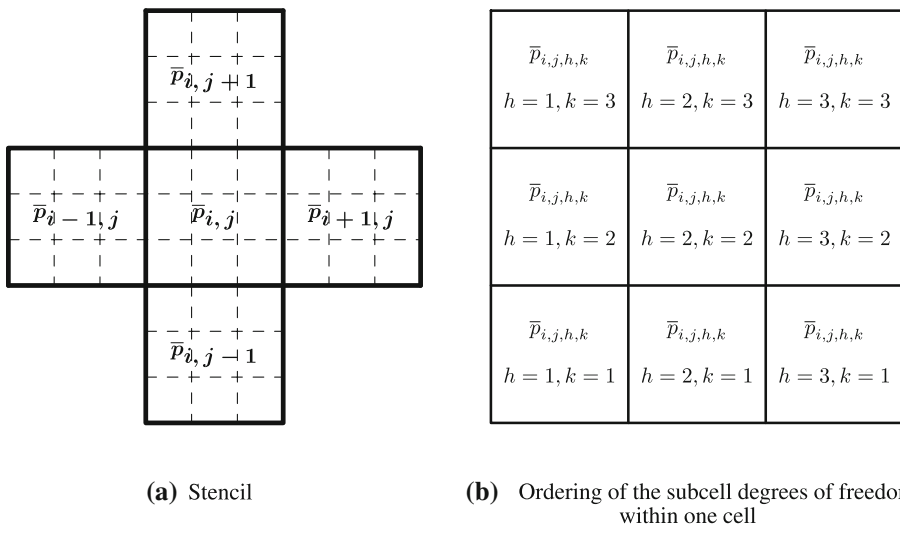


Fig. 8 Main grid and sub-cells for the 2D semi-implicit sub-cell finite volume scheme

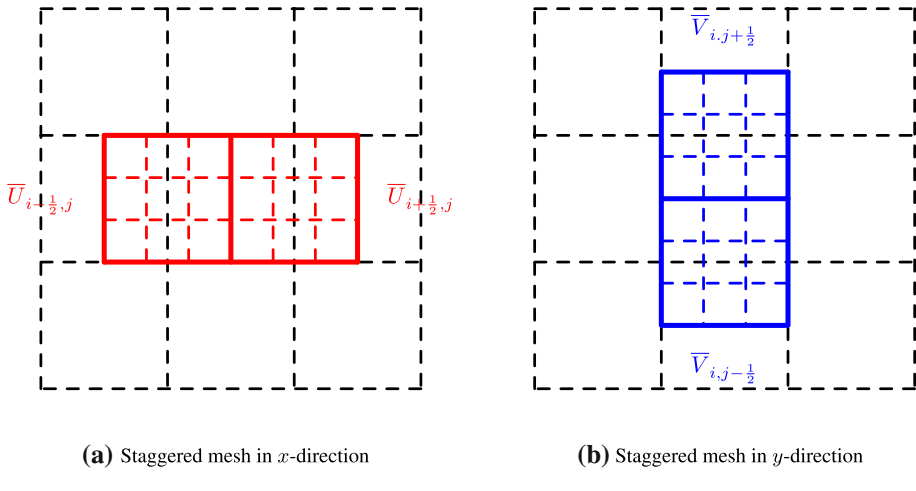


Fig. 9 Staggered grids for the 2D semi-implicit sub-cell finite volume scheme

$$\begin{aligned}
 & (\overline{\rho e}_{i,j}^{n+1} + \overline{\rho k}_{\sim i,j}^{n+1} - \overline{\rho E}_{i,j}^*) \\
 & + \frac{\Delta t}{\Delta x} \left(\mathbf{R}^x, \text{FV} \cdot \overline{h \rho u}_{i+\frac{1}{2},j}^{n+\theta_{i+\frac{1}{2},j}} - \mathbf{L}^x, \text{FV} \cdot \overline{h \rho u}_{i-\frac{1}{2},j}^{n+\theta_{i-\frac{1}{2},j}} \right) \\
 & + \frac{\Delta t}{\Delta y} \left(\mathbf{R}^y, \text{FV} \cdot \overline{h \rho v}_{i,j+\frac{1}{2}}^{n+\theta_{i,j+\frac{1}{2}}} - \mathbf{L}^y, \text{FV} \cdot \overline{h \rho v}_{i,j-\frac{1}{2}}^{n+\theta_{i,j-\frac{1}{2}}} \right) = 0. \quad (99)
 \end{aligned}$$

while the momentum equations are approximated on the control volumes of the dual grids as follows

$$\left(\overline{\rho u}_{i+\frac{1}{2},j}^{n+1} - \overline{\rho u}_{i+\frac{1}{2},j}^* \right) + \frac{\Delta t}{\Delta x} \left(\mathbf{R}^x, \text{FV} \cdot \overline{p}_{i+1,j}^{n+\theta_{i+\frac{1}{2},j}} - \mathbf{L}^x, \text{FV} \cdot \overline{p}_{i,j}^{n+\theta_{i+\frac{1}{2},j}} \right) = 0 \quad (100)$$

$$\left(\bar{\rho} \bar{v}_{i,j+\frac{1}{2}}^{n+1} - \bar{\rho} \bar{v}_{i,j+\frac{1}{2}}^* \right) + \frac{\Delta t}{\Delta y} \left(\mathbf{R}^y, \text{FV} \cdot \bar{p}_{i,j+1}^{n+\theta_{i,j+\frac{1}{2}}} - \mathbf{L}^y, \text{FV} \cdot \bar{p}_{i,j}^{n+\theta_{i,j+\frac{1}{2}}} \right) = 0 \quad (101)$$

The tensor products in Eqs. (99), (100), (101) are carried out using the same approach explained in the previous subsection. So matrix multiplications involve only the tensors introduced for the 1D case of the subcell finite volume method and they are reported in “Appendix A.2”.

Then, at every iteration of the Picard loop we solve the following linear system

$$\mathcal{L}_{i,j}^{x,\text{FV}} \cdot \bar{p}_{i-1,j}^{n+1,r+1} + \mathcal{L}_{i,j}^{y,\text{FV}} \cdot \bar{p}_{i,j-1}^{n+1,r+1} + \mathcal{C}_{i,j}^{\text{FV}} \cdot \bar{p}_{i,j}^{n+1,r+1} + \mathcal{R}_{i,j}^{x,\text{FV}} \cdot \bar{p}_{i+1,j}^{n+1,r+1} + \mathcal{R}_{i,j}^{y,\text{FV}} \cdot \bar{p}_{i,j+1}^{n+1,r+1} = \bar{b}_{i,j}^r, \quad (102)$$

which is obtained coupling the energy equation (99) with the momentum equations (100) and (101). System in Eq. (102) is symmetric and positive definite since that the method presented in this subsection is an extension at the subgrid level of the FV method proposed [36]. Hence a conjugate gradient method gives efficiently the pressure $\bar{p}^{n+1,r+1}$ and then the momentum is readily updated using Eqs. (100) and 101. Then, one can compute the kinetic energy where the velocities are extrapolated from the dual grid using the following projections

$$\bar{u}_{i,j} = \left(\mathbf{M}_L^{x,\text{FV}} \cdot \bar{u}_{i-\frac{1}{2},j} + \mathbf{M}_R^{y,\text{FV}} \cdot \bar{u}_{i+\frac{1}{2},j} \right) \quad (103)$$

$$\bar{v}_{i,j} = \left(\mathbf{M}_L^{y,\text{FV}} \cdot \bar{v}_{i,j-\frac{1}{2}} + \mathbf{M}_R^{x,\text{FV}} \cdot \bar{v}_{i,j+\frac{1}{2}} \right). \quad (104)$$

where $\bar{u}_{i+\frac{1}{2},j} = \bar{\rho} \bar{u}_{i+\frac{1}{2},j} / \bar{\rho}_{i+\frac{1}{2},j}$ and $\bar{v}_{i,j+\frac{1}{2}} = \bar{\rho} \bar{v}_{i,j+\frac{1}{2}} / \bar{\rho}_{i,j+\frac{1}{2}}$ are computed component-wise, respectively. Similarly, the densities on the dual grids $\bar{\rho}_{i+\frac{1}{2},j}$ and $\bar{\rho}_{i,j+\frac{1}{2}}$ are computed from $\bar{p}_{i,j}$ using these subcell finite volume averages

$$\bar{\rho}_{i+\frac{1}{2},j} = \left(\mathbf{M}_L^{x,\text{FV}} \cdot \bar{\rho}_{i,j} + \mathbf{M}_R^{x,\text{FV}} \cdot \bar{\rho}_{i+1,j} \right) \quad (105)$$

$$\bar{\rho}_{i,j+\frac{1}{2}} = \left(\mathbf{M}_L^{y,\text{FV}} \cdot \bar{\rho}_{i,j} + \mathbf{M}_R^{y,\text{FV}} \cdot \bar{\rho}_{i,j+1} \right). \quad (106)$$

Finally, the update for the total energy reads

$$\begin{aligned} \bar{\rho} \bar{E}_{i,j}^{n+1} - \bar{\rho} \bar{E}_{i,j}^* &= -\frac{\Delta t}{\Delta x} \left(\mathbf{R}^x, \text{FV} \cdot \bar{h} \bar{\rho} \bar{u}_{i+\frac{1}{2},j}^{n+\theta_{i+\frac{1}{2},j}} - \mathbf{L}^x, \text{FV} \cdot \bar{h} \bar{\rho} \bar{u}_{i-\frac{1}{2},j}^{n+\theta_{i-\frac{1}{2},j}} \right) \\ &\quad - \frac{\Delta t}{\Delta y} \left(\mathbf{R}^y, \text{FV} \cdot \bar{h} \bar{\rho} \bar{v}_{i,j+\frac{1}{2}}^{n+\theta_{i,j+\frac{1}{2}}} - \mathbf{L}^y, \text{FV} \cdot \bar{h} \bar{\rho} \bar{v}_{i,j-\frac{1}{2}}^{n+\theta_{i,j-\frac{1}{2}}} \right) \end{aligned} \quad (107)$$

In this method, Δt is computed according to the following expression for the CFL condition

$$\Delta t = \text{CFL} \left(\frac{|u_{\max}|}{\Delta x_s} + \frac{|v_{\max}|}{\Delta y_s} \right)^{-1}, \quad \text{with } \text{CFL} < 1. \quad (108)$$

3.4 MOOD Algorithm and Detection Criteria: 2D Case

The MOOD algorithm for the two-dimensional case is based on the same approach of Sect. 2.4. Consequently, the two dimensional extension of the considerations made in Sect. 2.4 is straightforward. We introduce the projection and reconstruction matrices \mathcal{P}^{xy} and \mathcal{W}^{xy} for a generic variable q . Hence, we have $\bar{q}_{i,j}^n = \mathcal{P}^{xy} \cdot \hat{q}_{i,j}^n$, $\hat{q}_{i,j}^n = \mathcal{W}^{xy} \cdot \bar{q}_{i,j}^n$.

In addition, we introduce also the operators $\mathbb{W}^x, \mathbb{W}^y, \mathbb{P}^x, \mathbb{P}^y$ and, for the sake of simplicity, their role will be explained in the next subsection. The detection criteria are based on the

positivity of the density and of the pressure and on the relaxed discrete maximum principle (DMP), i.e.

$$\hat{p}_{i,j,m}^{\circ,n+1} > 0, \quad \hat{p}_{i,j,l,k}^{\circ,n+1} > 0, \quad \text{and} \quad \min_{\forall T_{k,l} \in \mathcal{V}_{i,j}} (\hat{q}_{k,l,m}^n) - \delta \leq \hat{q}_{i,j,m}^{\circ,n+1} \leq \max_{\forall T_{k,l} \in \mathcal{V}_{i,j}} (\hat{q}_{k,l,m}^n) + \delta, \quad (109)$$

where $\mathcal{V}_{i,j} = \{T_{i-1,j-1}, T_{i,j-1}, T_{i+1,j-1}, T_{i-1,j}, T_{i,j}, T_{i+1,j}, T_{i-1,j+1}, T_{i,j+1}, T_{i+1,j+1}\}$ is the set of Voronoi neighbours of $T_{i,j}$ and δ is the same relaxation parameter for the DMP as in the 1D case. The DMP is applied to the set of conserved variables $\rho, \rho u, \rho v, \rho E$ as well to the primitive variables ρ, u, v, p . The control volumes that do not pass the admissibility criteria outlined in Eq. (109) are marked as a troubled cells by assigning a limiter status $\beta_{i,j} = 1$, while in the cells that do not need to be limited we impose $\beta_{i,j} = 0$. Then, similarly to the 1D case we limit properly also the cells of the staggered dual grids. For example, if the control volume $T_{i,j}$ is flagged as limited zone with $\beta_{i,j} = 1$, then also the four corresponding cells on the dual grids $T_{i+\frac{1}{2},j}, T_{i-\frac{1}{2},j}, T_{i,j+\frac{1}{2}}$ and $T_{i,j-\frac{1}{2}}$ need to be limited by assigning $\beta_{i+\frac{1}{2},j} = 1, \beta_{i-\frac{1}{2},j} = 1, \beta_{i,j+\frac{1}{2}} = 1$ and $\beta_{i,j-\frac{1}{2}} = 1$. In addition, in the rare case that the conjugate gradient does not converge all the control volumes of the domain are marked as troubled cells. Finally, in the first MOOD step the implicitness parameter θ is chosen between 0.5 and 1. In general, in order to reduce the numerical viscosity of the time integration, we impose $\theta_{DG} = 0.55$ in the entire domain. However, at the second MOOD phase θ is changed and imposed equal to $\theta = 1$ in the troubled control volumes, in order to avoid the generation of Gibbs oscillations, while it is kept equal to $\theta = \theta_{DG}$ in all the unlimited cells.

3.5 Sub-cell Limiting of the Semi-implicit DG Scheme for the 2D Euler Equations

Now, the total energy equation is discretized in the presence of subcell limiter, where we have consider four possible configurations. In all cases $T_{i,j}$ is unlimited ($\beta_{i,j} = 0$), but one of its edge neighbours is a troubled cell. We write the equation as follows

$$\mathbf{M}^{\mathbf{x}\mathbf{y}} \cdot \left(\widehat{\rho e}_{i,j}^{n+1} + \widehat{\rho k}_{i,j}^{n+1} - \widehat{\rho E}_{i,j}^* \right) + \frac{\Delta t}{\Delta x} \mathbf{M}^{\mathbf{y}} \cdot \widehat{\Delta h \rho u}_{i,j}^{n+\theta_{i,j}} + \frac{\Delta t}{\Delta y} \mathbf{M}^{\mathbf{y}} \cdot \widehat{\Delta h \rho v}_{i,j}^{n+\theta_{i,j}} = 0. \quad (110)$$

We distinguish two cases for $\widehat{\Delta h \rho u}_{i,j}^{n+\theta_{i,j}}$:

$$\widehat{\Delta h \rho u}_{i,j}^{n+\theta_{i,j}} = \begin{cases} \mathbf{R}_e^{\mathbf{x}, \text{Lim}} \cdot \mathbb{W}^y \left(\widehat{h \rho u}_{i+\frac{1}{2},j}^{n+\theta_{i+\frac{1}{2},j}} \right) - \mathbf{L}_e^{\mathbf{x}, \text{DG}} \cdot \widehat{h}_{i-\frac{1}{2},j}^{n+\theta_{i-\frac{1}{2},j},j} \widehat{\rho u}_{i-\frac{1}{2},j}^{n+\theta_{i-\frac{1}{2},j},j} & \text{if } \beta_{i+\frac{1}{2},j} = 1, \beta_{i-\frac{1}{2},j} = 0, \\ \mathbf{R}_e^{\mathbf{x}, \text{DG}} \cdot \widehat{h}_{i+\frac{1}{2},j}^{n+\theta_{i+\frac{1}{2},j}} \widehat{\rho u}_{i+\frac{1}{2},j}^{n+\theta_{i+\frac{1}{2},j}} - \mathbf{L}_e^{\mathbf{x}, \text{Lim}} \cdot \mathbb{W}^y \left(\widehat{h \rho u}_{i-\frac{1}{2},j}^{n+\theta_{i-\frac{1}{2},j}} \right) & \text{if } \beta_{i+\frac{1}{2},j} = 0, \beta_{i-\frac{1}{2},j} = 1. \end{cases} \quad (111)$$

The first corresponds to the case when the cell $T_{i+1,j}$ is troubled and consequently $\beta_{i+1,j} = \beta_{i+\frac{1}{2},j} = 1$; on the contrary the other situation is when the control volume $T_{i-1,j}$ is a troubled cell. Similarly, the two cases for $\widehat{\Delta h \rho v}_{i,j}^{n+\theta_{i,j}}$ read

$$\widehat{\Delta h \rho v}_{i,j}^{n+\theta_{i,j}} = \begin{cases} \mathbf{R}_e^{\mathbf{y}, \text{Lim}} \cdot \mathbb{W}^x \left(\widehat{h \rho v}_{i,j+\frac{1}{2}}^{n+\theta_{i,j+\frac{1}{2}}} \right) - \mathbf{L}_e^{\mathbf{y}, \text{DG}} \cdot \widehat{h}_{i,j-\frac{1}{2}}^{n+\theta_{i,j-\frac{1}{2}},j} \widehat{\rho v}_{i,j-\frac{1}{2}}^{n+\theta_{i,j-\frac{1}{2}},j} & \text{if } \beta_{i,j+\frac{1}{2}} = 1, \beta_{i,j-\frac{1}{2}} = 0, \\ \mathbf{R}_e^{\mathbf{y}, \text{DG}} \cdot \widehat{h}_{i,j+\frac{1}{2}}^{n+\theta_{i,j+\frac{1}{2}}} \widehat{\rho v}_{i,j+\frac{1}{2}}^{n+\theta_{i,j+\frac{1}{2}}} - \mathbf{L}_e^{\mathbf{y}, \text{Lim}} \cdot \mathbb{W}^x \left(\widehat{h \rho v}_{i,j-\frac{1}{2}}^{n+\theta_{i,j-\frac{1}{2}}} \right) & \text{if } \beta_{i,j+\frac{1}{2}} = 0, \beta_{i,j-\frac{1}{2}} = 1. \end{cases} \quad (112)$$

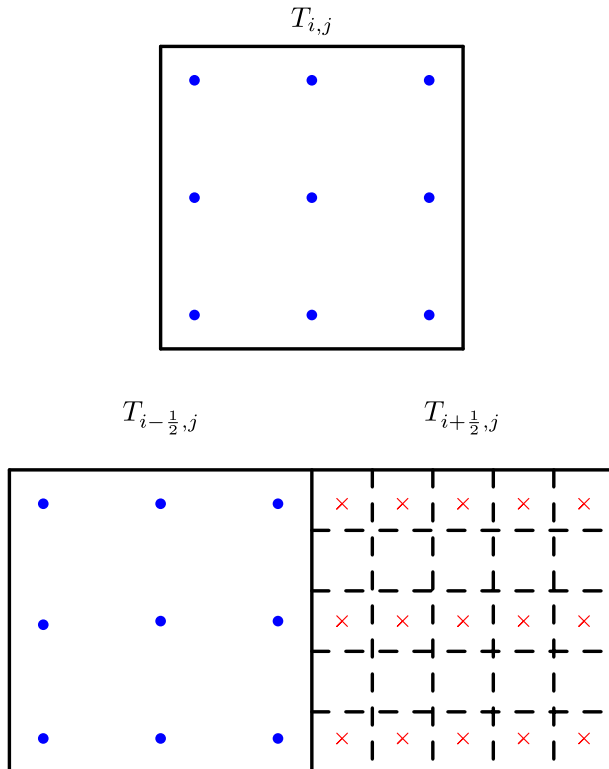


Fig. 10 Reconstruction done by the operator \mathbb{W}^y used in the continuity equation of the limited scheme. The red crosses in $T_{i+1/2,j}$ are the new degrees of freedom obtained applying the \mathbb{W}^y operator the DG degrees of freedom in $T_{i+1/2,j}$ (Color figure online)

In Eqs. (111) and (112) we used the two operators \mathbb{W}^x and \mathbb{W}^y that are used in order to have consistent tensor products. Looking at Fig. 10 the operator \mathbb{W}^y works on the finite volume subcell averages and does a reconstruction of the DG polynomial only y direction producing the red symbols. The operator \mathbb{W}^y does a similar reconstruction in x direction. We remind that when all the four control volumes $T_{i\pm 1/2,j}$ and $T_{i,j\pm 1/2}$ are not marked the discrete total energy equation is discretized using the pure DG scheme and it corresponds to Eq. (83) derived in Sect. 3.2.2. On the contrary, if all the four cells are troubled control volumes, then the subcell averages of the total energy are given by Eq. (99), see Sect. 3.3.

Now we consider the limited case of the momentum equation in x direction. When $T_{i+1/2,j}$ is limited ($\beta_{i+1/2,j} = 1$), we consider two cases. If $\beta_{i+1/2,j} = \beta_{i,j} = 1$ and $\beta_{i+1,j} = 0$, the momentum update reads

$$\overline{\rho u}_{i+1/2,j}^{n+1} = \overline{\rho u}_{i+1/2,j}^* - \frac{\Delta t}{\Delta x} \left(\mathbf{R}_u^{x,\text{Lim}} \cdot \mathbb{P}^y \left(\hat{\mathbf{p}}_{i+1,j}^{n+\theta_{i+1/2,j}} \right) - \mathbf{L}_u^{x,\text{FV}} \cdot \overline{\mathbf{p}}_{i,j}^{n+\theta_{i+1/2,j}} \right) \quad (113)$$

while for the other case, $\beta_{i+1/2,j} = \beta_{i+1,j} = 1$ and $\beta_{i,j} = 0$, we have

$$\overline{\rho u}_{i+1/2,j}^{n+1} = \overline{\rho u}_{i+1/2,j}^* - \frac{\Delta t}{\Delta x} \left(\mathbf{R}_u^{x,\text{FV}} \cdot \overline{\mathbf{p}}_{i+1,j}^{n+\theta_{i+1/2,j}} - \mathbf{L}_u^{x,\text{Lim}} \cdot \mathbb{P}^y \left(\hat{\mathbf{p}}_{i,j}^{n+\theta_{i+1/2,j}} \right) \right). \quad (114)$$

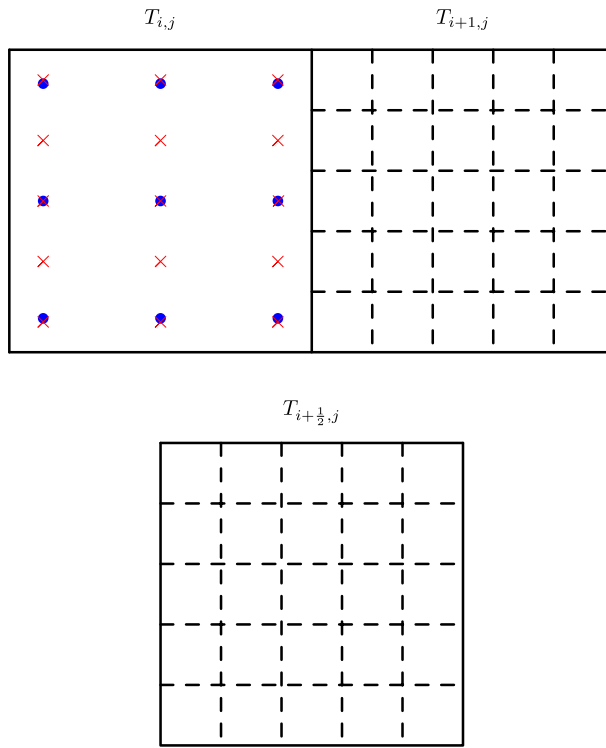


Fig. 11 Projection done by the operator \mathbb{P}^y used in the momentum equation of the limited scheme. The red crosses in $T_{i,j}$ are the new degrees of freedom obtained applying the \mathbb{P}^y operator the DG degrees of freedom in $T_{i,j}$ (Color figure online)

Similarly in y direction the two possibilities of the momentum equation are

$$\bar{\rho}v_{i,j+\frac{1}{2}}^{n+1} = \bar{\rho}v_{i,j+\frac{1}{2}}^* - \frac{\Delta t}{\Delta y} \left(\mathbf{R}_u^y \cdot \mathbf{Lim} \cdot \mathbb{P}^x \left(\hat{p}_{i,j+1}^{n+\theta_{i,j+\frac{1}{2}}} \right) - \mathbf{Ly} \cdot \mathbf{FV} \cdot \bar{p}_{i,j}^{n+\theta_{i,j+\frac{1}{2}}} \right) \quad (115)$$

if $\beta_{i,j+\frac{1}{2}} = \beta_{i,j} = 1$ and $\beta_{i,j+1} = 0$, and for the other case

$$\bar{\rho}v_{i,j+\frac{1}{2}}^{n+1} = \bar{\rho}v_{i,j+\frac{1}{2}}^* - \frac{\Delta t}{\Delta y} \left(\mathbf{R}^y \cdot \mathbf{FV} \cdot \bar{p}_{i,j+1}^{n+\theta_{i,j+\frac{1}{2}}} - \mathbf{L}_u^y \cdot \mathbf{Lim} \cdot \mathbb{P}^x \left(\hat{p}_{i,j}^{n+\theta_{i,j+\frac{1}{2}}} \right) \right) \quad (116)$$

if $\beta_{i,j+\frac{1}{2}} = \beta_{i,j+1} = 1$ and $\beta_{i,j} = 0$. Also for the limited momentum equations we introduced the operators \mathbb{P}^y and \mathbb{P}^x that are necessary in order to multiply properly the tensors and the degrees of freedom. See Fig. 11 for a schematic representation of the projection done in y direction by \mathbb{P}^y . Then, the linear system for the 2D semi-implicit limited staggered DG reads

$$\mathcal{L}_{i,j}^{x,\text{Lim}} \cdot \tilde{p}_{i-1,j}^{n+1,r+1} + \mathcal{L}_{i,j}^{y,\text{Lim}} \cdot \tilde{p}_{i,j-1}^{n+1,r+1} + \mathcal{C}_{i,j}^{\text{Lim}} \cdot \tilde{p}_{i,j}^{n+1,r+1} + \mathcal{R}_{i,j}^{x,\text{Lim}} \cdot \tilde{p}_{i+1,j}^{n+1,r+1} + \mathcal{R}_{i,j}^{y,\text{Lim}} \cdot \tilde{p}_{i,j+1}^{n+1,r+1} = \tilde{b}_{i,j}^r, \quad (117)$$

which appears to be symmetric in practice, but we are not able to provide a rigorous proof of this property yet. The blocks $\mathcal{R}_{i,j}^{x,\text{Lim}}$, $\mathcal{L}_{i,j}^{x,\text{Lim}}$, $\mathcal{R}_{i,j}^{y,\text{Lim}}$, $\mathcal{L}_{i,j}^{y,\text{Lim}}$ are computed as follows

$$\mathcal{R}_{i,j}^{x,\text{Lim}} = -\frac{\Delta t^2}{\Delta x^2} \theta_{i+\frac{1}{2},j}^2 \begin{cases} \mathbf{M}^y \cdot \mathbf{R}_e^{x,\text{DG}} \cdot \hat{\mathbf{h}}_{i+\frac{1}{2},j}^{n+1} \cdot (\mathbf{M}^x)^{-1} \cdot \mathbf{R}_u^{x,\text{DG}} & \text{if } \beta_{i+1,j} = \beta_{i,j} = 0, \\ \mathbf{R}^{x,\text{FV}} \cdot \mathcal{D}^x(\bar{\mathbf{h}}_{i+\frac{1}{2},j}^{n+1}) \cdot \mathbf{R}^{x,\text{FV}} & \text{if } \beta_{i+1,j} = \beta_{i,j} = 1, \\ \mathbf{M}^y \cdot \mathbf{R}_e^{x,\text{Lim}} \cdot \mathcal{D}^x(\mathbb{W}^y(\bar{\mathbf{h}}_{i+\frac{1}{2},j}^{n+1})) \cdot \mathbf{R}^{x,\text{FV}} & \text{if } \beta_{i+1,j} = 1, \beta_{i,j} = 0, \\ \mathbf{R}^{x,\text{FV}} \cdot \mathcal{D}^x(\bar{\mathbf{h}}_{i+\frac{1}{2},j}^{n+1}) \cdot \mathbf{R}_u^{x,\text{Lim}} & \text{if } \beta_{i+1,j} = 0, \beta_{i,j} = 1. \end{cases} \quad (118)$$

$$\mathcal{R}_{i,j}^{y,\text{Lim}} = -\frac{\Delta t^2}{\Delta y^2} \theta_{i,j+\frac{1}{2}}^2 \begin{cases} \mathbf{M}^x \cdot \mathbf{R}_e^{y,\text{DG}} \cdot \hat{\mathbf{h}}_{i,j+\frac{1}{2}}^{n+1} \cdot (\mathbf{M}^y)^{-1} \cdot \mathbf{R}_u^{y,\text{DG}} & \text{if } \beta_{i,j+1} = \beta_{i,j} = 0, \\ \mathbf{R}^{y,\text{FV}} \cdot \mathcal{D}^y(\bar{\mathbf{h}}_{i,j+\frac{1}{2}}^{n+1}) \cdot \mathbf{R}^{y,\text{FV}} & \text{if } \beta_{i,j+1} = \beta_{i,j} = 1, \\ \mathbf{M}^x \cdot \mathbf{R}_e^{y,\text{Lim}} \cdot \mathcal{D}^y(\mathbb{W}^x(\bar{\mathbf{h}}_{i,j+\frac{1}{2}}^{n+1})) \cdot \mathbf{R}^{y,\text{FV}} & \text{if } \beta_{i,j+1} = 1, \beta_{i,j} = 0, \\ \mathbf{R}^{y,\text{FV}} \cdot \mathcal{D}^y(\bar{\mathbf{h}}_{i,j+\frac{1}{2}}^{n+1}) \cdot \mathbf{R}_u^{y,\text{Lim}} & \text{if } \beta_{i,j+1} = 0, \beta_{i,j} = 1. \end{cases} \quad (119)$$

$$\mathcal{L}_{i,j}^{x,\text{Lim}} = -\frac{\Delta t^2}{\Delta x^2} \theta_{i-\frac{1}{2},j}^2 \begin{cases} \mathbf{M}^y \cdot \mathbf{L}_e^{x,\text{DG}} \cdot \hat{\mathbf{h}}_{i-\frac{1}{2},j}^{n+1} \cdot (\mathbf{M}^x)^{-1} \cdot \mathbf{L}_u^{x,\text{DG}} & \text{if } \beta_{i-1,j} = \beta_{i,j} = 0, \\ \mathbf{L}^{x,\text{FV}} \cdot \mathcal{D}^x(\bar{\mathbf{h}}_{i-\frac{1}{2},j}^{n+1}) \cdot \mathbf{L}^{x,\text{FV}} & \text{if } \beta_{i-1,j} = \beta_{i,j} = 1, \\ \mathbf{M}^y \cdot \mathbf{L}_e^{x,\text{Lim}} \cdot \mathcal{D}^x(\mathbb{W}^y(\bar{\mathbf{h}}_{i-\frac{1}{2},j}^{n+1})) \cdot \mathbf{L}^{x,\text{FV}} & \text{if } \beta_{i-1,j} = 1, \beta_{i,j} = 0, \\ \mathbf{L}^{x,\text{FV}} \cdot \mathcal{D}^x(\bar{\mathbf{h}}_{i-\frac{1}{2},j}^{n+1}) \cdot \mathbf{L}_u^{x,\text{Lim}} & \text{if } \beta_{i-1,j} = 0, \beta_{i,j} = 1. \end{cases} \quad (120)$$

$$\mathcal{L}_{i,j}^{y,\text{Lim}} = -\frac{\Delta t^2}{\Delta x^2} \theta_{i,j-\frac{1}{2}}^2 \begin{cases} \mathbf{M}^x \cdot \mathbf{L}_e^{y,\text{DG}} \cdot \hat{\mathbf{h}}_{i,j-\frac{1}{2}}^{n+1} \cdot (\mathbf{M}^y)^{-1} \cdot \mathbf{L}_u^{y,\text{DG}} & \text{if } \beta_{i,j-1} = \beta_{i,j} = 0, \\ \mathbf{L}^{y,\text{FV}} \cdot \mathcal{D}^y(\bar{\mathbf{h}}_{i,j-\frac{1}{2}}^{n+1}) \cdot \mathbf{L}^{y,\text{FV}} & \text{if } \beta_{i,j-1} = \beta_{i,j} = 1, \\ \mathbf{M}^x \cdot \mathbf{L}_e^{y,\text{Lim}} \cdot \mathcal{D}^y(\mathbb{W}^x(\bar{\mathbf{h}}_{i,j-\frac{1}{2}}^{n+1})) \cdot \mathbf{L}^{y,\text{FV}} & \text{if } \beta_{i,j-1} = 1, \beta_{i,j} = 0, \\ \mathbf{L}^{y,\text{FV}} \cdot \mathcal{D}^y(\bar{\mathbf{h}}_{i,j-\frac{1}{2}}^{n+1}) \cdot \mathbf{L}_u^{y,\text{Lim}} & \text{if } \beta_{i,j-1} = 0, \beta_{i,j} = 1. \end{cases} \quad (121)$$

while a proper splitting for $\mathcal{C}_{i,j}^{\text{Lim}}$ yields

$$\mathcal{C}_{i,j}^{\text{Lim}} = \mathcal{C}_{i,j}^{0,\text{Lim}} + \mathcal{C}_{i,j}^{x,\text{Lim}} + \mathcal{C}_{i,j}^{y,\text{Lim}}, \quad (122)$$

with

$$C_{i,j}^{0,\text{Lim}} = \begin{cases} M^{\text{xy}} & \text{if } \beta_{i,j} = 0, \\ I & \text{if } \beta_{i,j} = 1. \end{cases} \quad (123)$$

$$C_{i,j}^{x,\text{Lim}} = \frac{\Delta t^2}{\Delta x^2} \begin{cases} M^y \left(\theta_{i-\frac{1}{2},j}^2 \cdot R_e^x \cdot D_G \cdot \hat{h}_{i-\frac{1}{2},j}^{n+1} \cdot (M^x)^{-1} \cdot L_u^x \cdot D_G + \theta_{i+\frac{1}{2},j}^2 \cdot R_e^x \cdot D_G \cdot \hat{h}_{i+\frac{1}{2},j}^{n+1} \cdot (M^x)^{-1} \cdot R_u^x \cdot D_G \right) \\ \text{if } \beta_{i,j} = \beta_{i-\frac{1}{2},j} = \beta_{i+\frac{1}{2},j} = 0, \\ \theta_{i-\frac{1}{2},j}^2 \cdot L^x \cdot FV \cdot D^x \left(\bar{h}_{i-\frac{1}{2},j}^{n+1} \right) \cdot R^x \cdot FV + \theta_{i+\frac{1}{2},j}^2 \cdot R^x \cdot FV \cdot D^x \left(\bar{h}_{i+\frac{1}{2},j}^{n+1} \right) \cdot L^x \cdot FV \\ \text{if } \beta_{i,j} = \beta_{i-\frac{1}{2},j} = \beta_{i+\frac{1}{2},j} = 1, \\ M^y \left(\theta_{i-\frac{1}{2},j}^2 \cdot R_e^x \cdot D_G \cdot \hat{h}_{i-\frac{1}{2},j}^{n+1} \cdot (M^x)^{-1} \cdot L_u^x \cdot D_G + \theta_{i+\frac{1}{2},j}^2 \cdot R_e^x \cdot D_G \cdot \hat{h}_{i+\frac{1}{2},j}^{n+1} \cdot (M^x)^{-1} \cdot R_u^x \cdot D_G \right) \\ \text{if } \beta_{i,j} = \beta_{i-\frac{1}{2},j} = 0, \beta_{i+\frac{1}{2},j} = 1, \\ M^y \left(\theta_{i-\frac{1}{2},j}^2 \cdot L_e^x \cdot D_G \cdot \hat{h}_{i-\frac{1}{2},j}^{n+1} \cdot (M^x)^{-1} \cdot R_u^x \cdot D_G \right) \\ \text{if } \beta_{i,j} = \beta_{i+\frac{1}{2},j} = 0, \beta_{i-\frac{1}{2},j} = 1, \end{cases} \quad (124)$$

$$C_{i,j}^{y,\text{Lim}} = \frac{\Delta t^2}{\Delta y^2} \begin{cases} M^x \left(\theta_{i,j-\frac{1}{2}}^2 \cdot R_e^y \cdot D_G \cdot \hat{h}_{i,j-\frac{1}{2}}^{n+1} \cdot (M^y)^{-1} \cdot L_u^y \cdot D_G + \theta_{i,j+\frac{1}{2}}^2 \cdot L_e^y \cdot D_G \cdot \hat{h}_{i,j+\frac{1}{2}}^{n+1} \cdot (M^y)^{-1} \cdot R_u^y \cdot D_G \right) \\ \text{if } \beta_{i,j} = \beta_{i,j-\frac{1}{2}} = \beta_{i,j+\frac{1}{2}} = 0, \\ \theta_{i,j-\frac{1}{2}}^2 \cdot L^y \cdot FV \cdot D^y \left(\bar{h}_{i,j-\frac{1}{2}}^{n+1} \right) \cdot R^y \cdot FV + \theta_{i,j+\frac{1}{2}}^2 \cdot R^y \cdot FV \cdot D^y \left(\bar{h}_{i,j+\frac{1}{2}}^{n+1} \right) \cdot L^y \cdot FV \\ \text{if } \beta_{i,j} = \beta_{i,j-\frac{1}{2}} = \beta_{i,j+\frac{1}{2}} = 1, \\ M^x \left(\theta_{i,j-\frac{1}{2}}^2 \cdot R_e^y \cdot D_G \cdot \hat{h}_{i,j-\frac{1}{2}}^{n+1} \cdot (M^y)^{-1} \cdot L_u^y \cdot D_G + \theta_{i,j+\frac{1}{2}}^2 \cdot R_e^y \cdot D_G \cdot \hat{h}_{i,j+\frac{1}{2}}^{n+1} \cdot (M^y)^{-1} \cdot R_u^y \cdot D_G \right) \\ \text{if } \beta_{i,j} = \beta_{i,j-\frac{1}{2}} = 0, \beta_{i,j+\frac{1}{2}} = 1, \\ M^x \left(\theta_{i-\frac{1}{2},j}^2 \cdot L_e^y \cdot D_G \cdot \hat{h}_{i-\frac{1}{2},j}^{n+1} \cdot (M^y)^{-1} \cdot R_u^y \cdot D_G \right) \\ \text{if } \beta_{i,j} = \beta_{i,j+\frac{1}{2}} = 0, \beta_{i,j-\frac{1}{2}} = 1. \end{cases} \quad (125)$$

We consider three contributions for the right hand side term

$$\tilde{b}_{i,j}^r = \tilde{b}_{i,j}^{0,n} + \tilde{b}_{i,j}^{x,n} + \tilde{b}_{i,j}^{y,n} \quad (126)$$

with

$$\tilde{b}_{i,j}^{0,r} = \begin{cases} M^{\text{xy}} \cdot (\widehat{\rho E}_{i,j}^* - \widehat{\rho}_{i,j}^{n+1} \widehat{k}_{i,j}^{n+1,r}) & \text{if } \beta_{i,j} = 0, \\ \overline{\rho E}_{i,j}^* - \overline{\rho}_{i,j}^{n+1} \overline{k}_{i,j}^{n+1,r} & \text{if } \beta_{i,j} = 1, \end{cases} \quad (127)$$

$$\tilde{b}_{i,j}^{x,r} = -\frac{\Delta t}{\Delta x} \left\{ \begin{array}{l} \left(\theta_{i+\frac{1}{2},j} \mathbf{R}_e^{\mathbf{x},\text{DG}} \cdot \hat{\mathbf{h}}_{i+\frac{1}{2},j}^{n+1} \hat{\mathbf{G}}_{i+\frac{1}{2},j}^n - \theta_{i-\frac{1}{2},j} \mathbf{L}_e^{\mathbf{x},\text{DG}} \cdot \hat{\mathbf{h}}_{i-\frac{1}{2},j}^{n+1} \hat{\mathbf{G}}_{i-\frac{1}{2},j}^n \right) \\ + \left(\left(1 - \theta_{i+\frac{1}{2},j} \right) \mathbf{R}_e^{\mathbf{x},\text{DG}} \cdot \hat{\mathbf{h}}_{i+\frac{1}{2},j}^n \bar{\rho} \bar{\mathbf{u}}_{i+\frac{1}{2},j}^n - \left(1 - \theta_{i-\frac{1}{2},j} \right) \mathbf{L}_e^{\mathbf{x},\text{DG}} \cdot \hat{\mathbf{h}}_{i-\frac{1}{2},j}^n \bar{\rho} \bar{\mathbf{u}}_{i-\frac{1}{2},j}^n \right) \\ \quad \text{if } \beta_{i,j} = \beta_{i-\frac{1}{2},j} = \beta_{i+\frac{1}{2},j} = 0, \\ \left(\theta_{i+\frac{1}{2},j} \mathbf{R}_e^{\mathbf{x},\text{FV}} \cdot \bar{\mathbf{h}}_{i+\frac{1}{2},j}^n \bar{\mathbf{G}}_{i+\frac{1}{2},j}^n - \theta_{i-\frac{1}{2},j} \mathbf{L}_e^{\mathbf{x},\text{FV}} \cdot \bar{\mathbf{h}}_{i-\frac{1}{2},j}^n \bar{\mathbf{G}}_{i-\frac{1}{2},j}^n \right) \\ + \left(\left(1 - \theta_{i+\frac{1}{2},j} \right) \mathbf{R}_e^{\mathbf{x},\text{FV}} \cdot \bar{\rho} \bar{\mathbf{u}}_{i+\frac{1}{2},j}^n - \left(1 - \theta_{i-\frac{1}{2},j} \right) \mathbf{L}_e^{\mathbf{x},\text{FV}} \cdot \bar{\rho} \bar{\mathbf{u}}_{i-\frac{1}{2},j}^n \right) \\ \quad \text{if } \beta_{i,j} = \beta_{i-\frac{1}{2},j} = \beta_{i+\frac{1}{2},j} = 1, \\ \left(\theta_{i+\frac{1}{2},j} \mathbf{R}_e^{\mathbf{x},\text{Lim}} \cdot \mathbb{W}^y \left(\bar{\mathbf{h}}_{i+\frac{1}{2},j}^{n+1} \bar{\mathbf{G}}_{i+\frac{1}{2},j}^n \right) - \theta_{i-\frac{1}{2},j} \mathbf{L}_e^{\mathbf{x},\text{DG}} \cdot \hat{\mathbf{h}}_{i-\frac{1}{2},j}^{n+1} \hat{\mathbf{G}}_{i-\frac{1}{2},j}^n \right) \\ + \left(\left(1 - \theta_{i+\frac{1}{2},j} \right) \mathbf{R}_e^{\mathbf{x},\text{Lim}} \cdot \mathbb{W}^y \left(\bar{\rho} \bar{\mathbf{u}}_{i+\frac{1}{2},j}^n \right) - \left(1 - \theta_{i-\frac{1}{2},j} \right) \mathbf{L}_e^{\mathbf{x},\text{DG}} \cdot \hat{\mathbf{h}}_{i-\frac{1}{2},j}^n \bar{\rho} \bar{\mathbf{u}}_{i-\frac{1}{2},j}^n \right) \\ \quad \text{if } \beta_{i,j} = \beta_{i-\frac{1}{2},j} = 0, \beta_{i+\frac{1}{2},j} = 1, \\ \left(\theta_{i+\frac{1}{2},j} \mathbf{R}_e^{\mathbf{x},\text{DG}} \cdot \hat{\mathbf{h}}_{i+\frac{1}{2},j}^{n+1} \hat{\mathbf{G}}_{i+\frac{1}{2},j}^n - \theta_{i-\frac{1}{2},j} \mathbf{L}_e^{\mathbf{x},\text{Lim}} \cdot \mathbb{W}^y \left(\bar{\mathbf{h}}_{i-\frac{1}{2},j}^{n+1} \bar{\mathbf{G}}_{i-\frac{1}{2},j}^n \right) \right) \\ + \left(\left(1 - \theta_{i+\frac{1}{2},j} \right) \mathbf{R}_e^{\mathbf{x},\text{DG}} \cdot \hat{\mathbf{h}}_{i+\frac{1}{2},j}^n \bar{\rho} \bar{\mathbf{u}}_{i+\frac{1}{2},j}^n - \left(1 - \theta_{i-\frac{1}{2},j} \right) \mathbf{L}_e^{\mathbf{x},\text{Lim}} \cdot \mathbb{W}^y \left(\bar{\rho} \bar{\mathbf{u}}_{i-\frac{1}{2},j}^n \right) \right) \\ \quad \text{if } \beta_{i,j} = \beta_{i+\frac{1}{2},j} = 0, \beta_{i-\frac{1}{2},j} = 1. \end{array} \right. \quad (128)$$

$$\tilde{b}_{i,j}^{y,r} = -\frac{\Delta t}{\Delta y} \left\{ \begin{array}{l} \left(\theta_{i,j+\frac{1}{2}} \mathbf{R}_e^{\mathbf{y},\text{DG}} \cdot \hat{\mathbf{h}}_{i,j+\frac{1}{2}}^{n+1} \hat{\mathbf{G}}_{i,j+\frac{1}{2}}^n - \theta_{i,j-\frac{1}{2}} \mathbf{L}_e^{\mathbf{y},\text{DG}} \cdot \hat{\mathbf{h}}_{i,j-\frac{1}{2}}^{n+1} \hat{\mathbf{G}}_{i,j-\frac{1}{2}}^n \right) \\ + \left(\left(1 - \theta_{i,j+\frac{1}{2}} \right) \mathbf{R}_e^{\mathbf{y},\text{DG}} \cdot \hat{\mathbf{h}}_{i,j+\frac{1}{2}}^n \bar{\rho} \bar{\mathbf{u}}_{i,j+\frac{1}{2}}^n - \left(1 - \theta_{i,j-\frac{1}{2}} \right) \mathbf{L}_e^{\mathbf{y},\text{DG}} \cdot \hat{\mathbf{h}}_{i,j-\frac{1}{2}}^n \bar{\rho} \bar{\mathbf{u}}_{i,j-\frac{1}{2}}^n \right) \\ \quad \text{if } \beta_{i,j} = \beta_{i,j-\frac{1}{2}} = \beta_{i,j+\frac{1}{2}} = 0, \\ \left(\theta_{i,j+\frac{1}{2}} \mathbf{R}_e^{\mathbf{y},\text{FV}} \cdot \bar{\mathbf{h}}_{i,j+\frac{1}{2}}^n \bar{\mathbf{G}}_{i,j+\frac{1}{2}}^n - \theta_{i,j-\frac{1}{2}} \mathbf{L}_e^{\mathbf{y},\text{FV}} \cdot \bar{\mathbf{h}}_{i,j-\frac{1}{2}}^n \bar{\mathbf{G}}_{i,j-\frac{1}{2}}^n \right) \\ + \left(\left(1 - \theta_{i,j+\frac{1}{2}} \right) \mathbf{R}_e^{\mathbf{y},\text{FV}} \cdot \bar{\rho} \bar{\mathbf{u}}_{i,j+\frac{1}{2}}^n - \left(1 - \theta_{i,j-\frac{1}{2}} \right) \mathbf{L}_e^{\mathbf{y},\text{FV}} \cdot \bar{\rho} \bar{\mathbf{u}}_{i,j-\frac{1}{2}}^n \right) \\ \quad \text{if } \beta_{i,j} = \beta_{i,j-\frac{1}{2}} = \beta_{i,j+\frac{1}{2}} = 1, \\ \left(\theta_{i,j+\frac{1}{2}} \mathbf{R}_e^{\mathbf{y},\text{Lim}} \cdot \mathbb{W}^x \left(\bar{\mathbf{h}}_{i,j+\frac{1}{2}}^{n+1} \bar{\mathbf{G}}_{i,j+\frac{1}{2}}^n \right) - \theta_{i,j-\frac{1}{2}} \mathbf{L}_e^{\mathbf{y},\text{DG}} \cdot \hat{\mathbf{h}}_{i,j-\frac{1}{2}}^{n+1} \hat{\mathbf{G}}_{i,j-\frac{1}{2}}^n \right) \\ + \left(\left(1 - \theta_{i,j+\frac{1}{2}} \right) \mathbf{R}_e^{\mathbf{y},\text{Lim}} \cdot \mathbb{W}^x \left(\bar{\rho} \bar{\mathbf{u}}_{i,j+\frac{1}{2}}^n \right) - \left(1 - \theta_{i,j-\frac{1}{2}} \right) \mathbf{L}_e^{\mathbf{y},\text{DG}} \cdot \hat{\mathbf{h}}_{i,j-\frac{1}{2}}^n \bar{\rho} \bar{\mathbf{u}}_{i,j-\frac{1}{2}}^n \right) \\ \quad \text{if } \beta_{i,j} = \beta_{i,j-\frac{1}{2}} = 0, \beta_{i,j+\frac{1}{2}} = 1, \\ \left(\theta_{i,j+\frac{1}{2}} \mathbf{R}_e^{\mathbf{y},\text{DG}} \cdot \hat{\mathbf{h}}_{i,j+\frac{1}{2}}^{n+1} \hat{\mathbf{G}}_{i,j+\frac{1}{2}}^n - \theta_{i,j-\frac{1}{2}} \mathbf{L}_e^{\mathbf{y},\text{Lim}} \cdot \mathbb{W}^x \left(\bar{\mathbf{h}}_{i,j-\frac{1}{2}}^{n+1} \bar{\mathbf{G}}_{i,j-\frac{1}{2}}^n \right) \right) \\ + \left(\left(1 - \theta_{i,j+\frac{1}{2}} \right) \mathbf{R}_e^{\mathbf{y},\text{DG}} \cdot \hat{\mathbf{h}}_{i,j+\frac{1}{2}}^n \bar{\rho} \bar{\mathbf{u}}_{i,j+\frac{1}{2}}^n - \left(1 - \theta_{i,j-\frac{1}{2}} \right) \mathbf{L}_e^{\mathbf{y},\text{Lim}} \cdot \mathbb{W}^x \left(\bar{\rho} \bar{\mathbf{u}}_{i,j-\frac{1}{2}}^n \right) \right) \\ \quad \text{if } \beta_{i,j} = \beta_{i,j+\frac{1}{2}} = 0, \beta_{i,j-\frac{1}{2}} = 1. \end{array} \right. \quad (129)$$

Then, the projections from the main grid to staggered grids in x and y direction are

$$\tilde{\rho}_{i+\frac{1}{2},j} = \begin{cases} (\mathbf{M}^x)^{-1} \cdot (\mathbf{M}_L^{x,DG} \cdot \hat{\rho}_{i,j} + \mathbf{M}_R^{x,DG} \cdot \hat{\rho}_{i+1,j}) & \text{if } \beta_{i+\frac{1}{2},j} = \beta_{i,j} = \beta_{i+1,j} = 0, \\ (\mathbf{M}_L^{x,FV} \cdot \bar{\rho}_{i,j} + \mathbf{M}_R^{x,FV} \cdot \bar{\rho}_{i+1,j}) & \text{if } \beta_{i+\frac{1}{2},j} = \beta_{i,j} = \beta_{i+1,j} = 1, \\ (\mathbf{M}_L^{x,FV} \cdot \mathbb{P}^{xy}(\hat{\rho}_{i,j}) + \mathbf{M}_R^{x,FV} \cdot \bar{\rho}_{i+1,j}) & \text{if } \beta_{i+\frac{1}{2},j} = \beta_{i+1,j} = 1, \beta_{i,j} = 0, \\ (\mathbf{M}_L^{x,FV} \cdot \bar{\rho}_{i,j} + \mathbf{M}_R^{x,FV} \cdot \mathbb{P}^{xy}(\hat{\rho}_{i+1,j})) & \text{if } \beta_{i+\frac{1}{2},j} = \beta_{i,j} = 1, \beta_{i+1,j} = 0. \end{cases} \quad (130)$$

$$\tilde{\rho}_{i,j+\frac{1}{2}} = \begin{cases} (\mathbf{M}^y)^{-1} \cdot (\mathbf{M}_L^{y,DG} \cdot \hat{\rho}_{i,j} + \mathbf{M}_R^{y,DG} \cdot \hat{\rho}_{i,j+1}) & \text{if } \beta_{i,j+\frac{1}{2}} = \beta_{i,j} = \beta_{i,j+1} = 0, \\ (\mathbf{M}_L^{y,FV} \cdot \bar{\rho}_{i,j} + \mathbf{M}_R^{y,FV} \cdot \bar{\rho}_{i,j+1}) & \text{if } \beta_{i,j+\frac{1}{2}} = \beta_{i,j} = \beta_{i,j+1} = 1, \\ (\mathbf{M}_L^{y,FV} \cdot \mathbb{P}^{xy}(\hat{\rho}_{i,j}) + \mathbf{M}_R^{y,FV} \cdot \bar{\rho}_{i,j+1}) & \text{if } \beta_{i,j+\frac{1}{2}} = \beta_{i,j+1} = 1, \beta_{i,j} = 0, \\ (\mathbf{M}_L^{y,FV} \cdot \bar{\rho}_{i,j} + \mathbf{M}_R^{y,FV} \cdot \mathbb{P}^{xy}(\hat{\rho}_{i,j+1})) & \text{if } \beta_{i,j+\frac{1}{2}} = \beta_{i,j} = 1, \beta_{i,j+1} = 0. \end{cases} \quad (131)$$

Reciprocally, the projections from the staggered grids to the main mesh are

$$\tilde{u}_{i,j} = \begin{cases} (\mathbf{M}^x)^{-1} \cdot (\mathbf{M}_L^{x,DG} \cdot \hat{u}_{i-\frac{1}{2},j} + \mathbf{M}_R^{x,DG} \cdot \hat{u}_{i+\frac{1}{2},j}) & \text{if } \beta_{i,j} = \beta_{i-\frac{1}{2},j} = \beta_{i+\frac{1}{2},j} = 0, \\ (\mathbf{M}_L^{x,FV} \cdot \bar{u}_{i-\frac{1}{2},j} + \mathbf{M}_R^{x,FV} \cdot \bar{u}_{i+\frac{1}{2},j}) & \text{if } \beta_{i,j} = \beta_{i-\frac{1}{2},j} = \beta_{i+\frac{1}{2},j} = 1, \\ (\mathbf{M}^x)^{-1} \cdot (\mathbf{M}_L^{x,DG} \cdot \hat{u}_{i-\frac{1}{2},j} + \mathbf{M}_R^{x,Lim} \cdot \mathbb{W}^y(\bar{u}_{i+\frac{1}{2},j})) & \text{if } \beta_{i,j} = \beta_{i-\frac{1}{2},j} = 0, \beta_{i+\frac{1}{2},j} = 1, \\ (\mathbf{M}^x)^{-1} \cdot (\mathbf{M}_L^{x,Lim} \cdot \mathbb{W}^y(\bar{u}_{i-\frac{1}{2},j}) + \mathbf{M}_R^{x,DG} \cdot \hat{u}_{i+\frac{1}{2},j}) & \text{if } \beta_{i,j} = \beta_{i+\frac{1}{2},j} = 0, \beta_{i-\frac{1}{2},j} = 1, \end{cases} \quad (132)$$

$$\tilde{v}_{i,j} = \begin{cases} (\mathbf{M}^y)^{-1} \cdot (\mathbf{M}_L^{y,DG} \cdot \hat{v}_{i,j-\frac{1}{2}} + \mathbf{M}_R^{y,DG} \cdot \hat{v}_{i,j+\frac{1}{2}}) & \text{if } \beta_{i,j} = \beta_{i,j-\frac{1}{2}} = \beta_{i,j+\frac{1}{2}} = 0, \\ (\mathbf{M}_L^{y,FV} \cdot \bar{v}_{i,j-\frac{1}{2}} + \mathbf{M}_R^{y,FV} \cdot \bar{v}_{i,j+\frac{1}{2}}) & \text{if } \beta_{i,j} = \beta_{i,j-\frac{1}{2}} = \beta_{i,j+\frac{1}{2}} = 1, \\ (\mathbf{M}^y)^{-1} \cdot (\mathbf{M}_L^{y,DG} \cdot \hat{v}_{i,j-\frac{1}{2}} + \mathbf{M}_R^{y,Lim} \cdot \mathbb{W}^x(\bar{v}_{i,j+\frac{1}{2}})) & \text{if } \beta_{i,j} = \beta_{i,j-\frac{1}{2}} = 0, \beta_{i,j+\frac{1}{2}} = 1, \\ (\mathbf{M}^y)^{-1} \cdot (\mathbf{M}_L^{y,Lim} \cdot \mathbb{W}^x(\bar{v}_{i,j-\frac{1}{2}}) + \mathbf{M}_R^{y,DG} \cdot \hat{v}_{i,j+\frac{1}{2}}) & \text{if } \beta_{i,j} = \beta_{i,j+\frac{1}{2}} = 0, \beta_{i,j-\frac{1}{2}} = 1. \end{cases} \quad (133)$$

The description of the two-dimensional limited method is concluded by discussing the CFL stability condition. The restriction on the time step is given by the stability condition for the explicit update of the nonlinear convective terms. We can easily verify that $\Delta x_s = \Delta x(2P+1)^{-1}$ and $\Delta y_s = \Delta y(2P+1)^{-1}$. Consequently, the time step Δt given in (108) for the subcell finite volume scheme is equivalent to the one expressed in (97) for the pure unlimited high order DG method. Moreover the 2D limited method acknowledges the same time step restriction.

3.6 Staggered Semi-implicit DG Scheme for the 2D Navier Stokes Equations

In this section, we discuss the numerical solution of the Navier–Stokes equations using a staggered semi-implicit Discontinuous Galerkin method starting from the numerical scheme presented in Sect. 3.2.2. The conservations of mass, momentum and energy read as follows

$$\frac{\partial \rho}{\partial t} + \nabla \cdot (\rho \mathbf{v}) = 0,$$

$$\begin{aligned} \frac{\partial \rho \mathbf{v}}{\partial t} + \nabla(\rho \mathbf{v} \otimes \mathbf{v}) + \nabla p &= \nabla \cdot \boldsymbol{\sigma}, \\ \frac{\partial \rho E}{\partial t} + \nabla \cdot (\mathbf{v}(\rho E + p)) &= \nabla \cdot (\boldsymbol{\sigma} \mathbf{v}), \end{aligned} \quad (134)$$

where $\boldsymbol{\sigma}$ is the stress tensor

$$\boldsymbol{\sigma} = \mu(\nabla \mathbf{v} + \nabla \mathbf{v}^T) - \frac{2}{3}\mu(\nabla \cdot \mathbf{v})\mathbf{I} \quad (135)$$

and μ is the dynamic viscosity. The system of PDE (134) can be written in the following form

$$\frac{\partial \mathbf{Q}}{\partial t} + \nabla \cdot \mathbf{F} = 0 \quad \text{with } \mathbf{F} = \mathbf{F}^c + \mathbf{F}^p + \mathbf{F}^v \quad (136)$$

where \mathbf{Q} , \mathbf{F}^c and \mathbf{F}^p are the same vectors presented in Sect. 3.1 while $\mathbf{F}^v = [\mathbf{F}_x^v, \mathbf{F}_y^v]$ is the viscous flux and its components are expressed as

$$\mathbf{F}_x^v = -[\sigma_{11}, \sigma_{21}, \sigma_{11}u + \sigma_{12}v]^T, \quad \mathbf{F}_y^v = -[\sigma_{12}, \sigma_{22}, \sigma_{21}u + \sigma_{22}v]^T. \quad (137)$$

3.6.1 Explicit Viscosity

The explicit update for the viscous fluxes is carried out on the main using again the RKDG method where the components of the spatial operator $\mathbf{L}_h(\widehat{\mathbf{Q}})$ are simply computed as follows

$$\begin{aligned} \mathbf{L}_h^x(\widehat{\mathbf{Q}})|_{T_i} &= -\frac{\Delta t}{\Delta x \Delta y} (\mathbf{M}^{xy})^{-1} \left(\int_{\partial T_{i,j}} \boldsymbol{\phi} \mathbf{F}_x^e \cdot \mathbf{n} dS - \int_{T_{i,j}} \nabla \boldsymbol{\phi} \cdot \mathbf{F}_x^e dx dy \right) \quad \text{with } \mathbf{F}_x^e = \mathbf{F}_x^c + \mathbf{F}_x^v, \\ \end{aligned} \quad (138)$$

$$\begin{aligned} \mathbf{L}_h^y(\widehat{\mathbf{Q}})|_{T_i} &= -\frac{\Delta t}{\Delta x \Delta y} (\mathbf{M}^{xy})^{-1} \left(\int_{\partial T_{i,j}} \boldsymbol{\phi} \mathbf{F}_y^e \cdot \mathbf{n} dS - \int_{T_{i,j}} \nabla \boldsymbol{\phi} \cdot \mathbf{F}_y^e dx dy \right) \quad \text{with } \mathbf{F}_y^e = \mathbf{F}_y^c + \mathbf{F}_y^v. \\ \end{aligned} \quad (139)$$

The numerical flux is computed using the method of Gassner et al. [47]

$$\begin{aligned} \mathbf{F}^e \cdot \mathbf{n} &= \frac{1}{2}(\mathbf{F}^e(q^+) + \mathbf{F}^e(q^-)) \cdot \mathbf{n} - \frac{1}{2}S_{max}^v(\mathbf{q}^+ - \mathbf{q}^-), \\ \text{with } S_{max}^v &= S_{max} + \frac{4}{3}\frac{\mu}{\rho} \frac{2P+1}{\Delta x_q} \quad \Delta x_q = \Delta x, \Delta y \end{aligned} \quad (140)$$

where S_{max} is the maximum speed of the convective terms computed according to the Rusanov method (see Eq. (76) discussed for the Euler equations. For this explicit scheme the time step restriction reads as follow

$$\begin{aligned} \Delta t &= \text{CFL} \left[(2P+1) \left(\frac{|u_{max}|}{\Delta x} + \frac{|v_{max}|}{\Delta y} \right) + \frac{4}{3} \frac{\mu}{\rho_{min}} (2P+1)^2 \left(\frac{1}{\Delta x^2} + \frac{1}{\Delta y^2} \right) \right]^{-1}, \\ \text{with } \text{CFL} &< 1. \end{aligned} \quad (141)$$

and it is more severe than the CFL condition for the Euler equations (see Sect. 3.2.2) due to the contribution of the parabolic viscous terms. For this reason an implicit treatment of the viscous terms would be a more efficient strategy, especially for high values of the viscosity and for very fine meshes.

3.6.2 Implicit Viscosity

For this algorithm the convective subsystem is updated using the RKDG method presented in Sect. 3.2.1 and this solution is denoted as $\widehat{\mathbf{FQ}} = [\widehat{\mathbf{F}\rho}, \widehat{\mathbf{F}\rho\mathbf{u}}, \widehat{\mathbf{F}\rho\mathbf{v}}, \widehat{\mathbf{F}\rho\mathbf{E}}]$. Then, we solve the following system of PDEs in order find the components of the velocity $\widehat{\mathbf{u}}^*$ and $\widehat{\mathbf{v}}^*$

$$\frac{d\rho u}{dt} = +\frac{4}{3}\mu\frac{\partial^2 u}{\partial x^2} + \mu\frac{\partial^2 u}{\partial y^2} + \frac{1}{3}\mu\frac{\partial^2 v}{\partial x\partial y} \quad (142)$$

$$\frac{d\rho v}{dt} = +\mu\frac{\partial^2 v}{\partial x^2} + \frac{4}{3}\mu\frac{\partial^2 v}{\partial y^2} + \frac{1}{3}\mu\frac{\partial^2 u}{\partial x\partial y} \quad (143)$$

where $\frac{d}{dt}$ are the total derivatives which account for the convective terms. Following the approach used in section and in [44] the spatial derivatives are integrated using a staggered DG method yielding the following system of equations

$$\begin{aligned} (\mathbb{M}\widehat{\rho}^* + \frac{4}{3}\mu\mathbb{H}^{xx} + \mu\mathbb{H}^{yy}) \cdot \widehat{\mathbf{u}}^* + \frac{1}{3}\mu\mathbb{H}^{xy} \cdot \widehat{\mathbf{v}}^* &= \widehat{\mathbf{F}\rho\mathbf{u}} \\ \frac{1}{3}\mu\mathbb{H}^{yx} \cdot \widehat{\mathbf{u}}^* + (\mathbb{M}\widehat{\rho}^* + \mu\mathbb{H}^{xx} + \frac{4}{3}\mu\mathbb{H}^{yy}) \cdot \widehat{\mathbf{v}}^* &= \widehat{\mathbf{F}\rho\mathbf{v}} \end{aligned} \quad (144)$$

which is solved by a conjugate gradient algorithm. Note that $\widehat{\rho}^* = \widehat{\mathbf{F}\rho}$. Once the velocities $\widehat{\mathbf{u}}^*$ and $\widehat{\mathbf{v}}^*$ are known it is possible to update the two components of the momentum as $\widehat{\rho\mathbf{u}}^* = \widehat{\rho}^*\widehat{\mathbf{u}}^*$ and $\widehat{\rho\mathbf{v}}^* = \widehat{\rho}^*\widehat{\mathbf{v}}^*$ and solve the energy equation

$$\frac{d\rho E}{dt} = \frac{\partial}{\partial x}(\sigma_{11}u + \sigma_{12}v) + \frac{\partial}{\partial y}(\sigma_{21}u + \sigma_{22}v) \quad (145)$$

using a classical explicit discontinuous Galerkin algorithm. Now the effect of the viscosity is included in the quantities $\widehat{\rho\mathbf{u}}^*$, $\widehat{\rho\mathbf{v}}^*$, $\widehat{\rho\mathbf{E}}^*$ and the numerical solution of the Navier–Stokes system of PDEs is completed by using the semi-implicit integration of pressure subsystem following the procedure given in Sect. 3.2.2. For this approach the stability condition for the computation of the time step is given by

$$\Delta t = \text{CFL} \left[(2P+1) \left(\frac{|u_{\max}|}{\Delta x} + \frac{|v_{\max}|}{\Delta y} \right) \right]^{-1}, \quad \text{with } \text{CFL} < 1. \quad (146)$$

which is the same of the semi-implicit DG method for the Euler equations.

4 Numerical Tests for the One-Dimensional Method

In this section we simulate several test cases in order to validate the new staggered semi-implicit discontinuous Galerkin method presented in Sect. 2 and referred to as SIDG in the following. The aim of the first test, which is reported in Sect. 4.1, is to verify the correctness of the implementation of the high order unlimited DG scheme. Then, in Sect. 4.2 the numerical results are compared against the exact solution of the Riemann problem in order to check the robustness of the limiter in presence of discontinuities. We remind that in all the benchmarks we do neither use artificial viscosity nor any smoothing or filtering of the solution. All numerical solutions are displayed on the figures as a set of equidistant samples in the DG cell by evaluating the underlying DG polynomial. More precisely $P+1$ sample points are displayed in 1D for a \mathbb{P}_P DG polynomial. For a FV subcell one sample centered point is plotted. Moreover each troubled DG cell and its $2P+1$ FV subcells, are colored in red, while unlimited DG cells are either plotted in blue or in black. When available, the numerical results are compared to an exact solution.

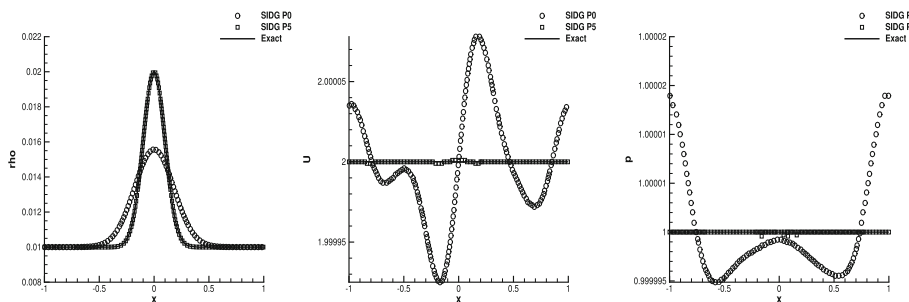


Fig. 12 Reference and numerical solutions for the Advection of a smooth density wave in 1D problem at $t_{end} = 1$

4.1 Advection of a Smooth Density Wave in 1D

Here, we consider a sanity test used to validate the correctness of the formulation of the pure DG scheme derived in Sect. 2.2. As initial condition, in the computational domain $\Omega_x = [-1, +1]$ we impose a smooth Gaussian profile for the density

$$\rho(x, 0) = \rho_0 \left(1 + e^{-\frac{0.5x^2}{0.1^2}} \right) \quad (147)$$

with $\rho_0 = 0.01$ and a constant value for the velocity $u(x, 0) = u_0 = 2$ and for the pressure $p(x, 0) = p_0 = 1$. Consequently, the density wave is transported without deformation. If we prescribe periodic boundary conditions, the exact solution at the final time $t_{end} = 1$ coincides with the initial condition. Two simulations are performed: first with a grid made of 50 cells with a polynomial degree $P = 5$ while, in the second case with 300 control volumes and $P = 0$ corresponding to a low order finite volume scheme. Note that in both cases the degrees of freedom are equal to 300. The implicitness parameter θ is fixed equal to 0.55. The results for density, velocity and pressure are presented in Fig. 12. It is possible to observe, that for this smooth test the results obtained using the high order semi-implicit DG scheme are extremely accurate and they reach an excellent agreement with the analytical solution. On the contrary, for the finite volume case we notice that the numerical solution for the density is drastically diffused. In addition, in the plots for the velocity and for the pressure, the numerical noise of the FV method is several orders of magnitude bigger than the noise produced by the DG scheme with $P = 5$.

4.2 One-Dimensional Riemann Problems

Here we apply the novel semi-implicit DG scheme to a set of Riemann problems taken from [36, 79, 82]. These simulations are carried out in order to check the correct propagation of the shock waves and to verify that the new method does not produce spurious or dispersive oscillations in the vicinity of discontinuities.

The computational domain is $\Omega_x = [-0.5, +0.5]$ and the initial condition consists in a discontinuity centred in x_0

$$\mathbf{V}(x, 0) = \begin{cases} \mathbf{V}_L & \text{if } x \leq x_0, \\ \mathbf{V}_R & \text{if } x > x_0. \end{cases} \quad (148)$$

In addition the simulation run up to $t = t_{end}$. The parameters for the initial conditions are listed in Table 1 and the results are shown in Figs. 14, 15, 16, 17, 18, 19 and 20 respectively. In RP0 we consider a contact discontinuity in the density moving in a flow characterized by uniform velocity and pressure. The results are shown in Fig. 13. It is possible to observe that the effects of numerical viscosity are located on the discontinuity. In this zone we also see that the limiter is active. Moreover, velocity and pressure remain constant. RP1 (see Fig. 14) is known as Sod shock tube [73]. We observe an excellent

Table 1 Initial and scheme conditions for the Riemann problems for semi-implicit DG schemes on staggered grid with subcell limiter—left and right states for ρ, U and p , initial discontinuity location x_0 , number of control volumes N_x , cell size Δx and final time of the simulations t_{end}

Case	ρ_L	u_L	p_L	ρ_R	u_R	p_R	P	x_0	N_x	Δx	t_{end}
RP0	10^5	1.0	10^5	10^{-3}	1	10^5	2	-0.25	200	0.05	0.5
RP1	1.0	0.0	1.0	0.125	0.0	0.1	5	0.0	100	0.01	0.2
RP2	0.445	0.698	3.528	0.5	0.0	0.571	5	0.0	100	0.01	0.14
RP3	1.0	0.0	1000.0	1.0	0.0	0.01	5	0.1	100	0.01	0.012
RP4	5.99924	19.5975	460.894	5.99924	-6.19633	46.095	5	0.0	100	0.01	0.035
RP5	1.0	-1.0	0.4	1.0	+1.0	0.4	5	0.0	100	0.01	0.15
RP6	1.0	+2.0	0.1	1.0	-2.0	0.1	5	0.0	100	0.01	0.5
RP7	1.0	0.75	1.0	0.125	0.0	0.1	5	-0.1	100	0.01	0.2

agreement with the reference solution and, moreover, the limiter is activated in the region of the shock wave only, while the rarefaction and the contact waves are solved only by using the pure DG method.

RP2 (see Fig. 15) is called Lax problem [62]. Also here we see a good fit with the exact solution. The new staggered semi-implicit DG scheme activates the *a posteriori* subcell FV limiter appropriately only at the shock wave.

RP3 and RP4 (see Figs. 16 and 17) are taken from the well-known textbook of Toro [82]; these test cases involve strong shock waves and consequently they are suitable for checking the robustness of the scheme. In RP3 despite a small overshoot on the shock wave, in the other parts of the domain the agreement is excellent. Also in RP4 (see Fig. 17) the shocks are very well resolved but we observe some additional troubled cells, probably because of some numerical noise in the plateau region.

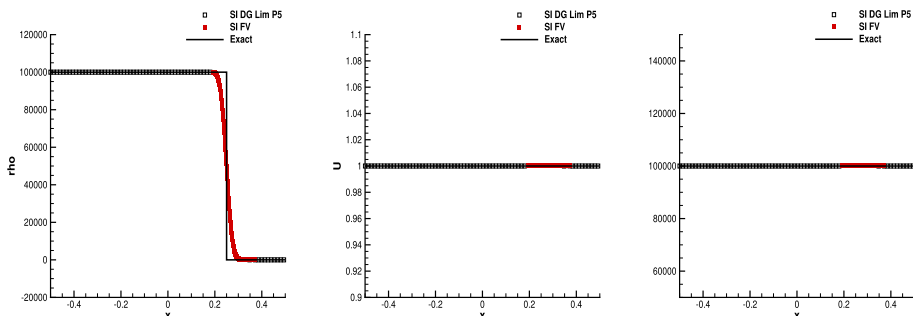
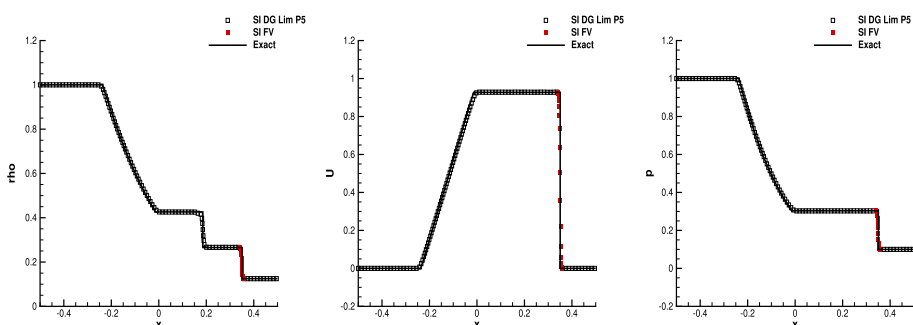
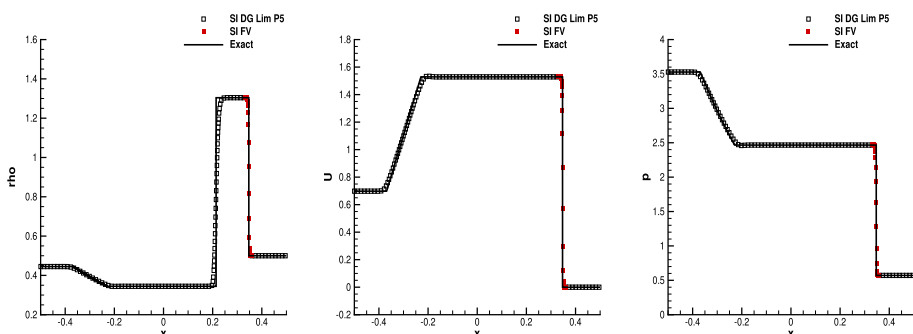
RP5 (see Fig. 18) consists of two symmetric rarefaction waves. We notice a small spurious peak close to the origin but elsewhere the numerical solution agrees with the exact one. Moreover, troubled cells are detected only in the first part of the simulation because the initial condition is discontinuous.

In RP6 (see Fig. 19) two jets collide and a double shock is generated; we observe that the waves are perfectly symmetric and the troubled cell are optimally detected and solved without occurrence of any Gibbs phenomena. Note that the glitch in the density has been observed also in [36].

RP7 (see Fig. 20) is a modified Sod problem proposed by Toro in [82] and is used to verify the presence of an entropy glitch inside the left moving rarefaction, sometimes observed in some entropy-violating approximate Riemann solvers [71]. Again, the agreement is good and we can conclude that the semi-implicit finite volume subcell limiter applied to the staggered semi-implicit DG scheme is an appropriate shock capturing strategy. Moreover, our numerical experiments have shown that the use of the limiter was necessary for all these test cases in order to successfully reach the final time t_{end} . The unlimited DG scheme alone produces strong spurious oscillations in the vicinity of discontinuities that may lead to negative densities and pressures, which then make the code crash. Contrarily, our *a posteriori* subcell finite volume limiter successfully cures these spurious oscillations and renders the code at the same time robust and accurate on these demanding test cases.

4.3 Comparison Against Other Schemes in One Dimension

In this subsection we compare the novel staggered semi-implicit DG 1D against other classical one-dimensional explicit methods on collocated grids. We consider benchmarks characterized by low Mach number according to the motivation presented at the beginning of the paper. At first, we consider a smooth test case and we repeat the problem carried out in Sect. 4.1 with some small modifications. The velocity and the pressure are chosen as $u_0 = 1$ and $p_0 = 1$. The polynomial degree is $P = 4$ and the cells used are $N_x = 30$. The Gaussian bell is centered in $x_0 = -0.5$, $dt_0 = 10^{-3}$ and the final

Fig. 13 RP0: reference and numerical solutions for ρ , u and p at $t_{end} = 0.5$ Fig. 14 RP1: reference and numerical solutions for ρ , u and p at $t_{end} = 0.2$ Fig. 15 RP2: reference and numerical solutions for ρ , u and p at $t_{end} = 0.14$

time is $t_{end} = 1$; the other parameters are the same used in Sect. 4.1. We consider two simulations, one is performed using the 1D staggered unlimited semi-implicit DG proposed in this paper and the second is performed with the explicit Runge Kutta Discontinuous Galerkin method ([25]). The results are shown in Fig. 21 (left column) and from the second and third columns of Table 2 it is possible to conclude that for smooth solutions in the low Mach regime the novel semi-implicit DG on staggered meshes gives more accurate results than the explicit RKDG method involving less time steps and a smaller CPU time. Later on, we consider a discontinuous test case at low Mach number. The initial condition is a density jump with the discontinuity centred in $x_0 = 0.4$. The left and the right density states are $\rho_L = 10$ and $\rho_R = 0.1$ while the velocity and the pressure are constant and equal to 1 and to 10^4 respectively. The computational domain is $\Omega_x = [0, 1]$ and the final time of the simulation is

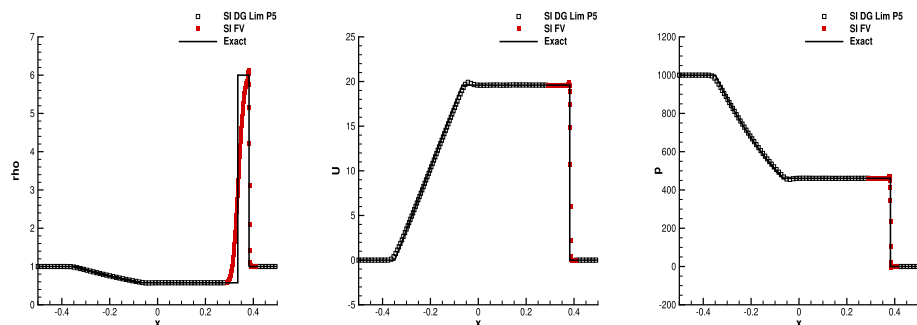


Fig. 16 RP3: reference and numerical solutions for ρ , u and p at $t_{end} = 0.012$

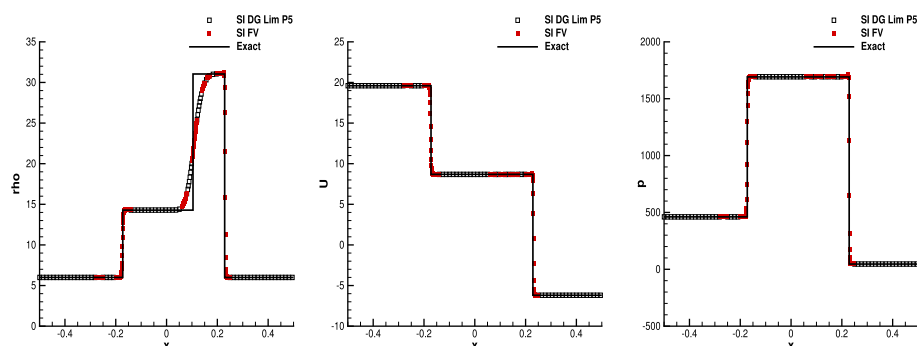


Fig. 17 RP4: reference and numerical solutions for ρ , u and p at $t_{end} = 0.035$

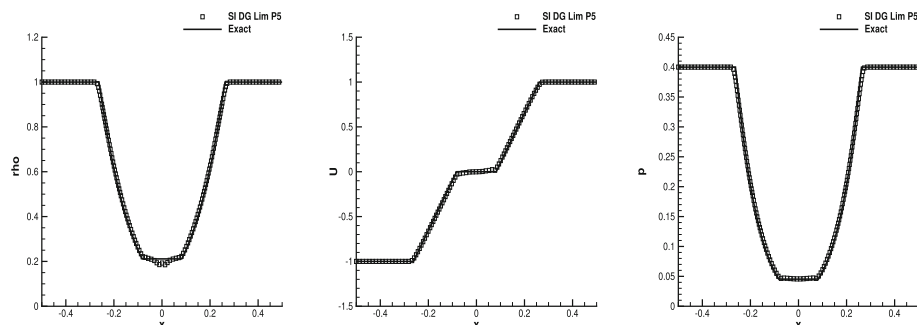


Fig. 18 RP5: reference and numerical solutions for ρ , u and p at $t_{end} = 0.15$

$t_{end} = 0.1$. For this benchmark the new limiting strategy is crucial and the grid is composed by 100 cells with $P = 4$ for a total number of degrees of freedom equal to 500. The other scheme considered is the explicit WENO5 finite volume method of Jiang and Shu [57] with 500 elements. The results are plotted in Fig. 21 (right column) and the efficiency analysis is in Table 2. Also in this case, it is possible to state the same conclusions obtained for the smooth case. In fact, for this test case the WENO5 scheme gives more viscous results than the semi-implicit DG using much more time steps and higher computational time.

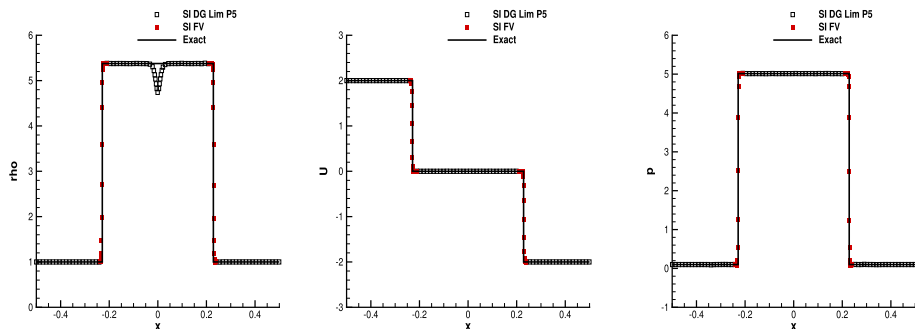


Fig. 19 RP6: reference and numerical solutions for ρ , u and p at $t_{end} = 0.5$

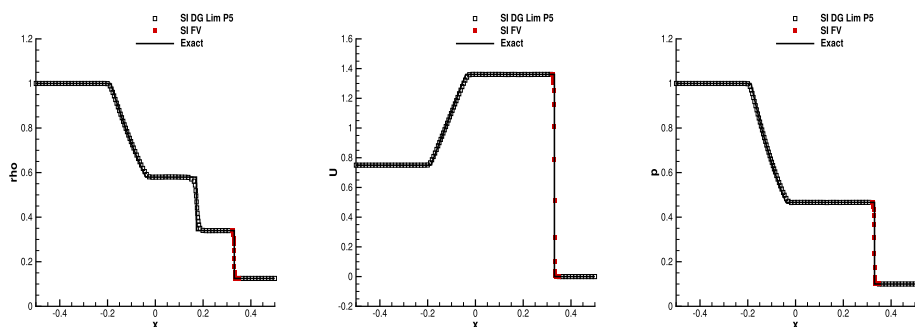


Fig. 20 RP7: reference and numerical solutions for ρ , u and p at $t_{end} = 0.2$

Table 2 Table for the efficiency analysis in 1D

	Smooth advection problem		Discontinuous advection problem	
	Semi-implicit	Explicit RKDG	Semi-implicit	Explicit WENO5
Iterations	1000	3851	1000	20,850
L_2 error	3.1076e-8	3.9086E-8	4.89531E-1	5.0997E-1
CPU time (sec)	149	348	81	141

Temporal iteration, L_2 error and CPU time for the smooth advection problem and for the discontinuous advection considering the novel staggered semi-implicit DG, Runge Kutta DG and WENO5 FV method

5 Numerical Tests for the Two-Dimensional Method

Finally, we carry out the numerical validation of the two-dimensional semi-implicit staggered DG scheme with *a posteriori* subcell finite volume limiting. First we consider two smooth problems: in Sect. 5.1 we compute the convergence table and the numerical order of convergence of the 2D scheme; then the test case in Sect. 5.2 can be considered as a sanity check analogous to the one of Sect. 4.1, while, in Sect. 5.3, some low Mach number regime simulations are run. We conclude this test suite with the 2D Riemann problems in Sect. 5.5 where the use of the limiter is fundamental in order to complete the simulations, and, obtain a clean, robust and accurate solution of the PDEs. All computations were carried out on *one single CPU core* of a workstation with an Intel i7-4790 CPU with 3.6 GHz clock speed and 32 GB of RAM.

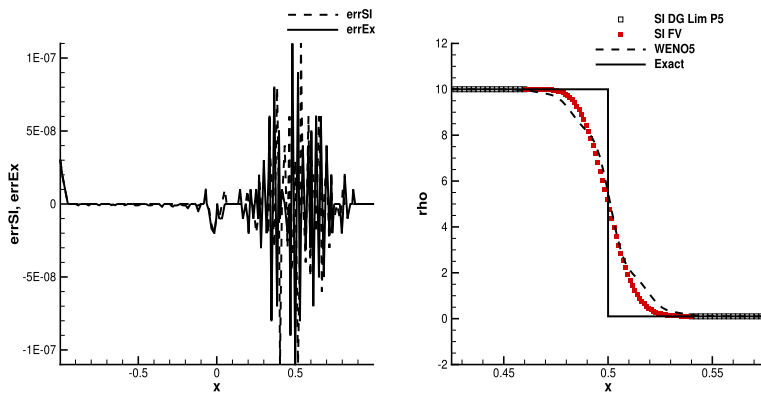


Fig. 21 Advection test problems and comparison between explicit and semi-implicit schemes. Density error in the advection of a smooth Gaussian density profile (left). Moving contact discontinuity (right)

Table 3 Shu–Osher vortex—numerical convergence rates computed with respect to the L_2 error norms of the pressure and velocity for the two-dimensional semi-implicit staggered DG scheme

P	$N_x = N_y$	$\epsilon_{L_2}^P$	$\epsilon_{L_2}^{V_t}$	$O_{L_2}^P$	$O_{L_2}^{V_t}$
0	100	1.94E-2	3.90E-2	—	—
	200	9.69E-3	1.71E-2	0.99	1.18
	300	6.58E-3	1.10E-2	0.95	1.09
	400	4.99E-3	8.10E-3	0.95	1.06
1	100	2.44E-2	3.14E-3	—	—
	200	1.25E-2	9.83E-4	0.96	1.67
	300	8.40E-3	4.64E-4	0.98	1.85
	350	7.21E-3	3.52E-4	0.99	1.77
	400	6.32E-3	2.77E-4	0.99	1.80
2	50	3.43E-3	1.67E-3	—	—
	100	6.31E-4	2.76E-4	2.44	2.59
	150	1.79E-4	9.03E-5	3.10	2.75
	200	7.69E-5	3.88E-5	2.93	2.93
3	25	8.89E-4	2.90E-4	—	—
	50	1.14E-4	2.49E-5	2.96	3.53
	75	3.35E-5	6.36E-6	3.02	3.36
	100	1.41E-5	2.51E-6	3.01	3.23
4	15	9.82E-4	3.42E-4	—	—
	30	7.67E-5	2.14E-5	3.67	4.00
	45	1.73E-5	3.04E-6	3.66	4.86
	60	5.58E-6	1.03E-6	3.93	3.75
5	15	8.39E-4	3.35E-4	—	—
	30	4.97E-5	5.27E-6	4.07	5.98
	45	7.02E-6	5.89E-7	4.82	5.40
	60	1.46E-6	2.85E-7	5.44	2.52

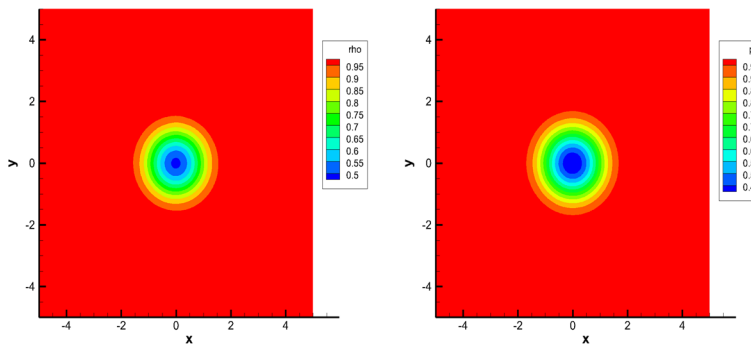


Fig. 22 Shu–Osher vortex—Contour plots for the density and the pressure at time $t_{end} = 10$

5.1 Isentropic Vortex

The first two-dimensional test is the well known *isentropic vortex* (see [53]). For the 2D Euler equations, this is a fundamental benchmark because this test checks the correctness of the implementation and the numerical convergence. In addition, the boundary conditions can be either set to periodic or transmissive. The initial condition for the density and for the pressure are $\rho(x, y, 0) = \rho_\infty + \delta\rho$, $p(x, y, 0) = p_\infty + \delta p$, where $\delta\rho$ and δp read as follows

$$\delta\rho = (1 + \delta T)^{\frac{1}{\gamma-1}} - 1, \quad \delta p = (1 + \delta T)^{\frac{\gamma}{\gamma-1}} - 1, \quad \text{with } \delta T = \frac{(\gamma - 1)\beta^2}{8\gamma\pi^2} e^{1-r^2}, \quad (149)$$

where we have introduced the radial coordinate $r = \sqrt{(x - x_0)^2 + (y - y_0)^2}$, the vortex center $(x_0, y_0) = (0, 0)$, $[\rho_\infty, p_\infty] = [1, 1]$ and, β , the vortex strength, here imposed equal to 5. The initial velocity is $[u(x, y, 0), v(x, y, 0)] = [u_\infty + \delta u, v_\infty + \delta v]$ where δu and δv are given as

$$\delta u = -\frac{\beta}{2\pi} e^{\frac{1-r^2}{2}} (y - y_0), \quad \delta v = \frac{\beta}{2\pi} e^{\frac{1-r^2}{2}} (x - x_0). \quad (150)$$

If the undisturbed velocity components u_∞ and v_∞ are imposed equal to 0, then the vortex is stationary. In this particular case we computed the L_2 error between the numerical and the exact solutions on a series of successively refined grids characterized by square cells in a domain $\Omega_{xy} = [-5, +5] \times [-5, +5]$ with $N_x = N_y$. For this steady state test, the choice of $\theta = 1$ makes sense because the problem is stationary (Table 3). The results for the errors and for the convergence rates are reported in the following table and it is possible to state that the semi-implicit DG method on staggered meshes is indeed arbitrary high order accurate in space, see also [35] for the shallow water equations. In particular for a given polynomial degree P , we observe that the convergence rate is equal to $P + 1$ for the absolute value of the velocity ($V = \sqrt{u^2 + v^2}$). For the pressure, an optimal convergence rate is reported for P even while sub-optimal for P odd. We attribute this behaviour to the choice of the basis functions; more detailed analyses will be carried out in the future. In addition, it is possible to note that for the last meshes used for $P = 4$ and $P = 5$ the order of convergence is lost because the errors generated by the numerical method are too low and affected by roundoff errors.

Later on, we impose the components of the velocity $[u_\infty, v_\infty]$ equal to $[1, 1]$. The computational grid is composed of 625 square cells with $N_x = N_y = 25$, the degree of the polynomial basis functions is $P = 5$ and $\Omega_{xy} = [-5, +5] \times [-5, +5]$. We impose the implicitness parameter equal to $\theta = 0.7$ and periodic boundary conditions are prescribed. Hence, at the final time $t_{end} = 10$ the vortex is centred again at its initial position at $(x_0, y_0) = (0, 0)$ and the exact solution corresponds to the initial one (see (149) and (150)). In Fig. 22 we report the contour plots for the density and pressure where it can be observed that the numerical solution is symmetric and free from spurious oscillations.

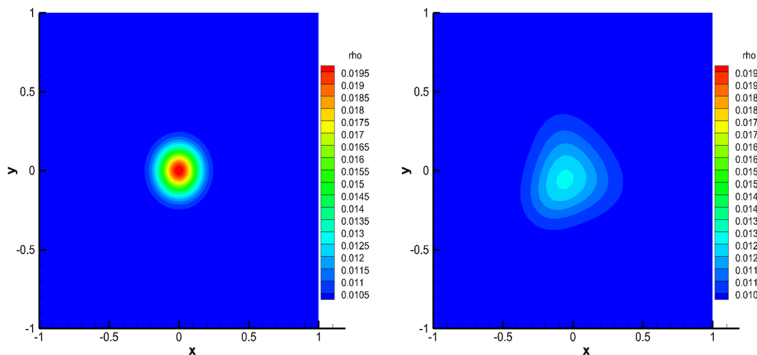


Fig. 23 Advection of a smooth density bell in 2D—density for $P = 5$ (high order DG) and for $P = 0$ (first order FV) at time $t_{end} = 2$

5.2 Advection of a Smooth Density Bell in 2D

Similarly to the 1D method in Sect. 4.1, this test consists in a two dimensional smooth Gaussian bell moving in a uniform pressure and velocity flow. Hence the initial condition reads as follows

$$\rho(x, y, 0) = \rho_0 \left(1 + e^{-\frac{0.5r^2}{0.1^2}} \right), \quad p(x, y, 0) = 1, \quad u(x, y, 0) = v(x, y, 0) = 1, \quad (151)$$

with $\rho_0 = 0.02$, so that the Mach number is of the order $M = 0.1$. The computational domain is $\Omega_{xy} = [-1, +1] \times [-1, +1]$ and $t_{end} = 2$; consequently, when imposing periodic boundary conditions the reference solution at the final time coincides with the initial condition in (151). We consider two configurations both with $\theta = 0.55$; in the first one the polynomial degree is $P = 5$ and $N_x = N_y = 50$ and for the second case $N_x = N_y = 300$ using $P = 0$, which corresponds to the piece-wise constant finite volume data. Note that in both situations the number of degrees of freedom is the same and equal to $N_x \times N_y \times P^2 = 9 \times 10^4$. The results for the contour plot at time $t_{end} = 2$ are shown in Fig. 23. Here we observe that for the high order DG case the solution is centred and symmetric, while we can see the spurious effects of the numerical viscosity in the first order situation. Moreover, in Fig. 24, we report a comparison between the numerical and the exact solutions both for a slice along the x axis. Similarly to the 1D case in Sect. 4.1, in the FV case the dissipation is important while the semi-implicit staggered DG scheme produces a very accurate solution. Consequently, this underlines the importance of the high order approach for the numerical solution of nonlinear partial differential equations. This benchmark problem terminated after 2446 time steps for a CPU time equal to 681 s and a L_2 error norm in the density equal to $2.443 \cdot 10^{-4}$. In addition, we repeated the simulation using an explicit third order RKDG scheme which involved 31369 time steps, for a CPU time equal to 2274 seconds and L_2 error norm in the density equal to $1.2787 \cdot 10^{-4}$.

5.3 Two-Dimensional Smooth Acoustic Wave Propagation

Let us consider another smooth test for the two-dimensional Euler equations. The initial pressure is a smooth surface, $p(x, y, 0) = 1 + e^{-\alpha r^2}$, while the density is constant, $\rho(x, y, 0) = 1$, and both components of velocity are null, $u(x, y, 0) = 0, v(x, y, 0) = 0$. For this test $\alpha = 40$ and $r = \sqrt{x^2 + y^2}$ is the radial coordinate. This simulation is characterized by a cylindrically symmetric solution. For this benchmark, the magnitude of the Mach number is 0.1.

According to [79], this is a useful test in order to assess the performance of high order staggered semi-implicit schemes for the 2D Euler equations. For this simulation the computational domain is $\Omega_{xy} = [-2, +2] \times [-2, +2]$ and we use $N_x = N_y = 50$ with a total number of 2500 cells, using a

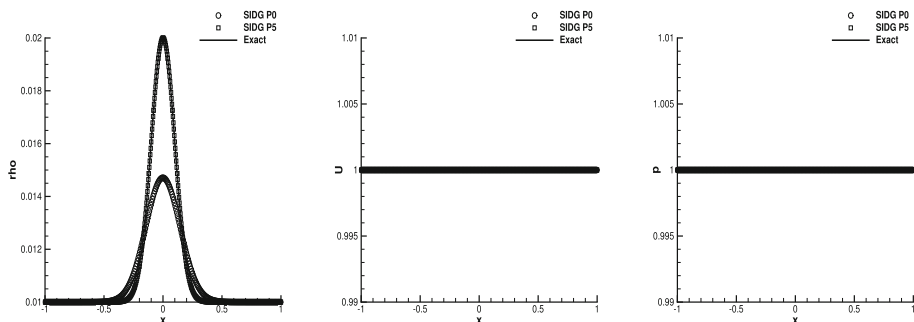


Fig. 24 Advection of a smooth density bell in 2D—reference and numerical solutions along the x axis for ρ , velocity component u and p at time $t_{end} = 2$

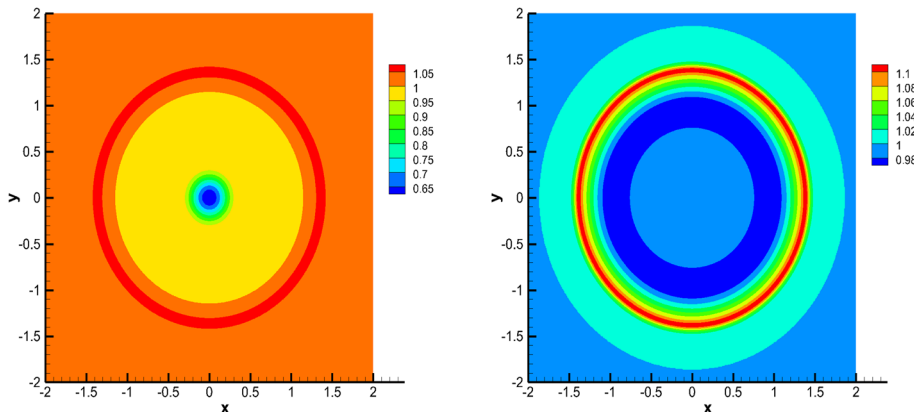


Fig. 25 Two-dimensional smooth acoustic wave propagation—contour plots for the density and pressure at time $t_{end} = 1$

polynomial degree $P = 5$. Hence, the total number of degrees of freedom is 90000 and the final time is set to $t = 1$. The implicitness parameter θ is chosen equal to 0.55 in order to get as close as possible to the second order accurate Crank-Nicholson scheme in time.

In Fig. 25 we can observe that the color contour plots for the density and the pressure perfectly respect the cylindrical symmetry. In addition, in Fig. 26 we compare the numerical results against a reference solution obtained running a second order explicit TVD scheme for an equivalent 1D PDE system with geometric source terms, see [82], on a very fine mesh. Except for some slight numerical dissipation close to the peaks, the agreement is excellent and the acoustic waves travel with the proper speed. Similar to the observations made in [79], we can state that the semi-implicit staggered DG scheme is a suitable numerical method for CFD simulations in the low Mach number regime. This simulation executed with the novel semi-implicit staggered DG scheme terminated after 109 time steps and 36 seconds, while the same problem solved by a third order explicit RKDG required 938 time steps and 75 seconds of wall-clock time. For this test we do not have an exact reference solution in 2D. However, the explicit RKDG is slightly less diffusive than the semi-implicit scheme but this explicit method produces dispersive oscillations where the gradients become very high (see Fig. 27).

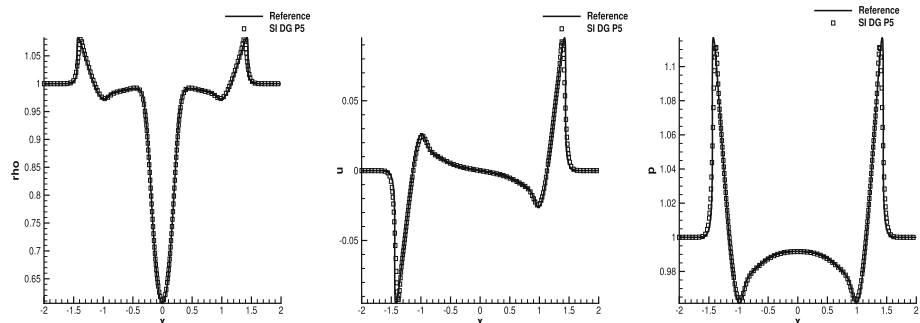
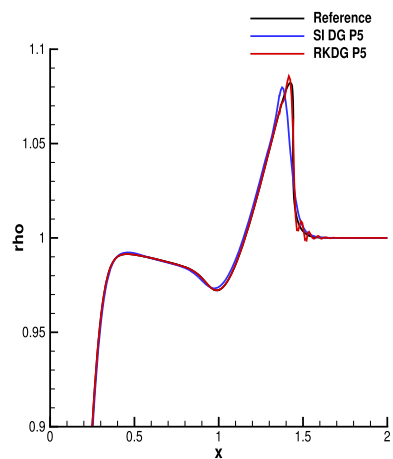


Fig. 26 Two-dimensional smooth acoustic wave propagation—reference and numerical solutions along the x axis for ρ , u and p at time $t_{end} = 1$

Fig. 27 Two-dimensional smooth acoustic wave propagation—reference (black line) against numerical solutions for SI DG P5 (blue line) and RKDG P5 (red line) along the x axis for ρ , u and p at time $t_{end} = 1$ (Color figure online)



5.4 Circular Explosion

Here we consider a well known two dimensional Riemann problem characterized by a cylindrical symmetry. Given a computational domain $\Omega_{xy} = [-1, +1] \times [-1, +1]$ the initial condition reads

$$\mathbf{V}(x, y, 0) = \begin{cases} \mathbf{V}_{\text{in}} = [1, 0, 0, 1]^T & \text{if } r \leq r_c \\ \mathbf{V}_{\text{out}} = [0.125, 0, 0, 0.1]^T & \text{if } r > r_c. \end{cases} \quad (152)$$

where $r = \sqrt{x^2 + y^2}$ is the radial coordinate and $\mathbf{V} = [\rho, u, v, p]$ is vector of primitive variables. For this simulation we impose the polynomial degree P equal to 5 and we use $N_x = N_y = 100$ with $\theta_{DG} = 0.55$ and $t_{end} = 0.2$. In Fig. 28 we see that the density has a very clean contour plot. In addition we report a map of the troubled cells; most of them are located in the vicinity of the shock wave and few other control volumes are limited in the zone of the contact wave. We can observe that a vast majority of the cells are dealt with the unlimited optimal DG scheme, while few troubled cells demand a re-calculation. Moreover, a cut of the solution along the x axis is compared against the reference solution in Fig. 29. These last data are obtained using a robust second order TVD scheme (see [88]) on a fine grid solving an equivalent 1D Euler system of PDEs with a source term taking into account the effect of the radial symmetry [82]. We observe an excellent agreement between the solutions; furthermore in the numerical solution no oscillation is observed, and, all waves are solved with their correct speed of propagation.

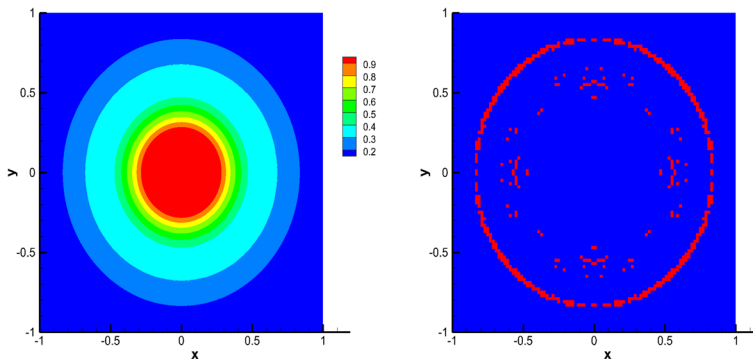


Fig. 28 Circular explosion—contour plots for the density and map of the troubled zones (red cells) at time $t_{end} = 0.2$ (Color figure online)

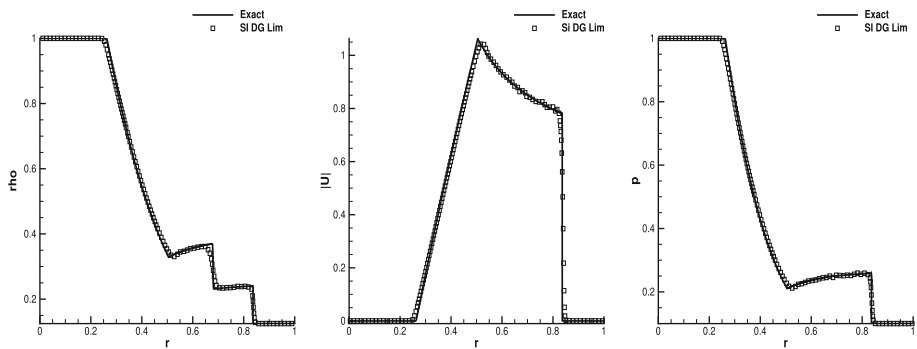


Fig. 29 Circular explosion—reference and cut-of the numerical solutions along the x axis for ρ , u and p at time $t_{end} = 0.2$

5.5 Two Dimensional Riemann Problems

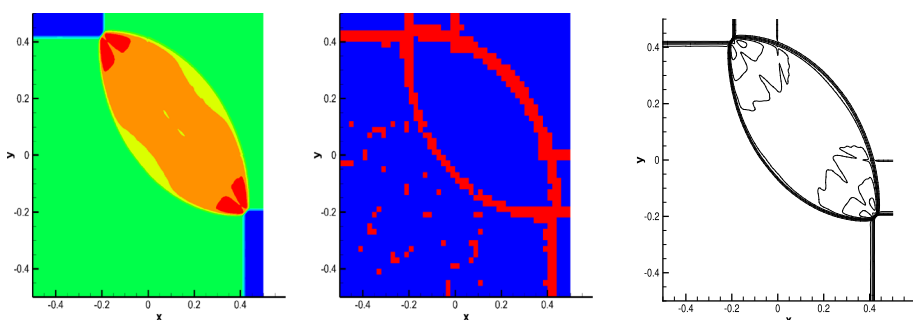
For the last benchmarks we consider a class of two dimensional Riemann problems presented in [72] and studied in detail in [61]. The computational domain $\Omega_{xy} = [-0.5, +0.5] \times [-0.5, +0.5]$ is paved using $N_x = N_y = 50$ cells with a polynomial degree $P = 5$. The initial condition reads as follows

$$(\rho, u, v, p) = \begin{cases} (\rho_1, u_1, v_1, p_1) & \text{if } x > 0 \wedge y > 0, \\ (\rho_2, u_2, v_2, p_2) & \text{if } x \leq 0 \wedge y > 0, \\ (\rho_3, u_3, v_3, p_3) & \text{if } x \leq 0 \wedge y \leq 0, \\ (\rho_4, u_4, v_4, p_4) & \text{if } x > 0 \wedge y \leq 0, \end{cases} \quad (153)$$

We consider four initial configurations, the same ones carried out in [36], the initial parameters of which are listed in Table 4. From Figs. 30, 31, 32, 33 we can state that the numerical result are in good agreement when compared to the simulations carried out in [36, 61]. In addition we observe that most of the troubled control volumes are located on the discontinuities but, probability due to numerical noise, few bad cells are also detected in the plateau regions and at boundaries. Moreover, since this method is at most second order accurate in time we observe a relevant numerical viscosity which, here, is clearly higher than the one observed in explicit DG schemes with *a posteriori* subcell WENO limiter, see [42, 90]. In order to achieve higher order in time, the present staggered semi-implicit DG scheme could be extended to a semi-implicit staggered space-time DG method, see [44, 77, 79].

Table 4 Initial conditions for the 2D Riemann problems

	ρ	u	v	p
Configuration C4				
($x > 0, y > 0$)	1.1	0.0	0.0	1.1
($x < 0, y > 0$)	0.5065	0.8939	0.0	0.35
($x < 0, y < 0$)	1.1	0.8939	0.8939	1.1
($x > 0, y < 0$)	0.5065	0.0	0.8939	0.35
Configuration C7				
($x > 0, y > 0$)	0.5197	-0.6259	0.1	0.4
($x < 0, y > 0$)	1.0	0.1	0.1	1.0
($x < 0, y < 0$)	0.8	0.1	0.1	0.4
($x > 0, y < 0$)	0.5197	0.1	-0.6259	0.4
Configuration C8				
($x > 0, y > 0$)	0.5197	0.1	0.1	0.4
($x < 0, y > 0$)	1.0	-0.6259	0.1	1.0
($x < 0, y < 0$)	0.8	0.1	0.1	1.0
($x > 0, y < 0$)	1.0	0.1	-0.6259	1.0
Configuration C16				
($x > 0, y > 0$)	0.5313	0.1	0.1	0.4
($x < 0, y > 0$)	1.0222	-0.6179	0.1	1.0
($x < 0, y < 0$)	0.8	0.1	0.1	1.0
($x > 0, y < 0$)	1.0	0.1	0.8276	1.0

**Fig. 30** Two dimensional Riemann problem RP2D C4—contour plots for the density, map of the troubled zones (red cells) and contour lines at time $t_{end} = 0.2$ (Color figure online)

5.6 Viscous Taylor–Green Vortex at Low Mach Number

Here, we solve a benchmark problem that is characterized by a nearly incompressible flow regime, which is the well known Taylor–Green vortex (see e.g. [8, 41, 44, 76]). The exact solution of the incompressible Navier–Stokes equations is given as follows:

$$\begin{aligned}\rho(x, y, t) &= \rho_0 \\ u(x, y, t) &= \sin(x) \cos(y) e^{-2vt},\end{aligned}$$

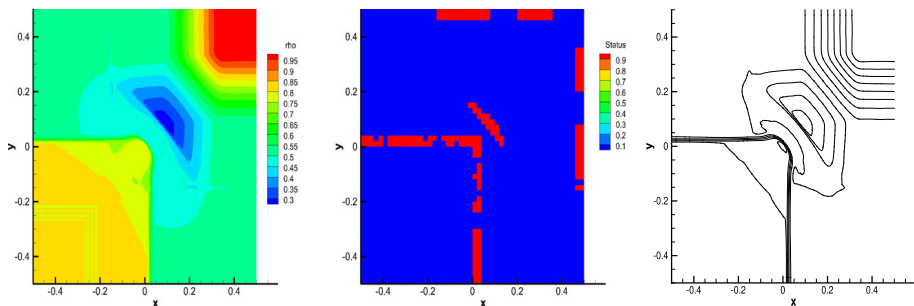


Fig. 31 Two dimensional Riemann problem RP2D C7—contour plots for the density, map of the troubled zones (red cells) and contour lines at time $t_{end} = 0.2$ (Color figure online)

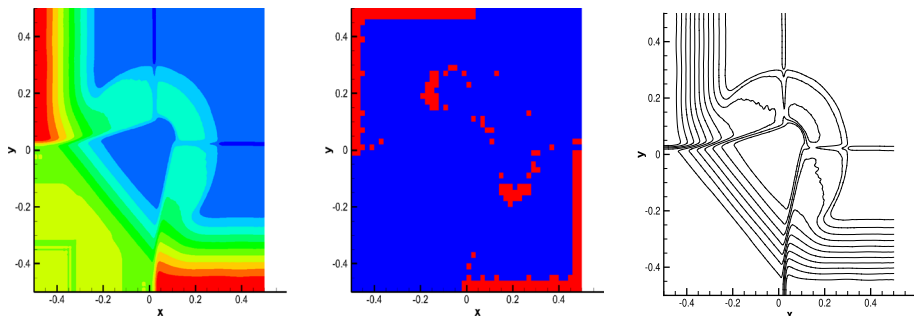


Fig. 32 Two dimensional Riemann problem RP2D C8—contour plots for the density, map of the troubled zones (red cells) and contour lines at time $t_{end} = 0.2$ (Color figure online)

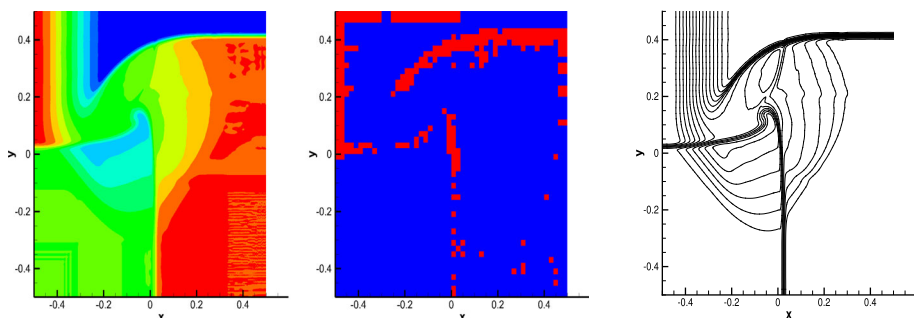


Fig. 33 Two dimensional Riemann problem RP2D C16—contour plots for the density, map of the troubled zones (red cells) and contour lines at time $t_{end} = 0.2$ (Color figure online)

$$\begin{aligned} v(x, y, t) &= -\cos(x) \sin(y) e^{-2vt}, \\ p(x, y, t) &= C + \frac{1}{4}(\cos(2x) + \sin(2y)) e^{-4vt}, \end{aligned} \quad (154)$$

with $\rho_0 = 1$, $C = 10^4$ and $\mu = 0.1$. The initial condition is given by Eq. (154) using $t = 0$ and the simulation is carried out using the implicit time integration of the viscous terms because the viscosity is very high. With this choice of parameters, the Mach number of this test case is of the order $M \approx 10^{-2}$, i.e. the use of an *explicit* scheme would be computationally very inefficient due to the CFL condition on the time step based on the sound speed and due to the effects of the parabolic terms. On the contrary,

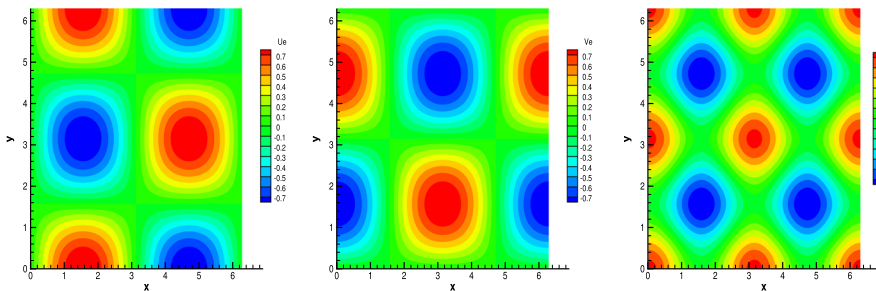


Fig. 34 Taylor–Green vortex—contour plots for u , v and p at time $t_{end} = 1.0$

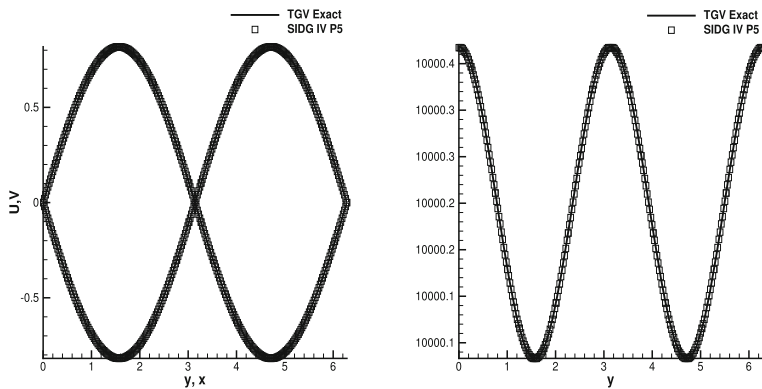


Fig. 35 Taylor–Green vortex—reference and cut-of the numerical solutions along the x axis for u , v and p at time $t_{end} = 1.0$

the time step of our semi-implicit staggered DG scheme with implicit viscosity is only limited by a CFL condition based on the flow velocity. We consider a computational domain $\Omega_{xy} = [0, 2\pi] \times [0, 2\pi]$ composed of 25^2 cells ($N_x = N_y = 25$) and a polynomial degree of $P = 5$. The final time of the simulation is $t_{end} = 1$. In Fig. 34 we report the contour plots for the components of the velocity and for the pressure and we can observe a very clean solution for all the quantities. In addition, in Fig. 35 we expose 1D cuts along the x and the y axis for the velocity components u and v and for the pressure p . For all quantities we note an excellent agreement between our numerical results and the reference solution. This simulation terminated after 181 time step with a CPU time of 168 s and a L_2 norm for the pressure equal to $5.7653e-3$. Later on, we repeated the simulation using a fully explicit time integration of the viscous term and we got the result after 2449 time steps and 195 s with a L_2 norm for the pressure equal to $1.0357e-3$. Notice that in this second case the error is smaller but the convection-diffusion is updated using a third order method in time. Hence, for high viscosities the implicit discretization of the source term is clearly more efficient than a explicit approach.

5.7 Double Shear Layer

Here we use again the extension of the SIDG scheme to the compressible Navier–Stokes equations exposed in Sect. 3.6, in order to carry out simulations for the double shear layer benchmark problem (see [6, 44, 77]). The computational domain is $\Omega_{xy} = [0, 1]^2$ with periodic boundary conditions everywhere.

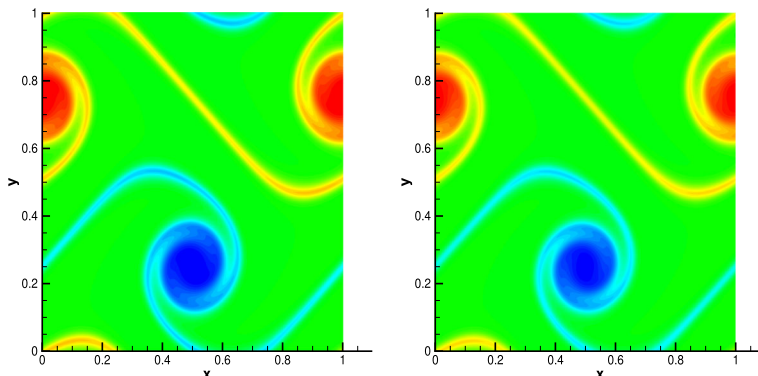


Fig. 36 Vorticity contours for the double shear layer problem at $t = 1.2$. Numerical solutions computed by the novel staggered semi-implicit DG method for the compressible Navier–Stokes (left) and by the spectral staggered semi-implicit DG for the incompressible Navier–Stokes of Fambri and Dumbser ([44])

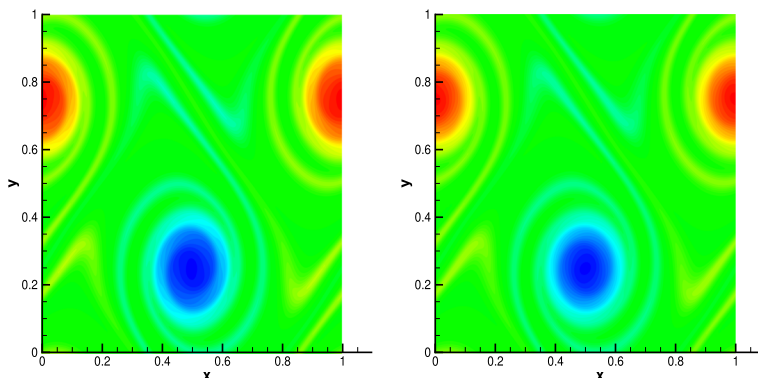


Fig. 37 Vorticity contours for the double shear layer problem at $t = 1.8$. Numerical solutions computed by the novel staggered semi-implicit DG method for the compressible Navier–Stokes (left) and by the spectral staggered semi-implicit DG for the incompressible Navier–Stokes of Fambri and Dumbser ([44])

The initial condition for the components of the velocities is

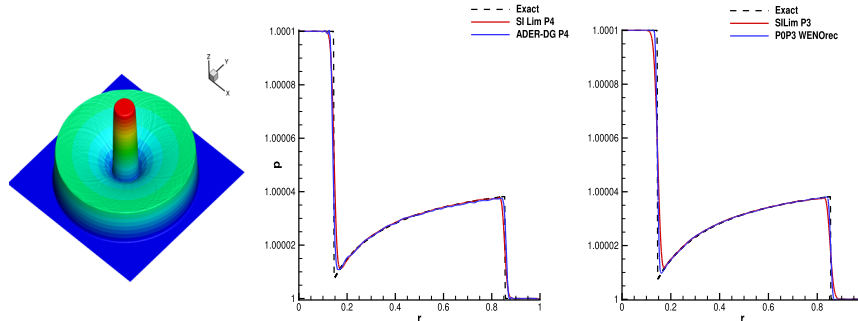
$$u = \begin{cases} \tanh(\bar{\rho}(y - 0.25)), & \text{if } y \leq 0.5 \\ \tanh(\bar{\rho}(0.75 - y)), & \text{if } y > 0.5 \end{cases} \quad v = \delta \sin(2\pi x) \quad \text{with} \quad \bar{\rho} = 30 \quad \delta = 0.05, \quad (155)$$

while we impose $\rho = 1$ and $p = 10^4$ in order to work in the low Mach number regime. The grid is composed by 30^2 cells ($N_x = N_y = 30$) with a polynomial degree $P = 5$ and $\mu = 2 \cdot 10^{-4}$. The implicitness parameter θ is equal to 0.55. The viscous parabolic terms are integrated with the implicit discretization, but one could choose also the explicit algorithm because in this benchmark the viscosity is quite small. In the Figs. 36 and 37 we report the contour plots for the vorticity at times $t = 1.2$ and $t = 1.8$. In these figures the novel results for the compressible Navier–Stokes (left column) are compared against the numerical solution of the incompressible Navier–Stokes (right column) computed with the spectral semi-implicit DG scheme of Fambri and Dumbser (see [44]) using exactly the same mesh and polynomial approximation degree. In conclusion, we observe a good agreement.

Table 5 Table for the efficiency analysis for the 2D method

	Steady Taylor Green vortex		Low Mach explosion		Low Mach explosion	
	RKDG P4	SI DG P4	ADERDG P4	SI DG P4	WENO4	SI DG P3
Time steps	16076	1000	1144	300	202	200
L2err	3.003E-3	1.4762e-3	—	—	—	—
CPU time (sec)	506	114	973	601	2656	325

Temporal iteration, L_2 error and CPU time for three different benchmark problems considering explicit schemes and semi-implicit DG method



(a) 3D plot of the pressure **(b)** SIDG 2D P4 Lim vs ADER-DG P4 **(c)** SIDG 2D P3 Lim vs P0P3 WENO rec

Fig. 38 Low Mach number explosion. Pressure and 1D cut along the x -axis

5.8 Comparison Against Other Schemes in 2D

Similarly to the 1D scheme, we analyse the behaviour in the low Mach number limit of the novel 2D staggered semi-implicit scheme against explicit schemes. We start investigating a steady Taylor Green Vortex which is the inviscid case of the benchmark presented in Sect. 5.6. We impose $\mu = 0$ and $P = 4$, while the other parameters do not change with respect Sect. 5.6. The test is executed using the novel staggered semi-implicit scheme and an explicit Runge-Kutta DG scheme. We observed that the novel 2D SI-DG method is more efficient than the classical explicit DG scheme, see Table 5.

Later on, we perform a low Mach number explosion test in order to compare the new limiter against other explicit methods in situations characterized by strong gradients. The domain is $\Omega = [-1, +1]^2$ and the initial data are given as follows:

$$\mathbf{V}(x, y, 0) = \begin{cases} \mathbf{V}_{\text{in}} = [10^{-2}, 0, 0, 1 + 10^{-4}] & \text{if } r \leq 0.5 \\ \mathbf{V}_{\text{out}} = [10^{-2}, 0, 0, 1] & \text{if } r > 0.5. \end{cases} \quad (156)$$

The benchmark is carried out using the novel 2D staggered semi-implicit DG scheme with a posteriori sub-cell finite volume limiter and the explicit one ADER-DG scheme with a posteriori sub-cell finite volume limiter (see [42]). In both cases the computational domain is composed by 100^2 cells ($N_x = N_y = 100$) with polynomial degree $P = 4$. From Table 5 it is possible to see that the simulation for the semi-implicit method is faster and involves less time steps than the explicit ADER-DG method. In addition, we compare the 2D staggered semi-implicit DG scheme with $P = 3$ against a fourth order WENO finite volume scheme ([32,34,43]). We use $N_x = N_y = 125$ for the semi-implicit DG and $N_x = N_y = 500$ for the explicit WENO method; note that with this choice the number of degrees of freedom is the same for the two simulations. Also in this last case the explicit method is less efficient than the semi-implicit scheme (see Table 5). In Fig. 38 we report some graphical results about the Low Mach number explosion test case. In the first sub-figure we give the 3D plot of the pressure obtained

using the 2D semi-implicit method; we observe that the surface is very clean and Gibbs' oscillations are not present. In the second and in the third sub-figures we show the 1D cuts along the x -axis. In particular, in 38b the numerical results of ADER-DG P4 scheme and SI DG P4 are compared against the exact solution; then in 38c the numerical results of the $P_0 P_3$ finite volume scheme and the SI DG P4 method are compared against the exact solution. We can see that ADER-DG scheme and the $P_0 P_3$ finite volume method with WENO reconstruction are slightly less viscous than the staggered semi-implicit DG scheme, because the explicit ADER schemes are characterized by a very high order of accuracy also in time.

6 Conclusions and Outlook

In this paper we have proposed a novel family of semi-implicit DG schemes on staggered meshes with a posteriori subcell finite volume limiter applied to the 1D and 2D Euler equations of gasdynamics. In particular, we have extended to high order of accuracy the FV method presented in [36] and then, in order to develop a robust shock-capturing strategy, we followed the approach used in [55] where the *a posteriori* subcell liming was extended to staggered semi-implicit schemes for the first time.

Similarly to the other *a posteriori* subcell finite volume limiters for explicit DG schemes on collocated grids developed in [7, 39, 42], this approach is based on the MOOD paradigm introduced in [23, 29, 30, 65]. Hence, an unlimited semi-implicit staggered DG method is first applied in order to produce a so-called discrete *candidate solution* at time t^{n+1} . Then, applying physical and numerical admissibility criteria, *troubled cells* characterized by a non-valid solution are detected. Then, a more robust first order semi-implicit staggered finite volume scheme is applied in the control volumes flagged as troubled cells. Successively, the linear system for the pressure is solved again involving the unlimited DG cells together with the finite volume subcells. This system can be solved very efficiently using modern matrix-free iterative Krylov subspace methods, since the pressure system resulting from a staggered discretization has the smallest possible stencil (only the cell and its direct neighbors) and the smallest possible number of unknowns (only the scalar pressure). The algorithm is concluded with the reconstruction of the DG polynomial from the piecewise constant subcell averages in the troubled cells.

Several benchmarks have been carried out in order to confirm that the new schemes behave well both for the low Mach number regime, due to the implicit treatment of the pressure term, and for several kinds of Riemann problems, since the *a posteriori* finite volume limiter stabilizes the DG scheme in the presence of shock waves and steep gradients.

In further works we will consider the extension to general equations of state, following [36]. In this case, the resulting pressure system will be mildly nonlinear and needs to be solved with the nested Newton method of Casulli and Zanolli [21, 22], for which convergence can be rigorously proven. With general equations of state we then plan to investigate cavitating compressible flows for industrial applications, see [37, 56], using the *a posteriori* subcell finite volume limiting for the semi-implicit DG proposed in [54]. In addition, we will extend the present subcell FV limiter for semi-implicit staggered DG schemes to adaptive Cartesian meshes (AMR), see [45, 89, 89, 90] and to three dimensions in space. Finally, another path to explore consists in the extension of the present staggered semi-implicit FV and DG methods to other nonlinear hyperbolic PDE systems, such as the Baer-Nunziato model for compressible multi-phase flows and the unified first order hyperbolic GPR model proposed in [9, 41, 68], which unifies a large range of different models of continuum mechanics.

Acknowledgements The authors acknowledge funding from the Istituto Nazionale di Alta Matematica (INdAM) via the GNCS group and the program *Young Researchers Funding 2018* via the research project *Semi-implicit structure preserving schemes for continuum mechanics*. MD acknowledges the financial support received from the Italian Ministry of Education, University and Research (MIUR) in the frame of the Departments of Excellence Initiative 2018–2022 attributed to DICAM of the University of Trento (Grant L. 232/2016) and in the frame of the PRIN 2017 Project *Innovative numerical methods for evolutionary partial differential equations and applications*. MD has also received funding from the University of Trento via the Strategic Initiative *Modeling and Simulation*.

Appendix A: Matrices and Tensors for the 1D Semi-implicit Schemes

Appendix A.1: Matrices and Tensors for the 1D Semi-implicit DG Method

$$\mathbf{M} = \int_0^1 \varphi(\xi) \varphi(\xi) d\xi \quad (\text{A.1})$$

$$\mathbf{K} = \int_0^1 \varphi'(\xi) \varphi(\xi) d\xi \quad (\text{A.2})$$

$$\mathbf{R}_e^{\text{DG}} = \varphi(1) \varphi\left(\frac{1}{2}\right) \varphi\left(\frac{1}{2}\right) - \int_{-\frac{1}{2}}^{\frac{1}{2}} \varphi'(\xi) \varphi\left(\xi - \frac{1}{2}\right) \varphi\left(\xi + \frac{1}{2}\right) d\xi \quad (\text{A.3})$$

$$\mathbf{L}_e^{\text{DG}} = \varphi(0) \varphi\left(\frac{1}{2}\right) \varphi\left(\frac{1}{2}\right) + \int_0^{\frac{1}{2}} \varphi'(\xi) \varphi\left(\xi + \frac{1}{2}\right) \varphi\left(\xi - \frac{1}{2}\right) d\xi \quad (\text{A.4})$$

$$\mathbf{R}_p^{\text{DG}} = \varphi\left(\frac{1}{2}\right) \varphi(0) + \int_{-\frac{1}{2}}^{\frac{1}{2}} \varphi(\xi) \varphi'\left(\xi - \frac{1}{2}\right) d\xi \quad (\text{A.5})$$

$$\mathbf{L}_p^{\text{DG}} = \varphi\left(\frac{1}{2}\right) \varphi(1) - \int_0^{\frac{1}{2}} \varphi(\xi) \varphi'\left(\xi + \frac{1}{2}\right) d\xi \quad (\text{A.6})$$

$$\mathbf{M}_L^{\text{DG}} = \int_0^{\frac{1}{2}} \varphi(\xi) \varphi\left(\xi + \frac{1}{2}\right) d\xi \quad (\text{A.7})$$

$$\mathbf{M}_R^{\text{DG}} = \int_{-\frac{1}{2}}^0 \varphi(\xi) \varphi\left(\xi - \frac{1}{2}\right) d\xi \quad (\text{A.8})$$

Appendix A.2: Matrices and Tensors for the 1D Semi-implicit Sub-cell FV Method for P = 2

$$\mathbf{R}^{\text{FV}} = \begin{pmatrix} 0 & 0 & 0 & 0 & 0 \\ 0 & 0 & 0 & 0 & 0 \\ 5 & 0 & 0 & 0 & 0 \\ -5 & 5 & 0 & 0 & 0 \\ 0 & -5 & 5 & 0 & 0 \end{pmatrix} \quad \mathbf{L}^{\text{FV}} = \begin{pmatrix} 0 & 0 & 5 & -5 & 0 \\ 0 & 0 & 0 & 5 & -5 \\ 0 & 0 & 0 & 0 & 5 \\ 0 & 0 & 0 & 0 & 0 \\ 0 & 0 & 0 & 0 & 0 \end{pmatrix} \quad (\text{A.9})$$

$$\mathbf{M}_R^{\text{FV}} = \begin{pmatrix} 0 & 0 & 0 & 0 & 0 \\ 0 & 0 & 0 & 0 & 0 \\ 0.5 & 0 & 0 & 0 & 0 \\ 0.5 & 0.5 & 0 & 0 & 0 \\ 0 & 0.5 & 0.5 & 0 & 0 \end{pmatrix} \quad \mathbf{M}_L^{\text{FV}} = \begin{pmatrix} 0 & 0 & 0.5 & 0.5 & 0 \\ 0 & 0 & 0 & 0.5 & 0.5 \\ 0 & 0 & 0 & 0 & 0.5 \\ 0 & 0 & 0 & 0 & 0 \\ 0 & 0 & 0 & 0 & 0 \end{pmatrix} \quad (\text{A.10})$$

Appendix A.3: Tensors for the Limited 1D Semi-implicit DG Method

$$\mathbf{R'}_{\mathbf{e}}^{\text{DG}} = \varphi(1)\varphi\left(\frac{1}{2}\right) - \int_{-\frac{1}{2}}^{\frac{1}{2}} \varphi'(\xi)\varphi\left(\xi - \frac{1}{2}\right) d\xi \quad (\text{A.11})$$

$$\mathbf{L'}_{\mathbf{e}}^{\text{DG}} = \varphi(0)\varphi\left(\frac{1}{2}\right) + \int_0^{\frac{1}{2}} \varphi'(\xi)\varphi\left(\xi + \frac{1}{2}\right) d\xi \quad (\text{A.12})$$

References

1. Bassi, F., Crivellini, A., Di Pietro, D.A., Rebay, S.: An artificial compressibility flux for the discontinuous Galerkin solution of the incompressible Navier–Stokes equations. *J. Comput. Phys.* **218**, 208–221 (2006)
2. Bassi, F., Crivellini, A., Di Pietro, D.A., Rebay, S.: An implicit high-order discontinuous Galerkin method for steady and unsteady incompressible flows. *Comput. Fluids* **36**, 1529–1546 (2007)
3. Bassi, F., Rebay, S.: A high-order accurate discontinuous finite element method for the numerical solution of the compressible Navier–Stokes equations. *J. Comput. Phys.* **131**, 267–279 (1997)
4. Baumann, C., Oden, J.: A discontinuous hp finite element method for convection–diffusion problems. *Comput. Methods Appl. Mech. Eng.* **175**, 311–341 (1999)
5. Baumann, C., Oden, J.: A discontinuous hp finite element method for the Euler and Navier–Stokes equation. *Int. J. Numer. Methods Fluids* **31**, 79–95 (1999)
6. Bell, J.B., Colella, P., Glaz, H.M.: A second-order projection method for the incompressible Navier–Stokes equations. *J. Comput. Phys.* **85**(2), 257–283 (1989)
7. Boscheri, W., Dumbser, M.: Arbitrary-Lagrangian–Eulerian discontinuous Galerkin schemes with a posteriori subcell finite volume limiting on moving unstructured meshes. *J. Comput. Phys.* **346**, 449–479 (2017)
8. Boscheri, W., Dumbser, M., Loubère, R.: Cell centered direct arbitrary-Lagrangian–Eulerian ADER-WENO finite volume schemes for nonlinear hyperelasticity. *Comput. Fluids* **134–135**, 111–129 (2016)
9. Busto, S., Chiocchetti, S., Dumbser, M., Gaburro, E., Peshkov, I.: High order ADER schemes for continuum mechanics. *Front. Phys.* [arXiv:1912.01964](https://arxiv.org/abs/1912.01964)
10. Busto, S., Ferrín, J.L., Toro, E.F., Vázquez-Cendón, M.E.: A projection hybrid high order finite volume/finite element method for incompressible turbulent flows. *J. Comput. Phys.* **353**, 169–192 (2018)
11. Busto, S., Toro, Eleuterio F., Elena Vázquez-Cendón, M.: Design and analysis of ADER-type schemes for model advection–diffusion–reaction equations. *J. Comput. Phys.* **327**, 553–575 (2016)
12. Casulli, V.: Semi-implicit finite difference methods for the two-dimensional shallow water equations. *J. Comput. Phys.* **86**, 56–74 (1990)
13. Casulli, V.: A high-resolution wetting and drying algorithm for free-surface hydrodynamics. *Int. J. Numer. Methods Fluids* **60**, 391–408 (2009)
14. Casulli, V.: A semi-implicit numerical method for the free-surface Navier–Stokes equations. *Int. J. Numer. Methods Fluids* **74**, 605–622 (2014)
15. Casulli, V., Cattani, E.: Stability, accuracy and efficiency of a semi-implicit method for three-dimensional shallow water flow. *Comput. Math. Appl.* **27**(4), 99–112 (1994)
16. Casulli, V., Cheng, R.T.: Semi-implicit finite difference methods for three-dimensional shallow water flow. *Int. J. Numer. Methods Fluids* **15**, 629–648 (1992)
17. Casulli, V., Dumbser, M., Toro, E.F.: Semi-implicit numerical modeling of axially symmetric flows in compliant arterial systems. *Int. J. Numer. Methods Biomed. Eng.* **28**, 257–272 (2012)
18. Casulli, V., Greenspan, D.: Pressure method for the numerical solution of transient, compressible fluid flows. *Int. J. Numer. Methods Fluids* **4**(11), 1001–1012 (1984)
19. Casulli, V., Stelling, S.: Semi-implicit subgrid modelling of three-dimensional free-surface flows. *Int. J. Numer. Methods Fluids* **67**, 441–449 (2010)
20. Casulli, V., Walters, R.A.: An unstructured grid, three-dimensional model based on the shallow water equations. *Int. J. Numer. Methods Fluids* **32**, 331–348 (2000)
21. Casulli, V., Zanolli, P.: A nested Newton-type algorithm for finite volume methods solving Richards’ equation in mixed form. *SIAM J. Sci. Comput.* **32**, 2255–2273 (2009)

22. Casulli, V., Zanolli, P.: Iterative solutions of mildly nonlinear systems. *J. Comput. Appl. Math.* **236**, 3937–3947 (2012)
23. Clain, S., Diot, S., Loubère, R.: A high-order finite volume method for systems of conservation laws: multi-dimensional optimal order detection (MOOD). *J. Comput. Phys.* **230**(10), 4028–4050 (2011)
24. Cockburn, B., Lin, S.Y., Shu, C.W.: TVB Runge-Kutta local projection discontinuous Galerkin finite element method for conservation laws III: one dimensional systems. *J. Comput. Phys.* **84**, 90–113 (1989)
25. Cockburn, B., Lin, S.-Y., Shu, C.-W.: TVB Runge Kutta local projection discontinuous Galerkin finite element method for conservation laws III: one-dimensional systems. *J. Comput. Phys.* **84**, 90 (1989)
26. Cockburn, B., Shu, C.W.: TVB Runge-Kutta local projection discontinuous Galerkin finite element method for conservation laws II: general framework. *Math. Comput.* **52**, 411–435 (1989)
27. Cockburn, B., Shu, C.W.: The Runge-Kutta local projection P1-discontinuous Galerkin finite element method for scalar conservation laws. *Math. Modell. Numer. Anal.* **25**, 337–361 (1991)
28. Cockburn, B., Shu, C.W.: The Runge-Kutta discontinuous Galerkin method for conservation laws V: multidimensional systems. *J. Comput. Phys.* **141**, 199–224 (1998)
29. Diot, S., Clain, S., Loubère, R.: Improved detection criteria for the multi-dimensional optimal order detection (MOOD) on unstructured meshes with very high-order polynomials. *Comput. Fluids* **64**(Supplement C), 43–63 (2012)
30. Diot, S., Loubère, R., Clain, S.: The multidimensional optimal order detection method in the three-dimensional case: very high-order finite volume method for hyperbolic systems. *Int. J. Numer. Methods Fluids* **73**(4), 362–392 (2013)
31. Dolejsi, V., Feistauer, M.: A semi-implicit discontinuous Galerkin method for the numerical solution of inviscid compressible flows. *J. Comput. Phys.* **198**, 727–746 (2004)
32. Dumbser, M.: Arbitrary high order PNPM schemes on unstructured meshes for the compressible Navier–Stokes equations. *Comput. Fluids* **39**(1), 60–76 (2010)
33. Dumbser, M., Balsara, D.S., Tavelli, M., Fambri, F.: A divergence-free semi-implicit finite volume scheme for ideal, viscous and resistive magnetohydrodynamics. *Int. J. Numer. Methods Fluids* **89**, 16–42 (2018)
34. Dumbser, M., Balsara, D.S., Toro, E.F., Munz, C.D.: A unified framework for the construction of one-step finite volume and discontinuous Galerkin schemes on unstructured meshes. *J. Comput. Phys.* **227**(18), 8209–8253 (2008)
35. Dumbser, M., Casulli, V.: A staggered semi-implicit spectral discontinuous Galerkin scheme for the shallow water equations. *Appl. Math. Comput.* **219**(15), 8057–8077 (2013)
36. Dumbser, M., Casulli, V.: A conservative, weakly nonlinear semi-implicit finite volume scheme for the compressible Navier–Stokes equations with general equation of state. *Appl. Math. Comput.* **272**, 479–497 (2016)
37. Dumbser, M., Iben, U., Ioriatti, M.: An efficient semi-implicit finite volume method for axially symmetric compressible flows in compliant tubes. *Appl. Numer. Math.* **89**, 24–44 (2015)
38. Dumbser, M., Käser, M.: Arbitrary high order non-oscillatory finite volume schemes on unstructured meshes for linear hyperbolic systems. *J. Comput. Phys.* **221**(2), 693–723 (2007)
39. Dumbser, M., Loubère, R.: A simple robust and accurate a posteriori sub-cell finite volume limiter for the discontinuous Galerkin method on unstructured meshes. *J. Comput. Phys.* **319**(Supplement C), 163–199 (2016)
40. Dumbser, M., Munz, C.D.: Building blocks for arbitrary high order discontinuous Galerkin schemes. *J. Sci. Comput.* **27**, 215–230 (2006)
41. Dumbser, M., Peshkov, I., Romenski, E., Zanotti, O.: High order ADER schemes for a unified first order hyperbolic formulation of continuum mechanics: viscous heat-conducting fluids and elastic solids. *J. Comput. Phys.* **314**, 824–862 (2016)
42. Dumbser, M., Zanotti, O., Loubère, R., Diot, S.: A posteriori subcell limiting of the discontinuous Galerkin finite element method for hyperbolic conservation laws. *J. Comput. Phys.* **278**, 47–75 (2014)
43. Dumbser, Michael, Hidalgo, Arturo, Zanotti, Olindo: High order space-time adaptive ADER-WENO finite volume schemes for non-conservative hyperbolic systems. *Comput. Methods Appl. Mech. Eng.* **268**, 359–387 (2014)
44. Fambri, F., Dumbser, M.: Spectral semi-implicit and space-time discontinuous Galerkin methods for the incompressible Navier–Stokes equations on staggered Cartesian grids. *Appl. Numer. Math.* **110**, 41–74 (2016)
45. Fambri, F., Dumbser, M.: Semi-implicit discontinuous Galerkin methods for the incompressible Navier–Stokes equations on adaptive staggered Cartesian grids. *Comput. Methods Appl. Mech. Eng.* **324**, 170–203 (2017)
46. Fambri, F., Dumbser, M., Casulli, V.: An efficient semi-implicit method for three-dimensional non-hydrostatic flows in compliant arterial vessels. *Int. J. Numer. Methods Biomed. Eng.* **30**, 1170–1198 (2014)

47. Gassner, G., Lörcher, F., Munz, C.-D.: A discontinuous Galerkin scheme based on a space–time expansion II. Viscous flow equations in multi dimensions. *J. Sci. Comput.* **34**(3), 260–286 (2008)
48. Gassner, G., Lörcher, F., Munz, C.D.: A contribution to the construction of diffusion fluxes for finite volume and discontinuous Galerkin schemes. *J. Comput. Phys.* **224**, 1049–1063 (2007)
49. Godunov, S.K.: Finite difference methods for the computation of discontinuous solutions of the equations of fluid dynamics. *Math. USSR Sb.* **47**, 271–306 (1959)
50. Gottlieb, S., Shu, C.W.: Total variation diminishing Runge–Kutta schemes. *Math. Comput.* **67**(221), 73–85 (1998)
51. Hartmann, R., Houston, P.: Symmetric interior penalty DG methods for the compressible Navier–Stokes equations I: method formulation. *Int. J. Numer. Anal. Model.* **3**, 1–20 (2006)
52. Hartmann, R., Houston, P.: An optimal order interior penalty discontinuous Galerkin discretization of the compressible Navier–Stokes equations. *J. Comput. Phys.* **227**, 9670–9685 (2008)
53. Hu, C., Shu, C.W.: Weighted essentially non-oscillatory schemes on triangular meshes. *J. Comput. Phys.* **150**, 97–127 (1999)
54. Ioriatti, M., Dumbser, M.: Semi-implicit staggered discontinuous Galerkin schemes for axially symmetric viscous compressible flows in elastic tubes. *Comput. Fluids* **167**, 166–179 (2018)
55. Ioriatti, M., Dumbser, M.: A posteriori sub-cell finite volume limiting of staggered semi-implicit discontinuous Galerkin schemes for the shallow water equations. *Appl. Numer. Math.* **135**, 443–480 (2019)
56. Ioriatti, M., Dumbser, M., Iben, U.: A comparison of explicit and semi-implicit finite volume schemes for viscous compressible flows in elastic pipes in fast transient regime. *Zeitschrift fuer Angewandte Mathematik und Mechanik* **97**, 1358–1380 (2017)
57. Jiang, G.S., Shu, C.W.: Efficient implementation of weighted ENO schemes. *J. Comput. Phys.* **126**(1), 202–228 (1996)
58. Käser, M., Iske, A.: ADER schemes on adaptive triangular meshes for scalar conservation laws. *J. Comput. Phys.* **205**(2), 486–508 (2005)
59. Klaij, C.M., van der Vegt, J.J.W., van der Ven, H.: Space-time discontinuous Galerkin method for the compressible Navier–Stokes equations. *J. Comput. Phys.* **217**(2), 589–611 (2006)
60. Kramer, S.C., Stelling, G.S.: A conservative unstructured scheme for rapidly varied flows. *Int. J. Numer. Methods Fluids* **58**, 183–212 (2008)
61. Kurganov, A., Tadmor, E.: Solution of two-dimensional Riemann problems for gas dynamics without Riemann problem solvers. *Numer. Methods Partial Differ. Equ.* **18**(5), 584–608 (2002)
62. Lax, Peter, Wendroff, Burton: Systems of conservation laws. *Commun. Pure Appl. Math.* **13**(2), 217–237 (1960)
63. Liu, Y.J., Shu, C.W., Tadmor, E., Zhang, M.: Central discontinuous Galerkin methods on overlapping cells with a non-oscillatory hierarchical reconstruction. *SIAM J. Numer. Anal.* **45**, 2442–2467 (2007)
64. Liu, Y.J., Shu, C.W., Tadmor, E., Zhang, M.: L₂-stability analysis of the central discontinuous Galerkin method and a comparison between the central and regular discontinuous Galerkin methods. *Math. Model. Numer. Anal.* **42**, 593–607 (2008)
65. Loubère, R., Dumbser, M., Diot, S.: A new family of high order unstructured MOOD and ADER finite volume schemes for multidimensional systems of hyperbolic conservation laws. *Commun. Comput. Phys.* **16**(3), 718–763 (2014)
66. Neumann, J., Richtmyer, R.D.: A method for the numerical calculation of hydrodynamic shocks. *J. Appl. Phys.* **21**, 232–237 (1950)
67. Park, J.H., Munz, C.D.: Multiple pressure variables methods for fluid flow at all Mach numbers. *Int. J. Numer. Methods Fluids* **49**, 905–931 (2005)
68. Peshkov, I., Romenski, E.: A hyperbolic model for viscous Newtonian flows. *Contin. Mech. Thermodyn.* **28**, 85–104 (2016)
69. Qiu, J., Dumbser, M., Shu, C.W.: The discontinuous Galerkin method with Lax–Wendroff type time discretizations. *Comput. Methods Appl. Mech. Eng.* **194**, 4528–4543 (2005)
70. Reed, W.H., Hill, T.R.: Triangular mesh methods for the neutron transport equation. Technical report LA-UR-73-479, Los Alamos Scientific Laboratory (1973)
71. Roe, P.L.: Approximate Riemann solvers, parameter vectors, and difference schemes. *J. Comput. Phys.* **43**, 357–372 (1981)
72. Schulz-Rinne, C.: Classification of the Riemann problem for two-dimensional gas dynamics. *SIAM J. Math. Anal.* **24**(1), 76–88 (1993)
73. Sod, Gary A.: A survey of several finite difference methods for systems of nonlinear hyperbolic conservation laws. *J. Comput. Phys.* **27**(1), 1–31 (1978)
74. Stelling, G.S., Duymeyer, S.P.A.: A staggered conservative scheme for every Froude number in rapidly varied shallow water flows. *Int. J. Numer. Methods Fluids* **43**, 1329–1354 (2003)

75. Tavelli, M., Dumbser, M.: A high order semi-implicit discontinuous Galerkin method for the two dimensional shallow water equations on staggered unstructured meshes. *Appl. Math. Comput.* **234**, 623–644 (2014)
76. Tavelli, M., Dumbser, M.: A staggered semi-implicit discontinuous Galerkin method for the two dimensional incompressible Navier–Stokes equations. *Appl. Math. Comput.* **248**, 70–92 (2014)
77. Tavelli, M., Dumbser, M.: A staggered space–time discontinuous Galerkin method for the incompressible Navier–Stokes equations on two-dimensional triangular meshes. *Comput. Fluids* **119**, 235–249 (2015)
78. Tavelli, M., Dumbser, M.: A staggered space–time discontinuous Galerkin method for the three-dimensional incompressible Navier–Stokes equations on unstructured tetrahedral meshes. *J. Comput. Phys.* **319**, 294–323 (2016)
79. Tavelli, M., Dumbser, M.: A pressure-based semi-implicit space–time discontinuous Galerkin method on staggered unstructured meshes for the solution of the compressible Navier–Stokes equations at all Mach numbers. *J. Comput. Phys.* **341**, 341–376 (2017)
80. Tavelli, M., Dumbser, M.: Arbitrary high order accurate space–time discontinuous Galerkin finite element schemes on staggered unstructured meshes for linear elasticity. *J. Comput. Phys.* **366**, 386–414 (2018)
81. Tavelli, M., Dumbser, M., Casulli, V.: High resolution methods for scalar transport problems in compliant systems of arteries. *Appl. Numer. Math.* **74**, 62–82 (2013)
82. Toro, E.F.: Riemann Solvers and Numerical Methods for Fluid Dynamics. Springer, Berlin (2009)
83. Toro, E.F., Vázquez-Cendón, M.E.: Flux splitting schemes for the Euler equations. *Comput. Fluids* **70**, 1–12 (2012)
84. Tumolo, G., Bonaventura, L.: A semi-implicit, semi-Lagrangian discontinuous Galerkin framework for adaptive numerical weather prediction. *Q. J. R. Meteorol. Soc.* **141**(692), 2582–2601 (2015)
85. Tumolo, G., Bonaventura, L., Restelli, M.: A semi-implicit, semi-Lagrangian, p-adaptive discontinuous Galerkin method for the shallow water equations. *J. Comput. Phys.* **232**, 46–67 (2013)
86. van der Vegt, J.J.W., van der Ven, H.: Space–time discontinuous Galerkin finite element method with dynamic grid motion for inviscid compressible flows: I. General formulation. *J. Comput. Phys.* **182**(2), 546–585 (2002)
87. van der Ven, H., van der Vegt, J.J.W.: Space–time discontinuous Galerkin finite element method with dynamic grid motion for inviscid compressible flows: II. Efficient flux quadrature. *Comput. Methods Appl. Mech. Eng.* **191**(41), 4747–4780 (2002)
88. van Leer, B.: Toward the ultimate conservative difference scheme. V. A second-order sequel to Godunov’s method. *J. Comput. Phys.* **32**, 101–136 (1979)
89. Zanotti, O., Dumbser, M., Fambri, F.: Solving the relativistic magnetohydrodynamics equations with ADER discontinuous Galerkin methods, a posteriori subcell limiting and adaptive mesh refinement. *Mon. Not. R. Astron. Soc.* **452**, 3010–3029 (2015)
90. Zanotti, O., Fambri, F., Dumbser, M., Hidalgo, A.: Space–time adaptive ADER discontinuous Galerkin finite element schemes with a posteriori sub-cell finite volume limiting. *Comput. Fluids* **118**, 204–224 (2015)

Publisher's Note Springer Nature remains neutral with regard to jurisdictional claims in published maps and institutional affiliations.

Affiliations

Matteo Ioriatti¹ · Michael Dumbser¹ · Raphaël Loubère²

Michael Dumbser
michael.dumbser@unitn.it

Raphaël Loubère
raphael.loubere@math.u-bordeaux.fr

¹ Department of Civil, Environmental and Mechanical Engineering, University of Trento, via Mesiano 77, 38123 Trento, Italy

² Institut de Mathématiques de Bordeaux (IMB), 33405 Talence, France